Diffuse Reflection and Transmission of Light by a Medium with an Arbitrary Scattering Indicatrix

D. N. Rachkovskiĭ

Crimean Astrophysical Observatory, National Academy of Sciences of Ukraine, p/o Nauchnyĭ, Crimea, 334413 Ukraine

Received June 10, 1999

Abstract—The diffuse reflection and transmission of light by a plane-parallel medium is considered, taking into account only the azimuth-independent part of the scattering indicatrix. The scattering indicatrix is expressed in terms of an expansion in an arbitrary number of Legendre polynomials. Two approaches to the problem are analyzed using Sobolev's theory. Two systems of linear algebraic equations for the coefficients of the auxiliary polynomials $q_i(\mu)$ and $s_i(\mu)$ are derived and compared. It is shown that one of these approaches is less preferable, since it is not valid for conservative scattering. © *2000 MAIK "Nauka/Interperiodica".*

This concludes a series of papers on light scattering in a medium with an arbitrary scattering indicatrix. We use Sobolev's [1] theory for the scattering of light in planetary atmospheres as a basis for these studies. Sobolev reduced the problem at hand to the solution of a system of linear integral equations for the auxiliary polynomials $q_i(\mu)$ and $s_i(\mu)$ and showed that these integral equations can be easily transformed to a system of linear algebraic equations for the coefficients of $q_i(\mu)$ and $s_i(\mu)$.

As an example of an application of this theory, Sobolev considered the scattering of light in a semi-infinite or finite medium with a binomial scattering indicatrix [2, 3]. The case of a trinomial indicatrix ($N = 2$) has been considered by Kolesov and Sobolev [4] and Kolesov and Smoktiĭ [5]. Kolesov and Smoktiĭ [6] also solved the problem of the scattering of light in a semi-infinite medium with a quadratic indicatrix ($N = 3$).

In the case of nonconservative scattering, the reduction of the linear integral equations for the polynomials $q_i(\mu)$ and $s_i(\mu)$ to a complete system of linear algebraic equations for the coefficients of $q_i(\mu)$ and $s_i(\mu)$ has a rather simple general form for any number N; nevertheless, it had not been solved prior to our studies [7, 8]. The system of linear algebraic equations for the case of conservative scattering turns out to be incomplete: one equation is missing.

Sobolev [1] avoided this difficulty by solving the system of equations using the Horner method with $\omega_0 \neq 1$. He obtained a solution by going to the conservative-scattering limit in the determinants. The same procedure was used by Kolesov and Smoktiĭ [5, 6]. However, when solving the system of equations using the Horner method for $N > 3$, major difficulties arise due to the necessity of taking into account elements of the determinants of different orders in the small parameter $1 - \omega_0$. We

derived the missing equation first based on semitheoretical reasoning [9] and then rigorously [10] using the constraints of Mullikin [11].

All these analyses used linear integral equations for the polynomials $q_i(\mu)$ and $s_i(\mu)$ as input equations. However, Sobolev outlined another approach to the solution in [1]. In addition to the integral equations, Sobolev derived linear algebraic equations for $q_i(\mu)$ and $s_i(\mu)$. The form of these equations differs from those obtained from the integral equations.

In the current paper, we find a solution for the scattering of light in a medium with an arbitrary indicatrix. From the form of the algebraic equations proposed by Sobolev for $q_i(\mu)$ and $s_i(\mu)$, we have derived for any N another type of equation for the polynomial coefficients. We have found expressions relating the matrices of these two forms of the linear algebraic equations. In the case of conservative scattering, the new form of the equations is incomplete; i.e., there is one equation too few to fully determine the unknowns. The question of the existence of the missing equation remains open.

For reference, we list the basic relationships obtained in [7–10].

The scattering indicatrix is

$$p(\mu, \mu') = \mathbf{P}(\mu)^T \cdot \boldsymbol{\omega} \cdot \mathbf{P}(\mu'). \tag{1}$$

The components of the vector $\mathbf{P}(\mu)$ are the Legendre polynomials $P_n(\mu)$

$$\mathbf{P}(\mu)^T = \{P_0(\mu), P_1(\mu), \ldots, P_N(\mu)\}, \tag{2}$$

where $\boldsymbol{\omega}$ is a diagonal matrix with elements

$$\omega_{ij} = \omega_i \delta_{ij} \quad i, j = 0, 1, 2, \ldots, N. \tag{3}$$

The reflectivity and transmissivity of a medium of finite optical depth, $\rho(\mu, \mu_0)$ and $\sigma(\mu, \mu_0)$, are represented in terms of the vector functions $\boldsymbol{\varphi}(\mu)$ and $\boldsymbol{\psi}(\mu)$:

$$\rho(\mu, \mu_0) = \frac{1}{4} \frac{\boldsymbol{\varphi}(\mu)^T \mathbf{k}\boldsymbol{\omega}\boldsymbol{\varphi}(\mu_0) - \boldsymbol{\psi}(\mu)^T \mathbf{k}\boldsymbol{\omega}\boldsymbol{\psi}(\mu_0)}{\mu + \mu_0}, \quad (4)$$

$$\sigma(\mu, \mu_0) = \frac{1}{4} \frac{\boldsymbol{\varphi}(\mu_0)^T \boldsymbol{\omega}\boldsymbol{\psi}(\mu) - \boldsymbol{\varphi}(\mu)^T \boldsymbol{\omega}\boldsymbol{\psi}(\mu_0)}{\mu - \mu_0}. \quad (5)$$

The components of $\boldsymbol{\varphi}(\mu)$ and $\boldsymbol{\psi}(\mu)$ are the auxiliary functions $\varphi_i(\mu)$ and $\psi_i(\mu)$:

$$\boldsymbol{\varphi}(\mu)^T = \{\varphi_0(\mu), \varphi_1(\mu), \ldots, \varphi_N(\mu)\}, \quad (6)$$

$$\boldsymbol{\psi}(\mu)^T = \{\psi_0(\mu), \psi_1(\mu), \ldots, \psi_N(\mu)\}, \quad (7)$$

and $\mathbf{k}$ is a diagonal matrix with coefficients

$$k_{ij} = (-1)^j \delta_{ij} \quad i, j = 0, 1, 2, \ldots, N. \quad (8)$$

In turn, the vectors $\boldsymbol{\varphi}(\mu)$ and $\boldsymbol{\psi}(\mu)$ are defined in terms of the Chandrasekhar functions $X(\mu)$ and $Y(\mu)$:

$$\boldsymbol{\varphi}(\mu) = \frac{1}{2} \sum_{i=0}^{N} \mu^i [(X(\mu) + (-1)^i Y(\mu))\mathbf{q}_i^+$$

$$+ (X(\mu) - (-1)^i Y(\mu))\mathbf{q}_i^-],$$

$$\boldsymbol{\psi}(\mu) = \frac{1}{2} \sum_{i=0}^{N} \mu^i \mathbf{k}[(X(\mu) + (-1)^i Y(\mu))\mathbf{q}_i^+ \quad (9)$$

$$- (X(\mu) - (-1)^i Y(\mu))\mathbf{q}_i^-].$$

In [10], $\mathbf{q}_i^+$ and $\mathbf{q}_i^-$ are found from the system of linear algebraic equations

$$\mathbf{D}^{\pm} \cdot \mathbf{Q}^{\pm} = \mathbf{B}^{\pm}, \quad (10)$$

where the components of the vector $\mathbf{Q}^{\pm}$ are the vectors $\mathbf{q}_i^{\pm}$:

$$\mathbf{Q}^{\pm T} = \{\mathbf{q}_1^{\pm}, \mathbf{q}_2^{\pm}, \ldots, \mathbf{q}_N^{\pm}\}. \quad (11)$$

The vectors $\mathbf{q}_0^{\pm}$ and $\mathbf{q}_i^{\pm}$ are defined as

$$\mathbf{q}_0^{\pm} = \{P_0(0), P_1(0), \ldots, P_N(0)\},$$
$$\mathbf{q}_i^{\pm} = \{q_{i0}^{\pm}, q_{i1}^{\pm}, \ldots, q_{iN}^{\pm}\}. \quad (12)$$

In nonconservative scattering, the components of the matrix $\mathbf{D}$ are written as

$$D_{ij}^{\pm} = \begin{cases} \sum_{m=0}^{i-1} (A_{m, m+j-i}^X \pm (-1)^j A_{m, m+j-i}^Y) & i < j \\[2mm] -1 + \sum_{m=0}^{i-1} (A_{m, m}^X \pm (-1)^j A_{m, m}^Y) & i = j \\[2mm] -\sum_{m=i}^{N} (A_{m, m+j-i}^X \pm (-1)^j A_{m, m+j-i}^Y) & i > j \end{cases} \quad (13)$$

$$i, j = 1, 2, \ldots, N.$$

For conservative scattering, the components of $D_{ij}^{\pm}$ are determined from (13) only for indices

$$\begin{aligned} i &= 1, 2, \ldots, N-2 \\ j &= 1, 2, \ldots, N. \end{aligned} \quad (14)$$

The $(N-1)$th equation for the vectors $\mathbf{q}^+$ is written as

$$\sum_{j=1}^{N} (\alpha_j + (-1)^j \beta_j) \mathbf{q}_j^+ = 2\delta_0 - (\alpha_0 + \beta_0) \mathbf{r}_0. \quad (15)$$

For the vectors $\mathbf{q}^-$, it has the form

$$\sum_{j=1}^{N} C_j \cdot \mathbf{q}_j^- = -C_0 \mathbf{r}_0 + 2\left(1 - \frac{1}{3}\omega_1\right)\tau_0 \delta_0 + \frac{4}{3}\delta_1. \quad (16)$$

The vectors δ_0 and δ_i have only one nonzero component:

$$\delta_0^T = \{1, 0, 0, \ldots, 0\},$$
$$\delta_1^T = \{0, 1, 0, \ldots, 0\}.$$

For conservative scattering, the Nth equation has two forms, depending on whether N is even or odd:

$$\left[-1 + \sum_{m=0}^{N-2} (A_{m, m}^X - A_{m, m}^Y)\right] \cdot \mathbf{q}_{N-1}^{\pm}$$

$$+ \sum_{m=0}^{N-2} (A_{m, m+1}^X + A_{m, m+1}^Y) \cdot \mathbf{q}_N^{\pm} = 0, \quad (17)$$

$$\mathbf{q}_N^{\mp} = 0.$$

Here, the upper sign of $\mathbf{q}_i$ corresponds to even N, and the lower sign is chosen if N is odd.

We have in the case of conservative scattering in a semi-infinite medium

$$A_{ij}^Y = 0,$$

$$\left[-1 + \sum_{m=0}^{N-2} (A_{m, m}^X + A_{m, m}^Y)\right] = 0,$$

so that

$$\mathbf{q}_N^+ = \mathbf{q}_N^- = 0,$$

the Nth equation becomes an identity, and the $(N–1)$th equation will be (15) with $\beta_j = 0$ and $\mathbf{q}_j^+ = \mathbf{q}_j$.

In equations (13), (15), (16), and (17), it remains to determine the quantities

$$C_i = (\alpha_i - (-1)^i \beta_i)\left(1 - \frac{1}{3}\omega_1\right)\tau_0 \tag{18}$$

$$+ 2(\alpha_{i+1} - (-1)^i \beta_{i+1}),$$

$$\alpha_i = \int_0^1 X(\mu)\mu^i d\mu, \quad \beta_i = \int_0^1 Y(\mu)\mu^i d\mu, \tag{19}$$

and

$$A_{ij}^X = \frac{1}{2}\int_0^1 (\mathbf{r}_i^T \boldsymbol{\omega} \mathbf{P}(\mu))\mu^j X(\mu) d\mu \tag{20}$$

and analogously for A_{ij}^Y.

The components r_{ij} of the vectors $\mathbf{r}_i$ are given by the recursion relationships

$$r_{ij} = \frac{1}{j}(-(j-1)r_{i,j-2} + (2j-1-\omega_{j-1})r_{i-1,j-1}),$$

$$r_{0j} = P_j(0) \quad r_{ij} = 0 \quad \text{for} \quad i > j, \tag{21}$$

$$i, j = 0, 1, 2, \ldots, N.$$

It remains to find the right-hand side of equation (10). We have

$$\mathbf{B}^{\pm T} = \{\mathbf{b}_1^{\pm}, \mathbf{b}_2^{\pm}, \ldots, \mathbf{b}_N^{\pm}\}, \tag{22}$$

where

$$\mathbf{b}_i^{\pm} = \sum_{m=i}^{N} (A_{m,m-i}^X \pm A_{m,m-i}^Y)\mathbf{r}_0 - \mathbf{r}_i. \tag{23}$$

The above formulas represent the basic results of [7–10]. We present them here to facilitate our subsequent analysis, since many quantities contained in these formulas appear below. As noted above, our main aim is to study the different form of the linear algebraic equations for $q_i(\mu)$ and $s_i(\mu)$ proposed by Sobolev [1], rather than that underlying (10).

Let us write this in Sobolev's notation. To increase the transparency of the calculations, we consider scattering in a semi-infinite medium. It will be easy to extend the final results to the case of scattering in a medium of finite optical depth.

Thus, according to [1], we have in Sobolev's notation

$$q_i(\mu) = R_{i0}(\mu) + \sum_{k=1}^{N}\left[q_k(\mu) + \frac{k-1}{k}q_{k-2}(\mu)\right] \tag{24}$$

$$\times \int_0^1 g_{ik}(\eta)H(\eta)d\eta.$$

We must find relationships between the coefficients of the polynomials $q_i(\mu)$. Writing

$$q_i(\mu) = \sum_{j=0}^{N} q_{ij}\mu^j, \tag{25}$$

substituting (25) into (24), and equating the coefficients of terms with equal powers of μ, we find

$$q_{ij} = r_{ij} + \sum_{k=1}^{N}\left[q_{kj} + \frac{k-1}{k}q_{k-2,j}\right]\int_0^1 g_{ik}(\eta)H(\eta)d\eta. \tag{26}$$

The second subscript in the coefficients q_{ij} and in (26) refers to the power of μ. In our presentation, it comes first; therefore, we permutate the subscripts i and j in (26) and redefine

$$i, j \longrightarrow j, i.$$

As a result, we obtain

$$q_{ij} = r_{ij} + \sum_{k=1}^{N}\left[q_{ik} + \frac{k-1}{k}q_{i,k-2}\right]\int_0^1 g_{jk}(\eta)H(\eta)d\eta. \tag{27}$$

Introducing the notation

$$g_{jk} = \int_0^1 g_{jk}(\eta)H(\eta)d\eta, \tag{28}$$

we can write (27) in matrix form:

$$G_{mn}q_{in} = -r_{im}, \tag{29}$$

$$i, m, n = 0, 1, 2, \ldots, N.$$

In (29), the matrix elements G_{mn} are defined as

$$G_{ij} = \frac{1}{2}g_{j2} - \delta_{ij} \quad j = 0,$$

$$G_{ij} = g_{ij} + \frac{j+1}{j+2}g_{i,j+2} - \delta_{ij} \quad j = 1, 2, \ldots, N-2, \tag{30}$$

$$G_{ij} = g_{ij} - \delta_{ij} \quad j = N-1, N.$$

Sobolev gives the expression

$$g_{jk}(\eta) = \Psi(\eta)R_{jk}(\eta) - \Psi_k(\eta)R_{j0}(\eta) \tag{31}$$

for the quantity $g_{jk}(\eta)$ in (27). Interchanging the subscripts i and k in the polynomial $R_{ik}(\eta)$ and designating r_{kij} to be the coefficients for the powers η^j, we obtain

$$R_{ki}(\eta) = \sum_{j=0}^{N-k} r_{kij}\eta^j \qquad (32)$$

and

$$r_{0ij} = r_{ij}.$$

We can derive the recursion relationship

$$r_{kij} = \frac{1}{k+j}[-(k+j-1)r_{k,i,j-2}$$

$$+ (2k+2j-1-\omega_{k-1+j})r_{k,i-1,j-1}]$$

$$k, i = 0, 1, \ldots, N \quad j = 0, 1, \ldots, N-k, \qquad (33)$$

$$\begin{array}{l} r_{kij} = 0 \\ r_{k00} = 1 \end{array} \quad i, j < 0$$

for r_{kij}. Let us write an expansion of the Legendre polynomial $P_i(\eta)$ in powers of η:

$$P_i(\eta) = \sum_{j=0}^{i} p_{ij}\eta^j. \qquad (34)$$

We have for the functions $\Psi_k(\eta)$ in (31)

$$\Psi_k(\eta) = \frac{1}{2}\sum_{i=k}^{N} \omega_i R_{ki}(\eta) P_i(\eta), \qquad (35)$$

and we can obtain an expression for g_{ik} that is convenient for computer calculations:

$$g_{ik} = \frac{1}{2}\left\{ \sum_{m=0}^{i-k} r_{k,m,i-k}\sum_{j=0}^{N}\omega_j\sum_{l=0}^{j}p_{l,j}\sum_{n=0}^{j}r_{0nj}\alpha_{l+m+n} \right.$$

$$\left. - \sum_{m=0}^{i} r_{0,m,i}\sum_{j=k}^{N}\omega_j\sum_{l=0}^{j}p_{lj}\sum_{n=0}^{j-k}r_{k,n,j-k}\alpha_{l+m+n} \right\} \qquad (36)$$

$$i, k = 0, 1, \ldots, N.$$

Here, α_k are moments of the functions $H(\mu)$:

$$\alpha_k = \int_0^1 H(\mu)\mu^k d\mu. \qquad (37)$$

Let us now compare the two forms of the linear algebraic equations (10) and (29), determining the components of the polynomials $q_i(\mu)$:

$$D_{ik}q_{km} = b_{im} \quad i, k = 1, 2, \ldots, N$$

$$m = 0, 1, 2, \ldots, N, \qquad (38)$$

$$G_{jm}q_{km} = -r_{kj} \quad j, k, m = 0, 1, \ldots, N. \qquad (39)$$

For nonconservative scattering, the rank of the matrix G is greater than that of D by unity. Let us find a relation between the elements of the matrices D and G. In accordance with (23), we write b_{im} in (38)

$$b_{im} = c_i r_{0m} - r_{im}. \qquad (40)$$

Multiplying (38) by G_{jm} and summing over the subscript m, we obtain

$$-D_{ik}r_{kj} = -c_i r_{0j} + G_{jm}r_{im}$$

$$i, k = 1, 2, \ldots, N \qquad (41)$$

$$j, m = 0, 1, \ldots, N.$$

Taking into account the fact that the coefficients r_{kj} form a triangular matrix, we can obtain the following recursion relations, expressing the elements D_{ik} in terms of G_{jm}:

$$D_{is} = \left(c_i r_{0s} - \sum_{m=i}^{N} G_{sm}r_{im} \right)/r_{ss} \quad s = 1, 2,$$

$$D_{ik} = \left(-\sum_{l=s}^{k-2} D_{il}r_{lk} + c_i r_{0k} - \sum_{m=i}^{N} G_{km}r_{im} \right)/r_{kk}, \qquad (42)$$

$$i = 1, 2, \ldots, N \quad s = 1, 2 \quad k = 2+s, 3+s, \ldots, N.$$

Inversely, we can find an expression for the elements G_{jm} in terms of D_{ik}:

$$G_{js} = \left(c_s r_{0j} - \sum_{k=i}^{j} D_{sk}r_{kj} \right)/r_{ss},$$

$$G_{jm} = \left(c_m r_{0j} - \sum_{l=m+2}^{N} G_{jl}r_{ml} - \sum_{k=1}^{j} D_{mk}r_{kj} \right)/r_{mm}, \qquad (43)$$

$$G_{j0} = -r_{0j} - \sum_{k=2}^{N} G_{jm}r_{0m}$$

$$j = 0, 1, \ldots, N \quad s = N-1, N \quad m = s-2, s-3, \ldots 1.$$

Formulas similar to (42) and (43) can also be derived for the case of conservative scattering. However, they are of little use, since G remains degenerate. In particular, in accordance with (30), we find

$$G_{0m} = -2G_{2m} \quad m = 0, 1, \ldots, N.$$

G can be obtained from D, but upon the inverse transformation $G \longrightarrow D$, the elements $D_{i,N-1}$, where $i = 1, 2, \ldots, N-1$ are not determined.

We now turn to the theory of scattering of light in a medium of finite optical depth. Sobolev [1] showed that $q_i(\mu)$ and $s_i(\mu)$ satisfy the equations

$$q_i(\mu) = R_i(\mu) + \sum_{k=1}^{N}\left[q_k(\mu) + \frac{k-1}{k}q_{k-2}(\mu) \right]$$

$$\times \int_0^1 g_{ik}(\eta)X(\eta)d\eta$$

$$+ \sum_{k=1}^{N}\left[s_k(\mu)+\frac{k-1}{k}s_{k-2}(\mu)\right]\int_0^1 g_{ik}(-\eta)Y(\eta)d\eta, \quad (44)$$

$$s_i(\mu) = \sum_{k=1}^{N}\left[q_k(\mu)+\frac{k-1}{k}q_{k-2}(\mu)\right]\int_0^1 g_{ik}(\eta)Y(\eta)d\eta$$

$$+ \sum_{k=1}^{N}\left[s_k(\mu)+\frac{k-1}{k}s_{k-2}(\mu)\right]\int_0^1 g_{ik}(-\eta)X(\eta)d\eta.$$

Expanding $q_i(\mu)$ and $s_i(\mu)$ in powers of μ, as we have done earlier in (25), permuting the subscripts i and j, and substituting $i, j \longrightarrow j, i$, we obtain

$$q_{ij} = r_{ij} + \sum_{k=1}^{N}\left[q_{ik}+\frac{k-1}{k}q_{i,k-2}\right]\int_0^1 g_{jk}(\eta)X(\eta)d\eta$$

$$+ \sum_{k=1}^{N}\left[s_{ik}+\frac{k-1}{k}s_{i,k-2}\right](-1)^{j+k}\int_0^1 g_{jk}(\eta)Y(\eta)d\eta,$$

$$s_{ij} = \sum_{k=1}^{N}\left[q_{ik}+\frac{k-1}{k}q_{i,k-2}\right]\int_0^1 g_{jk}(\eta)Y(\eta)d\eta$$

$$+ \sum_{k=1}^{N}\left[s_{ik}+\frac{k-1}{k}s_{i,k-2}\right]\int_0^1 g_{jk}(\eta)X(\eta)d\eta. \quad (45)$$

When deriving (45), we used the equality

$$g_{jk}(-\eta) = (-1)^{j+k}g_{jk}(\eta).$$

We introduce the notation

$$q_{ij}^{\pm} = q_{ij} \pm (-1)^j s_{ij}. \quad (46)$$

With (12) and the definitions

$$q_i^T = \{q_{i0}, q_{i1}, ..., q_{iN}\},$$
$$s_i^T = \{s_{i0}, s_{i1}, ..., s_{iN}\}, \quad (47)$$

we can see that $q_{ij}^{\pm}$ are the components of the vector

$$\mathbf{q}_i^{\pm} = \mathbf{q}_i \pm \mathbf{k}\mathbf{s}_i. \quad (48)$$

Multiplying the second equation of (45) by $(-1)^j$, then adding or subtracting these equations and using relation (46), we obtain

$$q_{ij}^{\pm} = r_{ij} + \sum_{k=1}^{N}\left[q_{ik}^{\pm}+\frac{k-1}{k}q_{i,k-2}^{\pm}\right]$$

$$\times \int_0^1 g_{jk}(\eta)[X(\eta)\pm(-1)^j Y(\eta)]d\eta. \quad (49)$$

Designating

$$g_{jk}^{\pm} = \int_0^1 g_{jk}(\eta)[X(\eta)\pm(-1)^j Y(\eta)]d\eta, \quad (50)$$

we finally obtain

$$q_{ij}^{\pm} = r_{ij} + \sum_{k=1}^{N}\left[q_{ik}^{\pm}+\frac{k-1}{k}q_{i,k-2}^{\pm}\right]g_{jk}^{\pm}. \quad (51)$$

It is obvious that the equations defining $q_{ij}^{\pm}$ maintain a form similar to (29):

$$G_{mn}^{\pm}q_{in}^{\pm} = -r_{im} \quad i, m, n = 0, 1, 2, ..., N. \quad (52)$$

The elements of the matrices $G_{mn}^{\pm}$ are determined by a relation similar to (30):

$$G_{ij}^{\pm} = \frac{1}{2}g_{j,2}^{\pm}-\delta_{ij} \quad j = 0,$$

$$G_{ij}^{\pm} = g_{ij}^{\pm}+\frac{j+1}{j+2}g_{i,j+2}^{\pm}-\delta_{ij} \quad j = 1, 2, ..., N-2, \quad (53)$$

$$G_{ij}^{\pm} = g_{ij}^{\pm}-\delta_{ij} \quad j = N-1, N.$$

We can obtain a formula similar to (36) for $g_{ij}^{\pm}$, with one distinction: instead of α_k, there appear the quantities

$$\alpha_{ik}^{\pm} = \int_0^1 [X(\mu)\pm(-1)^i Y(\mu)]\mu^k d\mu. \quad (54)$$

For completeness, we list the resulting system of formulas:

$$g_{ik}^{\pm} = \frac{1}{2}\left\{\sum_{m=0}^{i-k}r_{k,m,i-k}\sum_{j=0}^{N}\omega_j\sum_{l=0}^{j}p_{lj}\sum_{n=0}^{j}r_{nj}\alpha_{i,l+m+n}^{\pm}\right.$$

$$\left.- \sum_{m=0}^{i}r_{m,i}\sum_{j=k}^{N}\omega_j\sum_{l=0}^{j}p_{l,j}\sum_{n=0}^{j-k}r_{k,n,j-k}\alpha_{i,l+m+n}^{\pm}\right\}. \quad (55)$$

Finally, let us recall the sequence of formulas for calculating the reflectivity and transmissivity of a medium of finite optical depth using two methods in the case of nonconservative scattering:

$$\text{first method: } (33), (34), (54), (55), (53), (52), (12), (9), (4), (5); \tag{56}$$

$$\text{second method [10]: } (19), (18), (20), (13), (22), (23), (10), (11), (9), (4), (5). \tag{57}$$

The relation between the matrices of the linear equations, D_{im} and G_{jm}, is given by (42), (43). Note that all the formulas describing scattering in a semi-infinite medium have been numerically tested for $N \leq 20$. The case of conservative scattering can be calculated using (57).

Sobolev [1] reduced the problem of light scattering in a medium with arbitrary indicatrix to finding the auxiliary polynomials $q_i(\mu)$ and $s_i(\mu)$. Sobolev proposed two methods for doing this:

(1) solution of a system of linear algebraic equations for the polynomials,

(2) solution of a system of linear integral equations.

Until now, the second method has been used. In this paper, we have investigated the first method. We transformed the linear algebraic equations for the polynomials $q_i(\mu)$ and $s_i(\mu)$ to linear equations for the polynomial coefficients. We considered the case of an arbitrary number of terms in the expansion of the phase function and derived formulas relating the matrices of the linear equations obtained in the two methods. In the case of conservative scattering, the system of equations obtained using the first method is incomplete. We have presented a sequence of formulas defining the reflectivity and transmissivity of the medium for both types of solution and transformed them to a form convenient for computer calculations.

REFERENCES

1. V. V. Sobolev, *Scattering of Light in Planetary Atmospheres* [in Russian] (Nauka, Moscow, 1972).
2. V. V. Sobolev, Astron. Zh. **45**, 254, 528 (1968).
3. V. V. Sobolev, Astrofizika **5**, 1 (1969).
4. A. K. Kolesov and V. V. Sobolev, Tr. Astron. Obs. Leningrad. Gos. Univ. **26**, 3 (1969).
5. A. K. Kolesov and O. I. Smoktiĭ, Astron. Zh. **47**, 397 (1970).
6. A. K. Kolesov and O. I. Smoktiĭ, Astron. Zh. **48**, 1004 (1971).
7. D. N. Rachkovskiĭ, Pis'ma Astron. Zh. **22** (4), 284 (1996).
8. D. N. Rachkovskiĭ, Astron. Zh. **73**, 141 (1996).
9. D. N. Rachkovskiĭ, Astron. Zh. **74**, 913 (1997).
10. D. N. Rachkovskiĭ, Astron. Zh. **75**, 777 (1998).
11. T. W. Mullikin, Astrophys. J. **147**, 858 (1967).

Translated by G. Rudnitskiĭ

Southern Isolated Galaxy Triplets

V. E. Karachentseva* and I. D. Karachentsev**

*Astronomical Observatory, Kiev State University, ul. Observatoriya 3, Kiev, 252053 Ukraine
**Special Astrophysical Observatory, Russian Academy of Sciences, Nizhni Arkhyz, Stavropol kraĭ, 357147 Russia
Received August 11, 1999

Abstract—Seventy-six isolated triple systems of galaxies with declinations $\delta < -3°$ were selected using ESO/SERC and POSS-I sky survey data. The equatorial coordinates, configuration types, angular sizes, component angular separations, component morphological types, total magnitudes, and other parameters are reported for each triplet. Radial-velocity estimates are available for all components in 33 of the 76 triplets. The median values of the main dynamical parameters—radial-velocity dispersion, mean harmonic radius, absolute magnitudes of member galaxies, and mass-to-luminosity ratios—are similar to those obtained earlier for 83 isolated triple systems with $\delta > -3°$. © *2000 MAIK "Nauka/Interperiodica".*

1. INTRODUCTION

As the least populated group of galaxies, triplets provide a link between single and binary galaxies, on the one hand, and rich groups and clusters of galaxies, on the other hand. Triple systems of galaxies are of special interest from a dynamical point of view (the three-body problem). Triplet studies are also important for elucidating the role of these systems as an intermediate stage in the evolution of groups of galaxies.

A list of isolated triple systems of galaxies published in 1979 [1] contained a total of 83 triplets with component apparent magnitudes no fainter than $m_p \leq 15.7$ and declinations $\delta > -3°$. Selection of the galaxies was based on analysis of data from the Palomar sky survey and the catalog of Zwicky *et al.* [2]. We used an empirical isolation criterion to distinguish triple systems allowing for foreground and background galaxies, which resulted in a triplet surface-density contrast of ~10 above the overall background.

Only 20% of the galaxies in [1] had measured radial velocities at the time the list was published. We subsequently obtained spectroscopic observations of the triplet member galaxies from 1977 through 1988 using the 6-m telescope of the Special Astronomical Observatory of the Russian Academy of Sciences [3, 4]. In 1988, we published a complete list of radial velocities and the reduced data for the triplets in a catalog of triple galaxies (CTG) [5]. The dynamical properties of the triplets have been analyzed in considerable detail by Karachentsev *et al.* [6].

Various methods have yielded a median virial mass-to-luminosity ratio of $30f_\odot$ for physical triplets, implying about a fourfold excess of the virial mass in triplets compared to single and binary galaxies. Applying the results of numerical simulations of the apparent distribution of galaxies [7] to the CTG, we found that a substantial fraction of the virial excess can be explained by contamination of the triplet sample with nonisolated triple configurations formed by fragments of larger groups of galaxies [6]. For the past ten years, the complete and homogeneous CTG sample has provided an observational basis for studies of the origin and evolution of galaxy triplets via computer simulations. The review [8] summarizes the results obtained in this field by research groups in Russia, Finland, and the USA.

Isolated triple galaxy systems represent an extremely important case of special structures in the Universe. Accordingly, we decided to compile a catalog of southern triple galaxies using the same criterion as in [1].

2. DESCRIPTION OF THE SOUTHERN ISOLATED TRIPLE GALAXY SAMPLE

As the observational basis for our search for isolated southern triplets, we used the ESO/SERC sky survey and the catalog of Lauberts [9] for declinations $-90° < \delta < -20°$ (down to a limiting diameter of $a_{\lim} \simeq 1$ arcmin), and the POSS-I sky survey and Morphological Catalog of Galaxies (MCG) [10] ($m_{\lim} \simeq 15$) for declinations $-21° < \delta < 3°$. As with the CTG, we excluded maps with a low Galactic latitude ($|b| < 20°$). We applied our criterion for local isolation to all galaxies from [9] and to all galaxies from [10] with diameters $a \geq 0.85$ arcmin. This difference in the limiting minimum sizes is dictated by the different limiting magnitudes of the ESO/SERC and POSS-I surveys [9].

Three galaxies were taken to form an isolated system if their distances from important neighbors exceeded the mutual separations between the triplet components by at least a factor of three. We defined important neighbors to be surrounding galaxies with angular diameters equal to 0.5–2 times that of the triplet component considered. As in the CTG, we included a galaxy in a triplet irrespective of its radial velocity, so that the resulting system could be isolated in the plane of the sky but not in real three-dimensional space.

Our list of southern triplets contains a total of 76 systems, or about 1% of all the galaxies in the catalog of Lauberts [9] and the MCG. The corresponding fraction for northern triplets is 0.8%. Table 1 presents a list of

Table 1. List of isolated southern galaxy triplets

TS	Isolation	R.A. (1950)	Dec. (1950)	a	b	X_{ij}	Confi-guration	Type	Identi-fication	B_t	$v \pm \sigma$, km/s
1	2	3	4	5	6	7	8	9	10	11	12
1A	+	00^{h}07^{m}49^s	−46°41′50″	2′.17	0′.54	4′.47	D	SBb	241-21	14.26	6071 ± 61
1B	−	00 07 54	−46 46 14	1.08	0.45	4.71		SBbc	241-22	14.17	
1C	+	00 07 56	−46 41 29	0.59	0.59	1.34		Sc			
2A	+	00 33 40	−32 52 48	0.90	0.45	1.94	D	Sa	350-37	14.49	
2B	−	00 33 44	−32 51 03	0.68	0.39	11.27		Sa			
2C	+	00 34 36	−32 48 17	1.18	0.45	12.58		S0-a	350-39	15.83	14803 60
3A	+	00 33 59	−28 03 37	0.99	0.44	2.20	T	S0-a	410-24	14.57	10431 52
3B	+	00 34 09	−28 03 49	0.99	0.57	2.01		E-S0	410-25	15.09	6910 52
3C	+	00 34 14	−28 05 32	0.86	0.09	3.81		Sc	410-26	16.29	
4A	+	00 34 10	−22 52 06	1.08	0.22	8.07	L	S0-a	474-4	14.92	3890 60
4B	+	00 34 45	−22 51 36	2.26	0.27	5.31		SBbc	474-5	14.08	2965 62
4C	+	00 35 06	−22 49 24	2.26	0.53	13.17		Sab	474-6	14.16	3858 54
5A	+	00 36 04	−24 36 54	1.18	0.44	3.93	T	SBb	474-8	14.98	3764 9
5B	+	00 36 06	−24 33 00	1.72	1.67	4.44		SBc	474-9	13.62	3681 39
5C	−	00 36 20	−24 29 52	0.54	0.44	7.89		Sdm			
6A	+	00 44 23	−52 23 02	0.82	0.17	4.74	D	Sb			
6B	+	00 44 44	−52 19 28	0.82	0.48	0.75		Sa}	194-39}	14.99}	8185 118
6C	+	00 44 49	−52 19 24	0.90	0.10	5.35		Scd			
7A	+	00 48 16	−07 09 26	2.35	0.56	10.90	D	S0	-1-3-19	13.87	4753 60
7B	+	00 48 30	−07 19 42	0.95	0.67	0.70		E	-1-3-21	12.71	1750 11
7C	+	00 48 32	−07 20 14	1.23	1.01	11.50		SBc	-1-3-22	12.63	1744 8
8A	+	01 10 13	−58 30 42	1.81	0.96	3.11	T	SBab	113-23	12.77	4849 103
8B	+	01 10 29	−58 28 24	1.36	0.52	5.05		SO-a	113-24	15.66	4828 8
8C	+	01 10 48	−58 32 48	0.82	0.52	5.03		Sbc	113-25	13.67	5015 93
9A	+	01 18 09	−17 39 30	1.68	0.67	0.60	D	Sb	-3-4-53	14.51	5961 48
9B	+	01 18 09	−17 38 55	1.12	0.22	2.75		SBb	-3-4-52	14.67	5927 60
9C	+	01 18 09	−17 36 10	1.23	0.67	3.35		E	-3-4-51	14.45	9296 68
10A	+	01 18 45	−61 35 36	1.08	0.79	6.71	D	SBab	113-40	15.11	
10B	+	01 19 37	−61 38 12	1.36	0.79	1.32		SBb	113-41	15.04	8622 42
10C	+	01 19 39	−61 36 54	0.82	0.61	6.55		E-S0	113-42	14.72	
11A	+	01 28 24	−23 50 42	0.99	0.57	6.80	L	SBc	476-17	14.91	
11B	+	01 28 53	−23 52 12	0.68	0.52	5.99		Sa			
11C	−	01 29 19	−23 51 23	0.76	0.16	12.60		Sbc			
12A	+	01 40 21	−83 37 00	2.08	0.70	10.38	T	SBc	3-3	14.56	4934 40
12B	+	01 43 06	−83 27 48	1.81	0.35	14.10		Sbc	3-4	14.85	4595 41
12C	+	01 48 13	−83 38 55	0.63	0.96	13.29		E-S0			
13A	+	01 42 52	−42 14 41	0.90	0.12	7.19	T	Sbc	297-26	16.08	
13B	+	01 43 03	−42 07 48	1.45	0.88	7.90		Sb	297-27	14.89	6317 48
13C	+	01 43 37	−42 12 24	0.90	0.22	8.64		Sbc	297-28	16.51	
14A	+	01 46 05	−52 17 55	0.72	0.52	0.67	L	SO-E			
14B	+	01 46 10	−52 17 57	0.80	0.07	0.84		Sc}	197-1	15.32	14708 60
14C	+	01 46 14	−52 17 37	0.99	0.28	1.46		Sa			
15A	+	01 50 06	−19 01 09	1.12	1.01	2.63	D	Sc	-3-5-26	14.35	
15B	+	01 50 17	−19 01 39	1.01	0.67	12.48		Sc	-3-5-27	14.47	14580 60
15C	+	01 50 52	−19 11 00	1.34	0.25	14.67		Sa	-3-5-28	15.22	
16A	+	02 19 34	−21 03 07	1.90	1.58	5.15	D	Irr	545-7	13.14	1563 11
16B	+	02 19 42	−20 58 20	1.13	0.61	14.37		Irr	545-8	14.15	1580 6
16C	+	02 20 43	−20 56 24	2.99	0.61	17.45		SBd	545-10	13.19	1726 11
17A	+	02 29 07	−44 38 48	1.08	0.48	2.20	D	SBc	246-22	14.83	5127 60
17B	−	02 29 07	−44 36 36	0.54	0.48	10.55		Sc			
17C	+	02 29 45	−44 44 42	1.63	1.14	8.98		S0	246-23	13.70	4775 9
18A	+	02 37 02	−08 20 54	2.69	0.90	22.56	T	Sc	-1-7-27	12.88	1241 7
18B	+	02 37 57	−08 38 52	5.60	4.14	14.57		SBc	-2-7-54	11.46	1373 8
18C	−	02 38 37	−08 28 10	2.58	2.02	24.60		E	-1-7-34	11.36	1507 40
19A	+	02 40 14	−12 38 01	1.12	0.67	1.04	D	E	-2-7-73	14.21	4285 34
19B	+	02 40 18	−12 38 22	1.12	0.25	2.09		Sa	-2-7-74	15.68	4246 39
19C	+	02 40 22	−12 36 31	1.34	0.56	2.46		Sm	-2-7-75	15.39	4160 41

Table 1. (Contd.)

TS	Isolation	R.A. (1950)	Dec. (1950)	a	b	X_{ij}	Configuration	Type	Identification	B_t	$v \pm \sigma$, km/s	
1	2	3	4	5	6	7	8	9	10	11	12	
20A	−	03^{s}28^{h}29^m	−48°01′54″	0.63	0.44	9.88	D	S0-a	200-29	14.16	6635 ±	62
20B	+	03 29 15	−48 08 07	0.77	0.66	0.94		Sbc	200-32	15.54	13800	190
20C	+	03 29 18	−48 08 54	0.95	0.66	10.79		Sbc	200-33	13.70	6964	213
21A	+	03 34 09	−25 46 12	1.36	0.35	3.84	D	Sbc	482-11	15.21		
21B	−	03 34 17	−25 49 36	0.63	0.17	0.46		S0				
21C	+	03 34 19	−25 49 30	0.90	0.35	4.00		Sb	482-12	16.01		
22A	+	03 52 17	−20 34 24	0.84	0.45	5.06	T	E	-3-10-53	14.52		
22B	+	03 52 27	−20 38 54	1.57	1.01	9.27		Sa	-3-10-54	13.14	1859	8
22C	+	03 52 52	−20 31 42	1.12	1.01	8.62		Sc	-3-10-55	15.51		
23A	+	03 59 23	−67 46 30	4.34	1.58	11.14	T	Sa	55-4	11.85	1341	14
23B	+	04 00 08	−67 56 48	1.99	0.35	12.22		SBa	55-5	14.16	1323	8
23C	+	04 00 42	−67 45 00	2.17	0.27	7.61		SBcd	55-6	15.06		
24A	+	04 13 47	−40 48 19	0.54	0.44	1.48	L	E				
24B	+	04 13 52	−40 47 08	0.45	0.27	1.28		S(r)				
24C	+	04 13 57	−40 46 15	1.18	0.53	2.78		Sc	303-6	15.86		
25A	+	04 26 34	−48 01 12	1.63	1.40	6.78	D	Spec	202-23	13.47	4913	61
25B	+	04 26 56	−47 55 30	1.45	1.05	2.91		E	202-25	13.68	4696	53
25C	+	04 27 08	−47 53 24	1.27	0.74	9.66		SBc	202-26	13.81	5105	29
26A	+	04 37 01	−24 16 54	1.08	0.44	1.13	D	Sc	485-3	14.53	4486	77
26B	+	04 37 06	−24 16 42	1.54	0.13	16.53		Sc	485-4	15.99	4409	47
26C	+	04 38 09	−24 24 54	1.08	0.96	17.44		SBc	485-6	14.58	4422	42
27A	−	04 49 41	−61 19 54	0.98	0.74	5.90	D	Sc	119-12	14.56	5941	60
27B	+	04 49 50	−61 25 42	1.27	1.09	1.66		SBc	119-13	13.67	5903	40
27C	+	04 50 03	−61 26 18	1.18	0.61	6.92		Scd	119-14	15.06		
28A	+	04 56 56	−11 11 35	3.25	1.68	1.67	L	SBb	-2-13-27	13.15	4607	134
28B	+	04 57 02	−11 12 24	1.23	1.01	1.34		S0	-2-13-28	13.70	3998	122
28C	+	04 57 07	−11 11 49	1.79	0.67	2.69		Sa	-2-13-30	14.76	4301	291
29A	+	04 58 52	−75 29 48	1.99	0.96	1.45	L	SBbc	33-4	14.04	5192	60
29B	+	04 58 58	−75 31 12	0.95	0.52	1.35		Sab	33-5	14.21		
29C	−	04 59 16	−75 31 58	0.45	0.27	2.62		Pec				
30A	+	05 14 00	−62 13 34	1.04	0.27	3.44	T	Sb	119-46	14.95	4966	60
30B	+	05 14 02	−61 17 00	1.08	0.66	3.76		SBb	119-47	13.98	5100	63
30C	−	05 14 22	−61 14 03	0.82	0.35	2.60		S0-a				
31A	+	05 14 03	−53 47 36	2.54	2.02	23.79	D	SBbc	159-2	13.71	4290	8
31B	+	05 15 06	−54 09 30	2.17	1.31	8.94		S0	159-3	13.97	3902	60
31C	−	05 16 05	−54 07 12	1.27	0.61	26.59		S0-a	159-4	14.45	10300	190
32A	+	06 18 56	−20 01 24	3.71	1.31	10.50	T	SBa	556-15	12.71	1981	11
32B	+	06 19 36	−20 06 06	1.18	0.52	6.01		Sbc	556-18	15.80		
32C	+	06 19 41	−20 12 00	1.53	1.49	14.96		SBm	556-19	14.96	1868	8
33A	+	06 19 26	−57 33 12	1.90	0.52	2.80	L	Sa	121-24	13.79	2442	96
33B	+	06 19 27	−57 30 24	1.08	0.35	2.93		SBa	121-25	14.14	2601	47
33C	+	06 19 40	−57 28 18	1.27	0.52	5.25		SBd	161-1	14.74		
34A	+	08 17 48	−67 25 12	1.27	0.74	2.46	T	SBc	89-15	14.31		
34B	+	08 18 03	−67 27 12	1.08	0.61	7.35		E	89-16	14.39		
34C	+	08 18 37	−67 20 36	1.36	0.70	6.58		E	89-17	13.67		
35A	+	08 24 44	−77 41 18	1.36	0.61	2.04	L	SBbc	18-7	13.52	5291	87
35B	+	08 24 52	−77 39 18	0.99	0.44	3.48		Sc	18-8	14.40	5432	87
35C	+	08 25 41	−77 37 00	0.82	0.79	5.26		Sb	18-9	13.80	5313	27
36A	+	08 54 27	−20 21 54	1.36	0.52	3.53	T	Sm	563-33	14.40		
36B	+	08 54 40	−20 20 06	1.18	0.79	4.55		Sab	563-34	13.86		
36C	+	08 54 55	−20 23 00	1.36	0.79	6.64		Sa	563-36	13.61	2630	60
37A	−	09 52 12	−32 52 48	1.45	0.27	9.74	D	Sb	374-8	15.62	1510	60
37B	+	09 52 58	−32 54 00	3.34	1.84	4.40		Sb	374-10	12.6	3012	
37C	+	09 52 59	−32 58 24	1.53	0.78	11.34		SBbc	374-11	13.65	2601	44
38A	+	10 03 36	−15 52 46	2.35	1.01	6.75	T	Sb	-3-26-20	14.31	4635	10
38B	+	10 03 50	−15 46 54	2.35	0.34	6.49		Sc	-3-26-21	14.89	5009	7
38C	+	10 04 01	−15 52 55	1.57	0.31	5.77		Sb	-3-26-22	14.62	4536	43

Table 1. (Contd.)

TS	Isolation	R.A. (1950)	Dec. (1950)	a	b	X_{ij}	Confi-guration	Type	Identi-fication	B_t	$v \pm \sigma$, km/s	
1	2	3	4	5	6	7	8	9	10	11	12	
39A	+	$10^s30^h37^m$	$-07°05'55''$	0.95	0.50	0.58	D	Sc	-1-27-16	15.11		
39B	+	10 30 39	−07 05 37	0.90	0.67	6.87		Sa	-1-27-17	15.57		
39C	+	10 30 43	−07 12 25	1.01	1.01	6.67		S0	-1-27-18	14.02	4942 ± 44	
40A	−	10 36 55	−30 02 18	3.34	1.05	11.24	T	SBbc	437-30	13.73	3773	15
40B	+	10 37 38	−29 56 00	1.63	1.05	4.59		SBa	437-33	13.72	3338	148
40C	+	10 37 44	−30 00 24	1.81	0.79	10.78		SBbc	437-35	14.26	3445	65
41A	−	10 49 55	−32 24 18	2.35	2.20	17.18	L	SBab	437-67	13.60	3162	25
41B	+	10 50 32	−32 39 36	3.53	1.05	19.42		SBab	376-25	12.83	3290	15
41C	+	10 51 46	−32 51 11	1.81	1.05	35.67		S0-a	376-26	13.52	3478	149
42A	+	11 14 25	−25 51 36	1.27	0.17	12.97	T	Sbc	503-8	15.81		
42B	+	11 15 17	−25 46 00	1.72	0.96	5.86		SBc	503-11	15.55	2047	9
42C	+	11 15 23	−25 51 42	1.63	1.14	13.05		E	503-12	13.60	2205	42
43A	+	11 24 37	−28 42 12	2.08	1.75	17.25	D	S0-a	439-8	13.21	1636	30
43B	+	11 24 55	−28 59 00	1.53	0.44	5.28		Sa	439-9	14.79	7137	102
43C	+	11 25 04	−28 54 06	1.72	0.66	13.28		Sb	439-10	15.77	7164	34
44A	+	12 12 08	−35 13 54	2.99	1.40	5.77	T	SBb	380-1	12.90	2689	6
44B	+	12 12 18	−35 19 18	1.18	0.44	8.14		Sbc	380-2	15.30	2626	44
44C	+	12 12 57	−35 21 06	3.53	1.40	12.31		Sb	380-6	12.63	2943	8
45A	+	12 37 59	−36 27 55	1.36	0.13	2.65	T	Sc	381-6	15.93	3180	60
45B	+	12 38 11	−36 29 00	1.08	0.96	1.79		SBbc	381-8	13.19	3396	160
45C	+	12 38 16	−36 27 30	1.45	1.14	3.44		SBbc	381-9	13.93	3302	71
46A	+	12 47 57	−09 10 46	1.01	0.56	4.16	D	S0	-1-33-21	13.74	4645	109
46B	+	12 47 58	−09 14 53	1.40	0.67	3.43		Scd	-1-33-22	14.62		
46C	+	12 47 58	−09 11 28	1.57	0.34	0.76		SBa	-1-33-23	15	4515	96
47A	+	13 37 00	−50 47 00	0.99	0.83	6.45	T	Sbc	220-27	14.02	4045	49
47B	+	13 37 05	−50 53 24	1.90	0.24	5.15		Sbc	220-28	14.73	3639	10
47C	+	13 37 23	−50 49 06	0.82	0.70	4.19		S0	220-29	13.37	4031	106
48A	+	13 46 22	−06 56 54	2.58	0.45	3.43	D	Sb	-1-35-13	15.07	7644	41
48B	+	13 46 34	−06 58 35	1.34	0.78	0.93		S0	-1-35-14	13.10	7246	36
48C	−	13 46 35	−06 57 41	0.78	0.34	3.31		Sb	-1-35-15	15.66	7368	104
49A	+	13 47 35	−37 02 30	2.44	0.27	22.71	T	SBcd	383-91	14.35	1079	8
49B	−	13 48 25	−37 22 54	1.72	0.27	14.87		Sb	384-3	14.37	3849	129
49C	+	13 49 19	−37 12 36	2.26	0.22	23.04		SBd	384-5	15.41	1640	8
50A	+	14 21 00	−28 27 42	1.36	0.70	7.32	T	SBbc	446-58	13.50	4347	10
50B	+	14 21 30	−28 24 30	1.27	0.30	5.61		Sbc	446-59	15.28		
50C	+	14 21 37	−28 29 54	1.04	0.16	8.42		Sbc	446-60	16.21		
51A	+	14 44 33	−22 11 54	1.08	0.70	14.98	L	Scd	580-25	14.34		
51B	+	14 44 36	−21 56 56	1.36	0.79	7.26		S0	580-26	14.92	3194	133
51C	+	14 44 37	−22 04 12	1.90	1.49	7.55		SBa	580-27	13.66	3286	9
52A	+	14 46 48	−09 57 58	2.80	1.12	0.80	D	Scd	-2-38-16	13.38	1859	20
52B	+	14 46 50	−09 57 19	1.90	0.56	5.45		Sdm	-2-38-17	14.28	1856	10
52C	+	14 46 53	−09 51 55	0.90	0.34	6.15		Irr				
53A	+	14 58 20	−37 47 48	2.26	0.44	3.87	T	Sa	328-5	15.0		
53B	+	14 58 33	−37 44 54	0.90	0.79	3.87		SBc	328-6	14.58	4434	60
53C	+	14 58 51	−37 46 24	1.36	0.22	6.28		Sbc	328-7	14.76		
54A	+	17 06 19	−77 28 30	3.71	2.20	6.69	L	Sc	44-3	12.40	2941	7
54B	+	17 08 12	−77 25 54	3.26	0.61	17.15		SBb	44-5	13.94	2948	8
54C	+	17 12 28	−77 18 42	1.72	0.30	22.52		SBcd	44-10	14.61		
55A	+	17 15 10	−80 00 54	1.18	1.05	5.01	T	SBcd	24-1		4845	60
55B	+	17 15 18	−80 05 54	1.27	1.23	5.56		Sc	24-2	13.80	5330	60
55C	+	17 17 08	−80 08 54	1.36	0.52	9.47		S0	24-5		4872	60
56A	−	17 23 33	−85 16 30	2.26	1.49	51.61	D	Sbc	9-10		2422	8
56B	+	18 05 51	−85 25 06	1.18	0.88	0.58		S0	10-1	12.13	2437	21
56C	+	18 06 18	−85 25 18	2.08	0.79	53.18		Irr	10-2	12.39	2515	9
57A	+	18 09 19	−57 44 48	0.32	0.30	0.42	L	Pec	140-9	14.77	4960	62
57B	+	18 09 20	−57 44 24	1.63	1.05	1.41		Sb	140-10	14.28	5189	35
57C	+	18 09 21	−57 45 48	0.82	0.30	1.04		Sa	140-11	15.00	5140	156

Table 1. (Contd.)

TS	Isolation	R.A. (1950)	Dec. (1950)	a	b	X_{ij}	Confi-guration	Type	Identi-fication	B_t	$v \pm \sigma$, km/s
1	2	3	4	5	6	7	8	9	10	11	12
58A	+	$18^s31^h32^m$	$-67°16'23''$	0.′54	0.′48	0.′87	L	SBa			
58B	+	18 31 37	−67 17 06	1.08	0.44	2.13		Sb	103-29	15.34	
58C	+	18 31 47	−67 19 00	1.08	0.27	3.00		Sbc	103-30	15.65	
59A	+	19 13 57	−60 35 30	1.90	1.14	1.85	T	SBb	141-48	12.57	3810 ±119
59B	+	19 14 12	−60 35 18	2.44	2.19	2.91		SBb	141-49	12.76	3834 96
59C	−	19 14 14	−60 38 12	2.35	0.44	3.41		S0-a	141-50	13.57	4221 76
60A	+	19 26 46	−39 30 49	0.73	0.39	0.68	T	Sab}	338-8}	16.73}	2835 67
60B	+	19 26 49	−39 31 09	0.45	0.24	0.24		Pec			
60C	+	19 26 50	−39 31 01	0.73	0.27	0.80		Pec			
61A	−	19 57 21	−47 13 22	0.99	0.27	0.85	L	Sa			
61B	+	19 57 21	−47 12 30	1.90	0.61	1.50		Sb}	284-8}	13.83}	6348 75
61C	+	19 57 29	−47 11 51	1.08	0.57	2.02		Sbc			
62A	+	20 27 52	−25 31 54	0.77	0.13	0.49	D	Sb	528-13	15.57	
62B	+	20 27 54	−25 32 06	0.82	0.27	3.76		Sa	528-14	15.24	
62C	+	20 27 58	−25 28 27	0.68	0.10	3.71		Sb			
63A	+	20 45 19	−20 02 27	0.63	0.44	1.45	T	E-S0			
63B	+	20 45 19	−20 01 00	0.86	0.27	1.37		Sa			
63C	+	20 45 23	−20 02 00	1.36	0.24	1.04		Sb	597-36	15.22	8694 41
64A	+	20 55 37	−20 10 30	1.27	0.44	9.87	L	Sb	598-9	14.38	
64B	+	20 56 15	−20 14 12	1.36	0.96	15.07		Sc	598-11	15.74	
64C	−	20 57 07	−20 19 22	0.90	0.52	22.89		S0			
65A	+	21 41 35	−49 14 10	0.82	0.48	0.95	D	Sm			
65B	+	21 41 39	−49 14 51	0.63	0.35	3.15		E-S0			
65C	+	21 41 58	−49 14 18	0.82	0.35	3.76		Irr	236-39	15.08	
66A	+	21 59 09	−32 12 54	1.18	0.79	1.27	T	E	466-39	12.86	2548 75
66B	+	21 59 12	−32 14 00	1.36	0.61	0.43		Sab	466-40	13.85	2754 88
66C	+	21 59 14	−32 13 54	1.08	0.70	1.44		E	466-41	12.39	2528 28
67A	+	22 12 33	−46 06 00	2.54	0.79	1.91	T	S0-a	289-7	12.87	2152 8
67B	+	22 12 44	−46 05 48	1.53	1.05	4.26		SBa	289-8	13.10	1915 8
67C	+	22 12 48	−46 01 48	1.72	1.40	4.94		SBm	289-9	13.87	2042 42
68A	+	22 13 44	−21 40 54	2.26	1.84	4.17	D	SBa	602-1	12.70	2616 11
68B	−	22 13 55	−21 44 12	1.08	0.70	13.72		SBa	602-2	14.75	9634 22
68C	+	22 14 06	−21 30 00	2.08	0.70	12.04		Irr	602-3	14.70	2571 11
69A	+	22 14 47	−47 09 28	0.73	0.16	0.34	L	Sa			
69B	+	22 14 48	−47 09 25	0.63	0.13	0.27		Pec}	289-14}	16.28	
69C	+	22 14 48	−47 09 30	0.30	0.10	0.57		S0-E			
70A	+	22 33 50	−12 49 36	1.57	0.67	4.33	T	Sa	-2-57-22	14.38	7504 73
70B	+	22 34 07	−12 48 20	1.12	0.39	2.18		S0-a	-2-57-23	14.35	7248 11
70C	−	22 34 15	−12 49 18	1.01	0.56	6.09		Sc	-2-57-24		7159 60
71A	+	23 11 37	−03 03 08	0.90	0.56	4.16	L	S0-a	-1-59-4	15.00	3475 60
71B	+	23 11 48	−03 00 00	1.23	0.56	1.99		S0-a	-1-59-5	13.85	3555 17
71C	+	23 11 52	−02 58 17	0.78	0.50	6.12		Ir	-1-59-6	14.54	3521 47
72A	+	23 21 01	−19 17 06	1.63	1.40	12.86	T	Sc	605-4	14.71	7677 60
72B	+	23 21 54	−19 20 06	1.36	1.31	14.02		S0p	605-5	14.41	7632 71
72C	−	23 22 24	−19 08 00	0.82	0.35	21.60		Sc	605-6	15.94	
73A	+	23 22 31	−58 03 54	1.07	0.96	6.17	T	Sb	148-10	13.44	3380
73B	+	23 22 47	−58 09 42	1.36	0.61	10.46		Sa	148-11	14.45	
73C	+	23 23 57	−58 04 48	1.40	0.27	11.40		SBd	148-12	14.67	3138 43
74A	+	23 35 03	−47 46 54	2.44	1.23	13.32	T	S0	240-10	12.59	3189 31
74B	+	23 35 08	−48 00 12	5.34	0.52	16.66		Sc	240-11	13.19	2843 6
74C	−	23 36 46	−48 03 00	1.40	0.96	23.58		SBb	240-13	14.00	3246 31
75A	+	23 35 11	−38 32 58	0.90	0.27	1.59	T	Sbc	347-32	15.88	
75B	+	23 35 12	−38 31 23	0.82	0.17	3.62		Sbc			
75C	+	23 35 25	−38 33 59	0.73	0.10	2.92		Sc			
76A	+	23 50 43	−41 04 57	1.08	0.10	0.77	L	Scd			
76B	+	23 50 47	−41 05 07	1.08	0.44	0.74		Sp}	293-8}	15.09}	9057 86
76C	+	23 50 50	−41 05 40	0.54	0.17	1.49		S0			
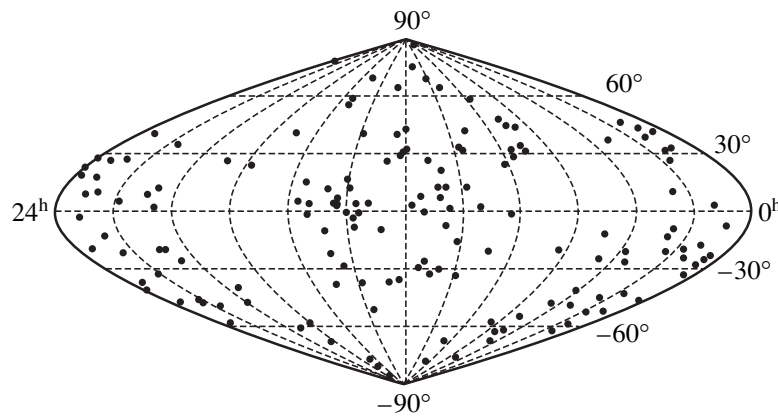
Distribution of the centers of the northern and southern triplets in equatorial coordinates.

the southern triplets. The columns in this table contain the following information.

(1) A running number for the triplet followed by a component designation (A, B, C, in order of increasing right ascension).

(2) A flag indicating whether the corresponding component fulfils the adopted isolation criterion ("+" and "–" mean "yes" and "no," respectively). Completely isolated triplets make up 67% of the entire sample; the corresponding fraction for northern triplets is 64%.

(3), (4) The right ascension and declination at epoch 1950.0. The coordinates for MCG galaxies and for objects absent from [9] were determined using the Digital Sky Survey.

(5), (6) The major and minor axes of the galaxy in arcmin measured down to the seeing limit on the "blue" (O) prints and J plates. For the sake of consistency, we reduced the diameters measured on the ESO/SERC survey plates to the POSS-I system using the relations [11] $a_O = 0.8078a_J$ and $b_O = 0.7827b_J$.

(7) The angular separations X_{ik} in arcmin; the upper, middle, and last rows refer to X_{AB}, X_{BC}, and X_{CA}, respectively. The distribution of X_{ik} peaks at ~1.5 arcmin; the corresponding distribution for northern triplets peaks at ~2 arcmin.

(8) The type of configuration, as defined in [1]: D—hierarchical (one side of the apparent triangle is shorter than one-third of each of the other two), L—linear (one angle in the triangle exceeds 150°), and T—triangular (all three sides and angles are comparable). The triplet configuration types are distributed as follows: D—34%; T—42%, and L—24% (the corresponding fractions for the northern triplets are 38, 49, and 13%, respectively).

(9) The morphological type of the galaxy as determined from its appearance on the blue and red sky-survey plates/prints. The percentages of galaxies having morphological types E, S0, Sa, Sb, Sc, and Sm + Pec are 9, 13, 17, 31, 19, and 11, respectively. The corresponding percentages for northern triplets are 16, 12,

21, 28, 18, and 5, respectively. The relative deficit of early-type galaxies and excess of irregular galaxies among southern triplets compared to the northern sample could be due to the higher resolution of the photographic emulsion on the ESO/SERC prints, which enables the identification of morphological features that are barely visible on the POSS-I prints; this possibility could be tested by redetermining the morphological types of the galaxies in the northern triplets using, e.g., the POSS-II prints.

(10) Cross-identifications with catalogs [9] and [10]. Other cross-identifications can be found in various databases. Twelve percent of southern triplet members are not present in the catalogs known to us.

(11) The total apparent magnitude of the galaxy adopted from the Lyon–Meudon Extragalactic Database. The braces in columns 9–11 indicate the parameters of merged components (written for the object with the lowest right ascension).

(12) The measured radial velocity and its standard error from the Lyon–Meudon Extragalactic Database. Either optical or radio radial-velocity measurements are available for 62% of the triplet member galaxies; the median radial velocity for the sample is 4000 km/s (the corresponding value for the northern triplets is 5465 km/s). Thirty-three triplets (43%) have measured radial velocities for all three components.

Digital Sky Survey (DigSS) triplet images are given in the Appendix to this paper. For convenience, we first present images for close triplets; then pair-plus-third-component triplets; and, finally, the individual components of wide triplets. Each plate is 5×5 arcmin² in size. North is at the top and east to the left.

The figure shows the overall distribution of the centers of northern and southern triplets in equatorial coordinates.

Table 2. Integrated parameters of southern triplets

TS	$\langle v \rangle$, km/s	s_v, km/s	r_H, kpc	L, $10^{10} L_\odot$	$\log \tau$	$f, f_\odot$	$f^c, f_\odot$
4	3623	429	108.7	4.5	−1.42	1380.0	1380.0
7	2864	1417	20.8	6.7	1.01	2089.0	2089.0
8	4767	84	77.3	10.0	−0.86	169.8	111.6
9	7109	1580	35.3	10.4	−2.48	2818.0	2818.0
16	1608	73	58.3	1.5	−0.92	67.6	67.5
18	1396	109	105.9	4.1	−0.84	102.3	99.2
19	4233	52	26.6	2.5	−1.12	9.5	6.1
20	8967	3303	83.2	15.6	−2.42	19498.0	19498.0
25	4703	167	92.0	7.3	−1.08	117.5	110.4
26	4295	34	49.8	3.0	−0.66	6.5	−5.6
28	4187	249	28.4	8.8	−1.77	64.6	37.5
31	5926	2929	360.3	9.2	−1.73	112202.0	112202.0
35	5075	62	61.0	11.1	−0.83	6.5	0.5
37	2068	634	57.5	2.9	−1.87	2630.0	2630.0
38	4458	204	109.1	5.5	−1.10	275.4	275.4
40	3223	185	93.9	4.3	−1.12	251.2	208.5
41	3013	130	254.8	7.1	−0.53	199.5	137.6
43	5032	2599	181.6	7.2	−1.98	56234.0	56234.0
44	2481	137	76.5	5.3	−1.08	91.2	89.4
45	3032	88	28.8	3.1	0.57	24.0	0.02
47	3656	188	72.3	8.7	−1.64	97.7	88.9
48	7290	166	50.9	16.4	−1.34	28.8	25.6
49	1970	1196	148.2	1.6	−1.76	44668.0	44668.0
55	4802	223	115.1	7.5	−1.11	251.2	238.6
56	2235	41	14.7	9.4	−1.27	0.9	0.8
57	4969	98	14.3	5.0	−1.66	9.1	2.9
59	3837	188	38.0	13.7	−1.52	32.4	26.6
66	2667	102	8.2	5.3	−1.93	5.4	3.7
67	2016	97	24.3	2.5	−1.43	30.2	29.0
68	5052	2867	148.6	9.7	−2.10	40738.0	40738.0
70	7456	146	101.5	9.7	−0.68	56.2	50.1
71	3702	33	47.5	3.1	−0.67	5.5	−1.3
74	3047	178	199.8	8.0	−0.77	2630.0	2604.0

3. DYNAMICAL CHARACTERISTICS OF THE SOUTHERN TRIPLETS

A complete analysis of the dynamical conditions in southern triplets will be possible only after all radial velocities have been measured. Here, we report data for the 33 triplets with radial-velocity measurements for all three components. In accordance with [6], we consid-ered the triplets to be individual dynamical systems and computed the following quantities.

(1) The mean radial velocity

$$\langle v \rangle = \sum_{k=1}^{3} v_k / 3, \qquad (1)$$

Table 3. Median values of some triplet parameters

Parameter	Southern triplets (this paper), $N = 33$	All northern triplets, $N = 83$	Triplets with $s_v < 300$ km/s	
			southern, $N = 24$	northern, $N = 53$
s_v, km/s	166	133	119	100
r_H, kpc	72	63	60	55
L, $10^{10} \times L_\odot$	7.1×10^{10}	7.4×10^{10}	6.3×10^{10}	7.6×10^{10}
τ, H^{-1}	0.08	0.04	0.08	0.07
$f, f_\odot$	102	67	64	31
$f^c, f_\odot$	99	58	44	27

where v_k is the radial velocity of the kth component corrected for the solar motion in accordance with [12].

(2) The dispersion of galaxy velocities with respect to the center

$$s_v = \left[\frac{1}{3} \sum_{k=1}^{3} (v_k - \langle v \rangle)^2 \right]^{1/2}. \qquad (2)$$

(3) The projected separation between components

$$r_{ik} = X_{ik} \langle v \rangle H^{-1}, \qquad (3)$$

where X_{ik} are the mutual angular separations and H is the Hubble constant, which we take to be $H = 75$ km s^{-1} Mpc^{-1}.

(4) The mean harmonic projected distance

$$r_H = \left[\frac{1}{3} \sum_{i,k} r_{ik}^{-1} \right]^{-1}. \qquad (4)$$

(5) The luminosity of the galaxy in solar units

$$L_k = \mathrm{dex}[0.4(5.40 - M_k)], \qquad (5)$$

where the absolute magnitude M_k is computed from the mean radial velocity $\langle v \rangle$ of the triplet and its apparent magnitude B_t, corrected for Galactic [13] and internal [14] extinction. (We used formula (1) from [15] to compute the apparent magnitudes of galaxies TS55 A, C, TS56 A, TS70 C.)

(6) The dimensionless crossing time of the system

$$\tau = 2H r_H / s_v, \qquad (6)$$

expressed in units of the Hubble time, H^{-1}.

(7) The virial mass-to-luminosity ratio for the triplet in solar units,

$$f = M_{\mathrm{vir}} \left[\sum L_k \right]^{-1}, \quad i = 1, 2, 3, \qquad (7)$$

where

$$M_{\mathrm{vir}} = 3\pi N (N-1)^{-1} G^{-1} s_v^2 r_H, \quad N = 3, \qquad (8)$$

G is the gravitational constant, and $3\pi N(N-1)^{-1}$ is a constant that includes a mean projection factor, in accordance with [16]. (This virial mass cannot be con-

sidered the true mass, only a combination of the velocity dispersion s_v and scale length r_H of the triplet, which has the dimension of mass.)

(8) A statistically unbiased estimate of the virial mass-to-luminosity ratio,

$$f^c = f[1 - 2\sigma_v^2 / 3 s_v^2], \qquad (9)$$

where σ_v is the standard error of the measured radial velocities of the triplet components.

Table 2 gives the integrated parameters of the 33 isolated southern triplets. As is evident from this table, the parameters of southern triplets vary over a wide range. The mass-to-luminosity ratios span six orders of magnitude. Following the results of triple-galaxy modeling reported in [6], we subdivided our sample into physical (with $s_v < 300$ km/s) and optical (with $s_v > 300$ km/s) triplets. We then determined for each subsample the median values of the main parameters. These are listed in Table 3, which also gives for comparison the corresponding data for northern triplets from [6, 8].

This subsample is characterized by higher median s_v and r_H values and lower median total luminosities compared to those of the northern triplets. The median f and f^c values for the southern triplets are double the corresponding quantities for the northern triplets. However, we will be able to draw more final conclusions only after integrated parameters have been determined for all the southern triplets.

4. CONCLUSIONS

We have presented a list of isolated triplets of galaxies located at declinations $-90°…-3°$. We identified triplet members using the POSS-I and ESO/SERC photographic sky surveys and catalogs [9, 10]. The list of southern triplets contains a total of 76 systems selected using the same isolation criterion as that used to create the catalog of northern triple galaxy [1]. Thus, we now have at our disposal a sample of 159 isolated triple galaxy systems distributed rather uniformly over the sky,

with equal surface densities in both the northern and southern hemispheres.

We have reported the equatorial coordinates, types of triplet configuration, angular sizes, component mutual angular separations, morphological types, apparent magnitudes, component radial velocities, etc., for the southern triplets. We present the main dynamical parameters for 33 southern triplets with measured radial velocities for all three components: velocity dispersion, mean linear harmonic ratios, total luminosity, characteristic "crossing time" of the system, and virial mass-to-luminosity ratio. On the whole, the results are similar to those obtained previously for northern triplets.

We consider measuring the missing radial velocities to be a task of prime importance. This will enable a full analysis of the physical and dynamical conditions in these interesting systems, based on substantially more extensive statistical material than employed in previous studies.

ACKNOWLEDGMENTS

APPENDIX
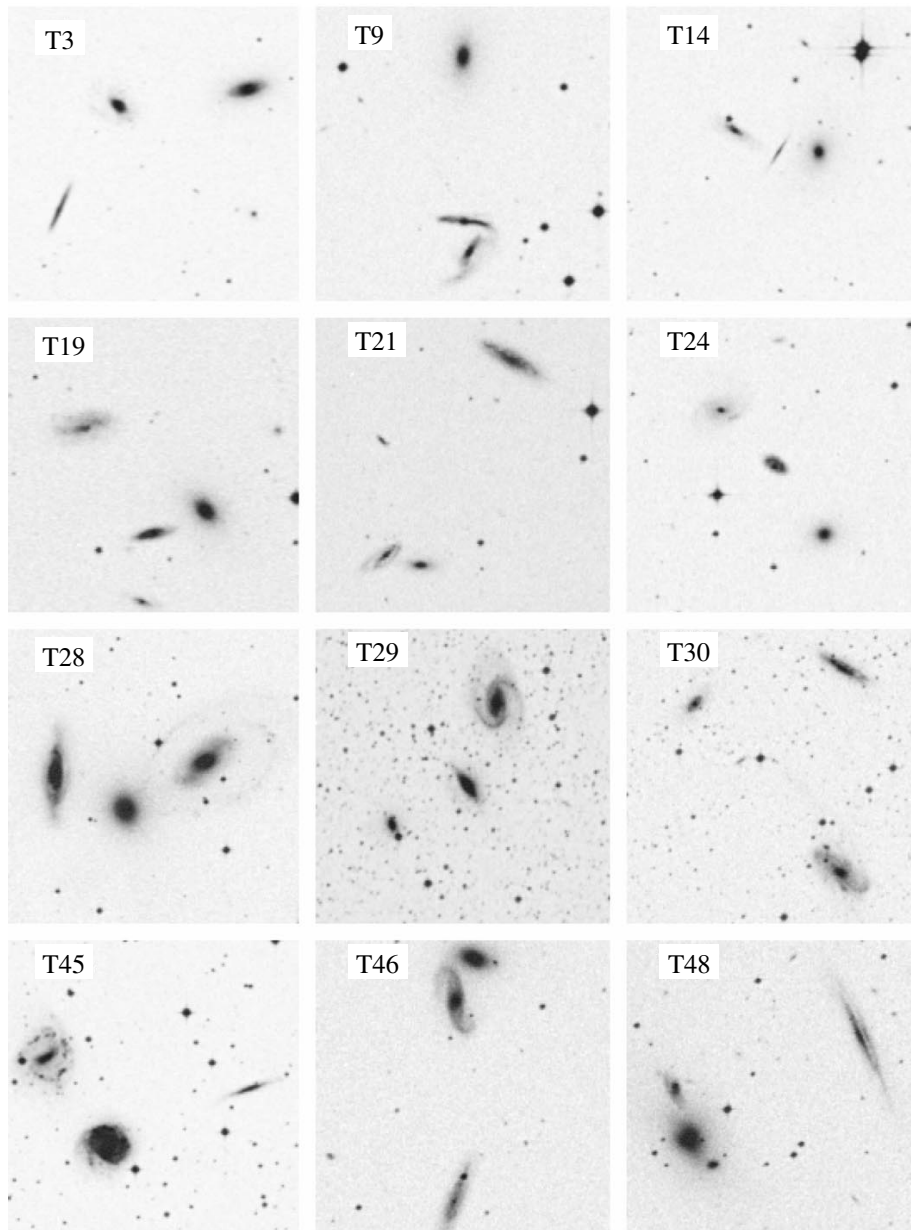
Triplet images from the DigSS atlas.
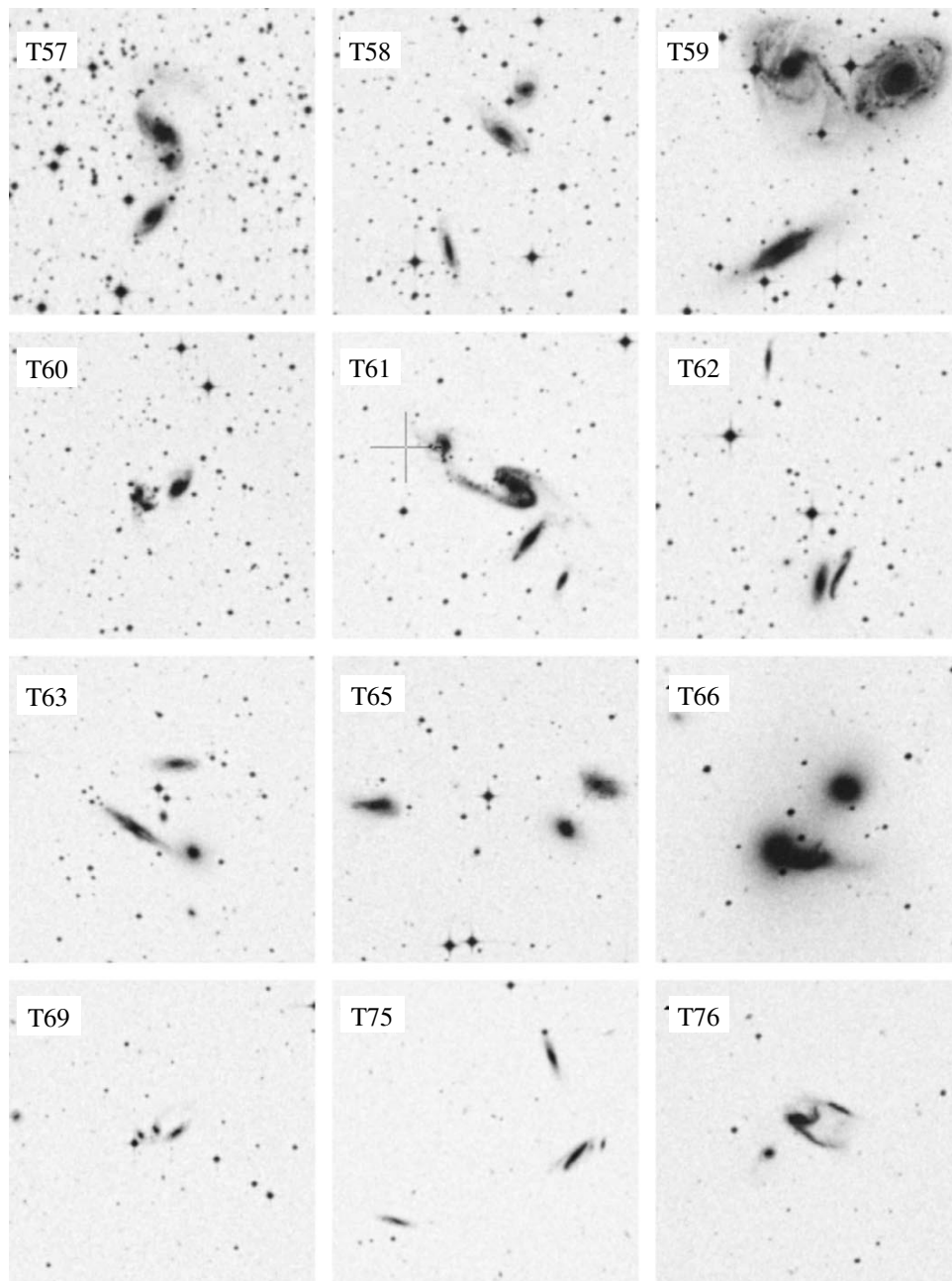
Figure. (Contd.)
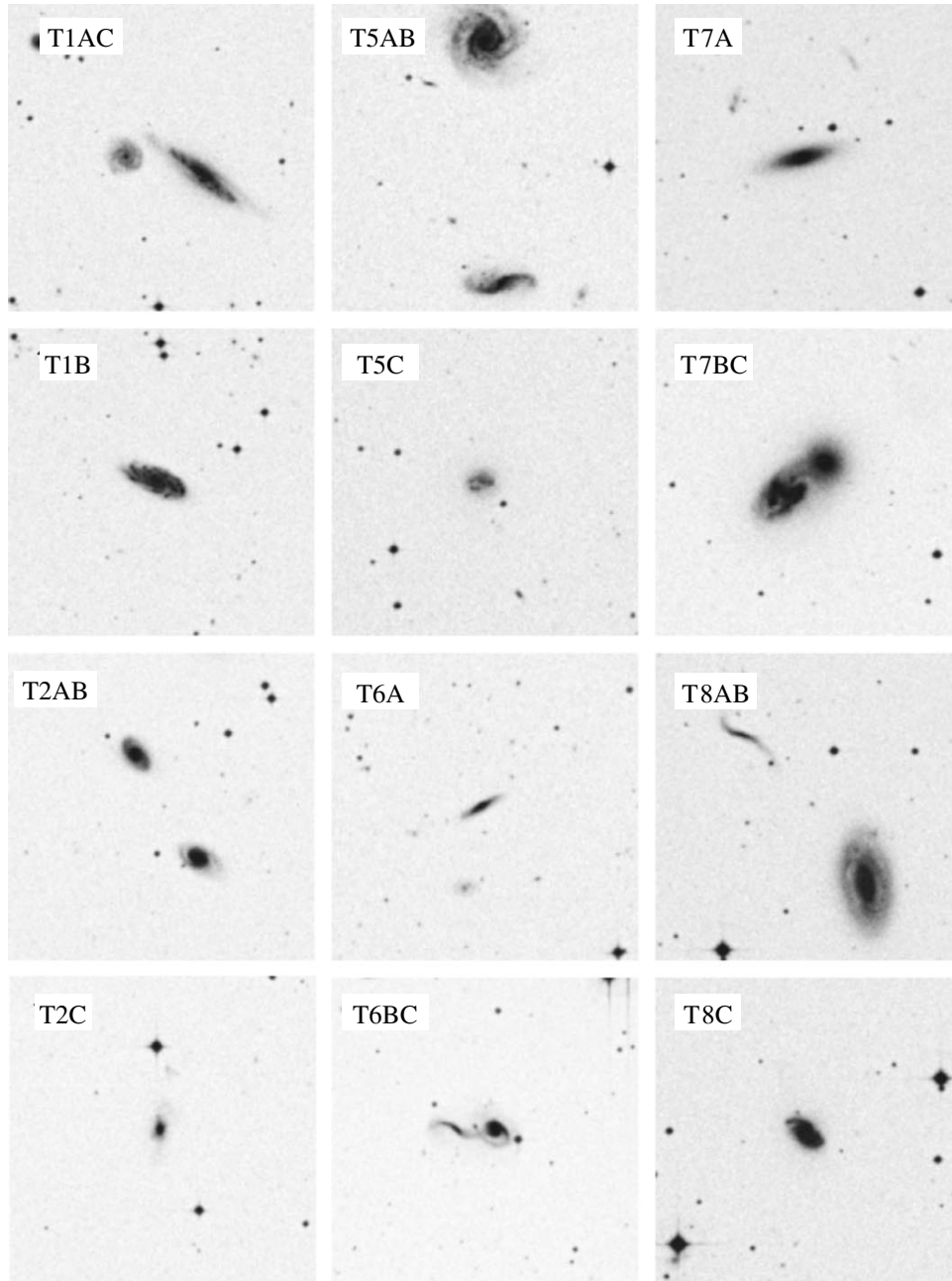
Figure. (Contd.)
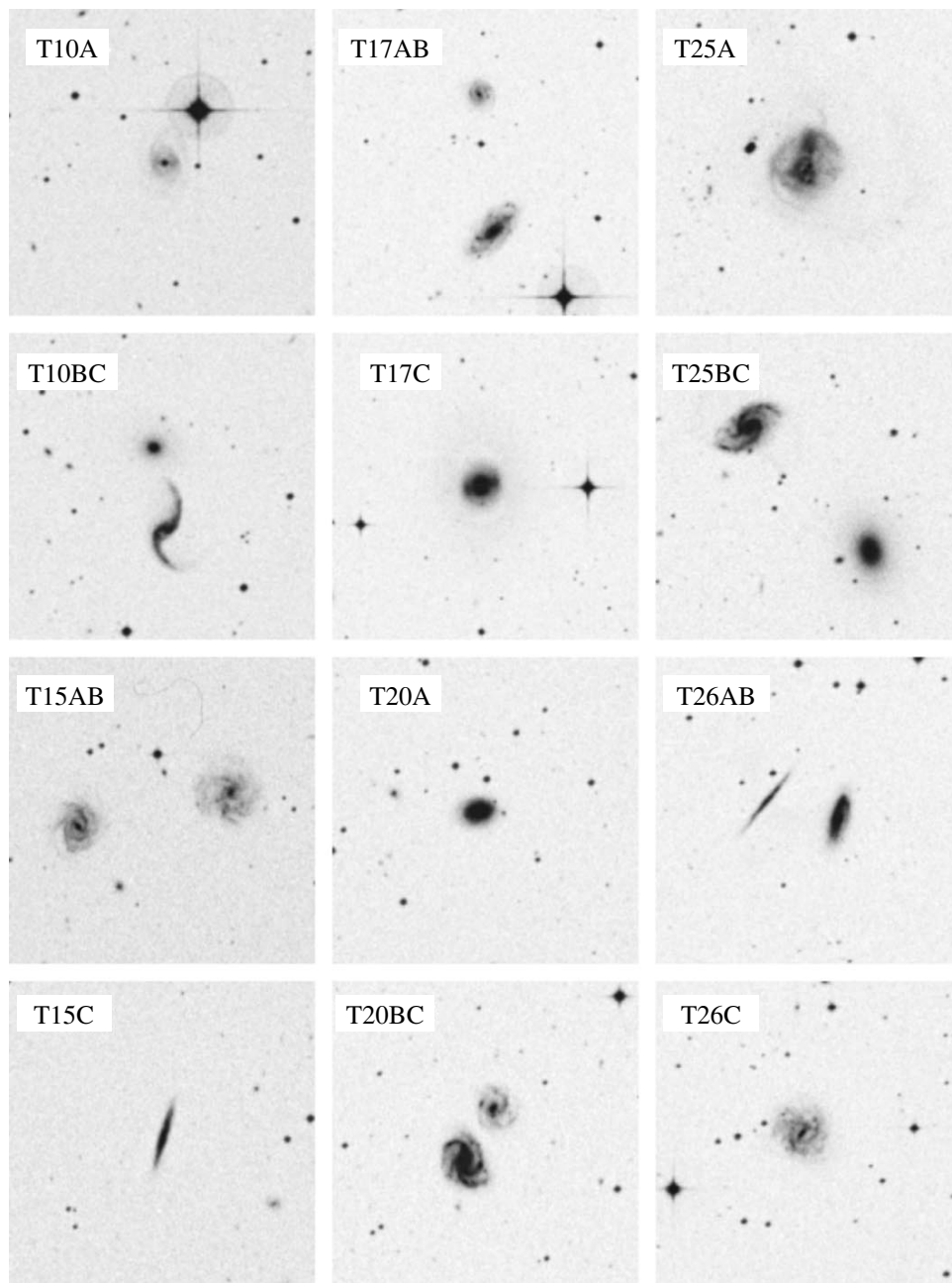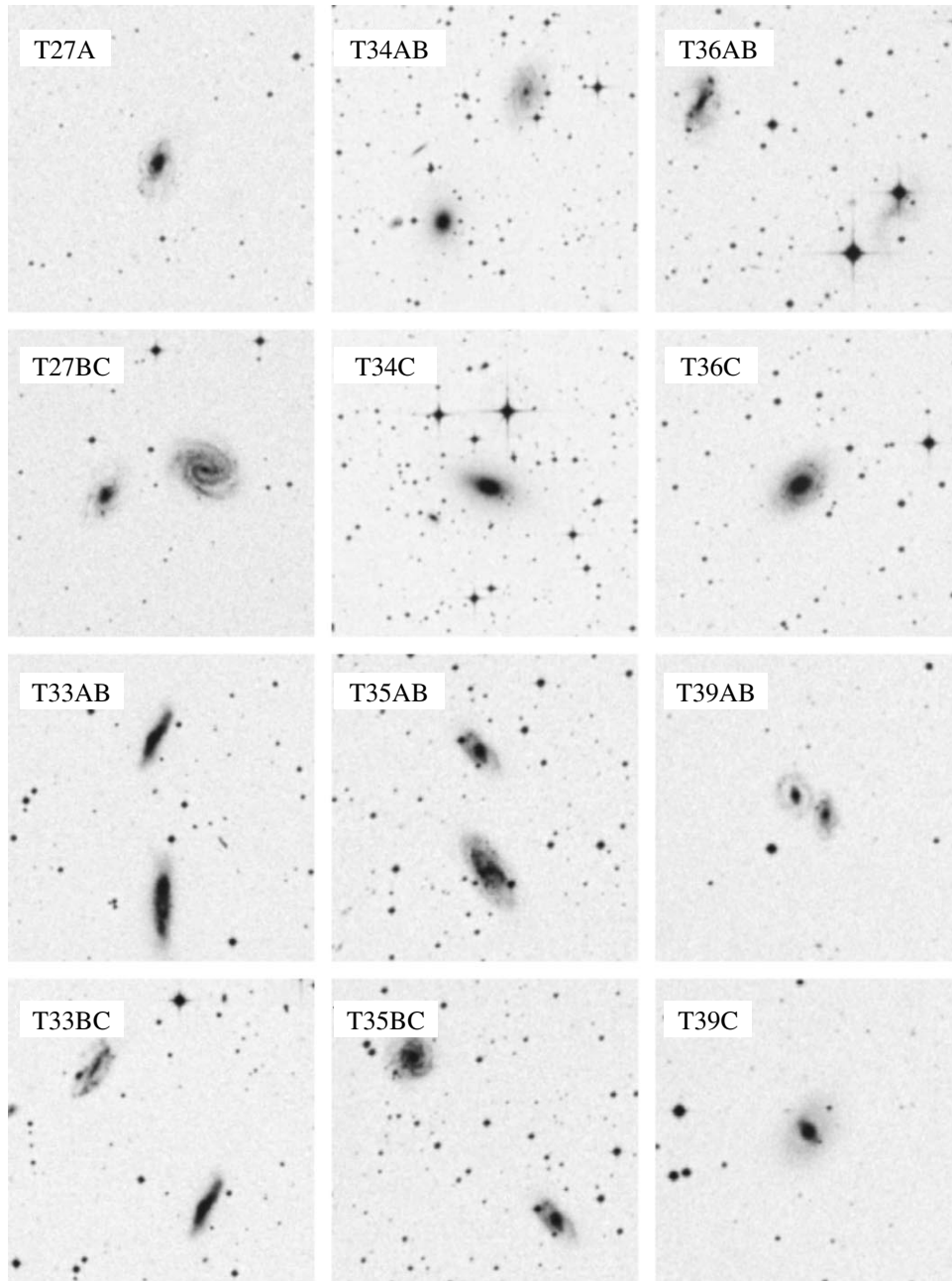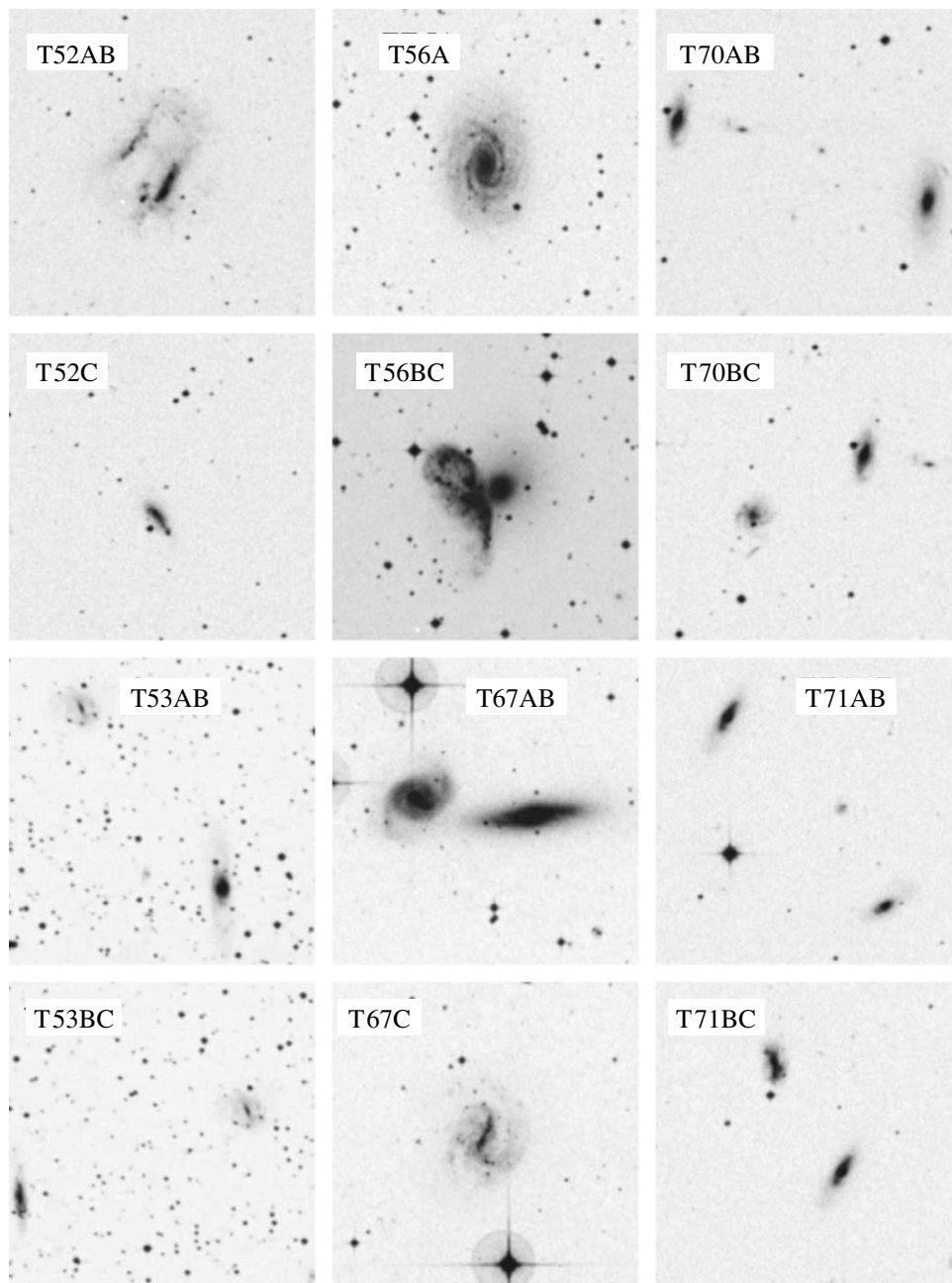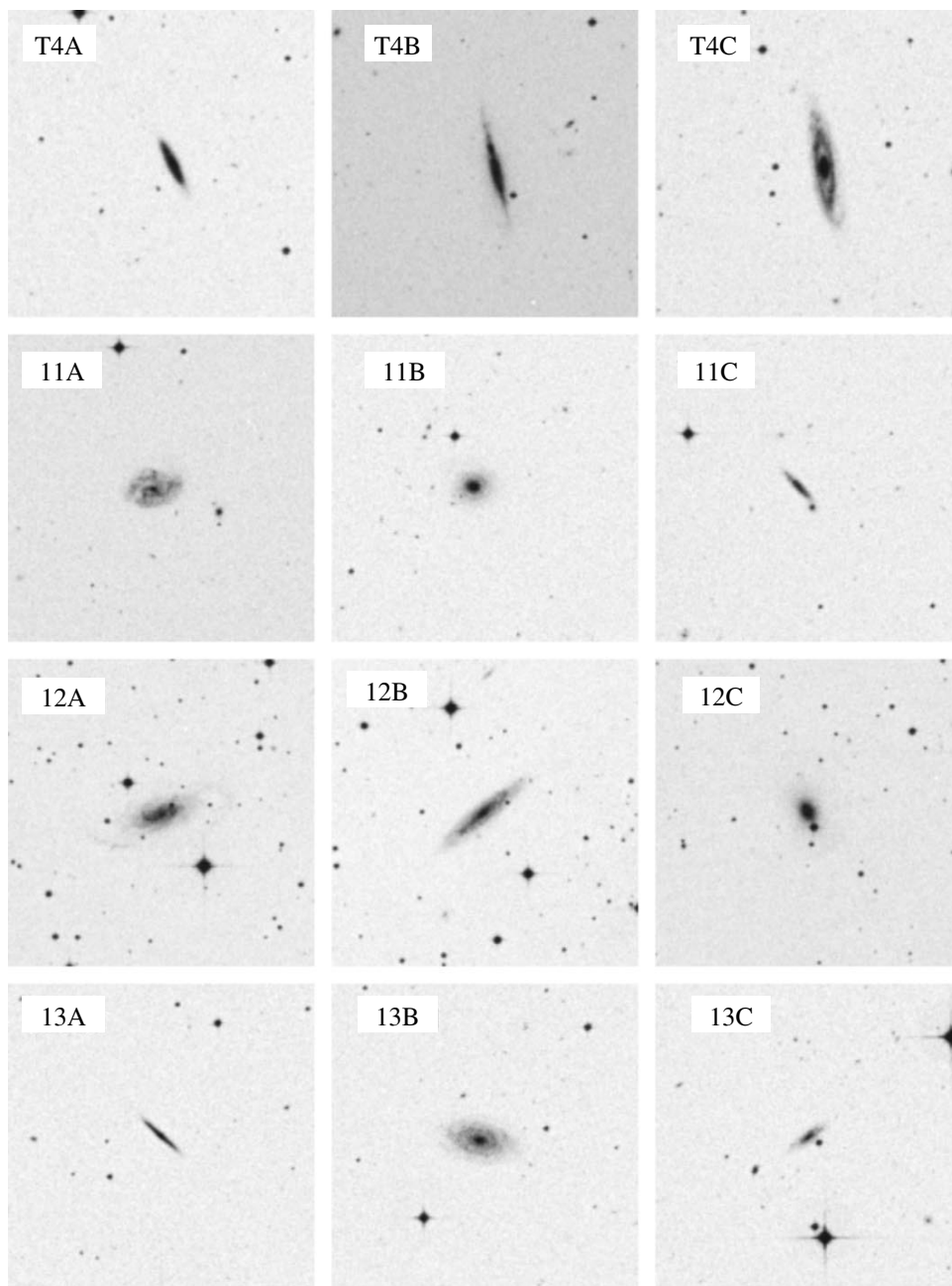
Figure. (Contd.)

Figure. (Contd.)

Figure. (Contd.)

Figure. (Contd.)

T16A

T16B

T16C

T18A

T18B

T18C

T22A

T22B

T22C

T23A

T23B

T23C
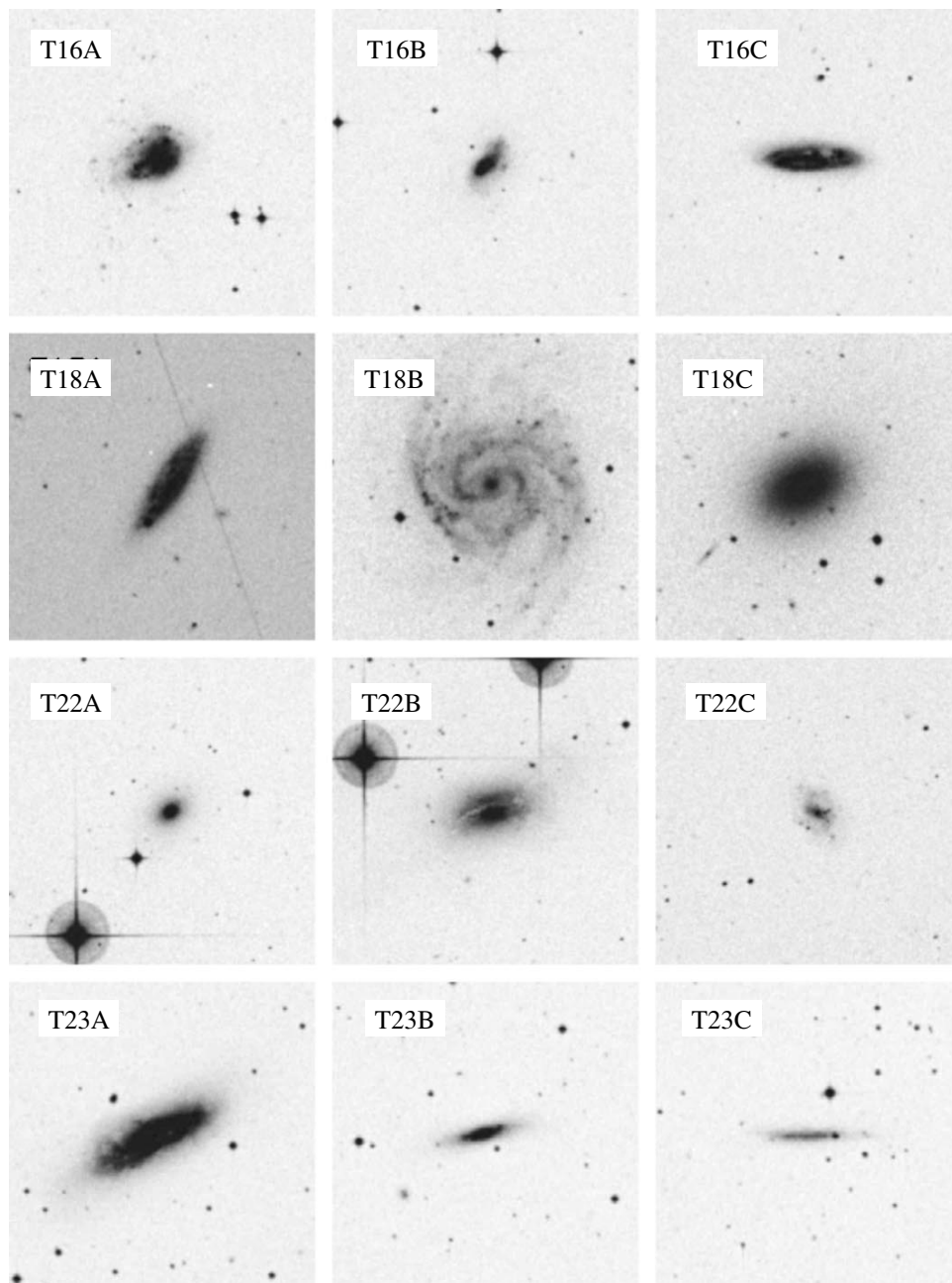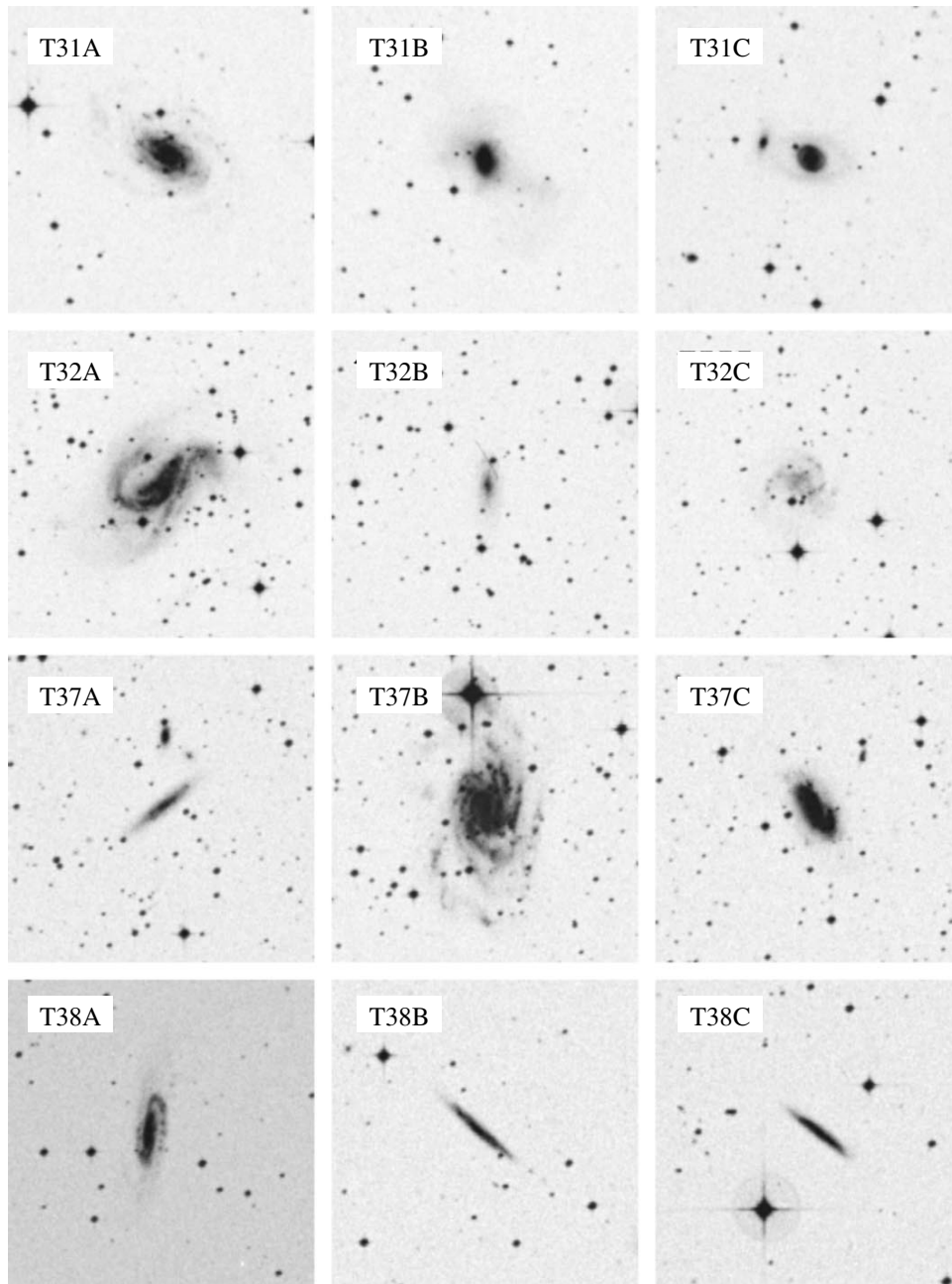
Figure. (Contd.)
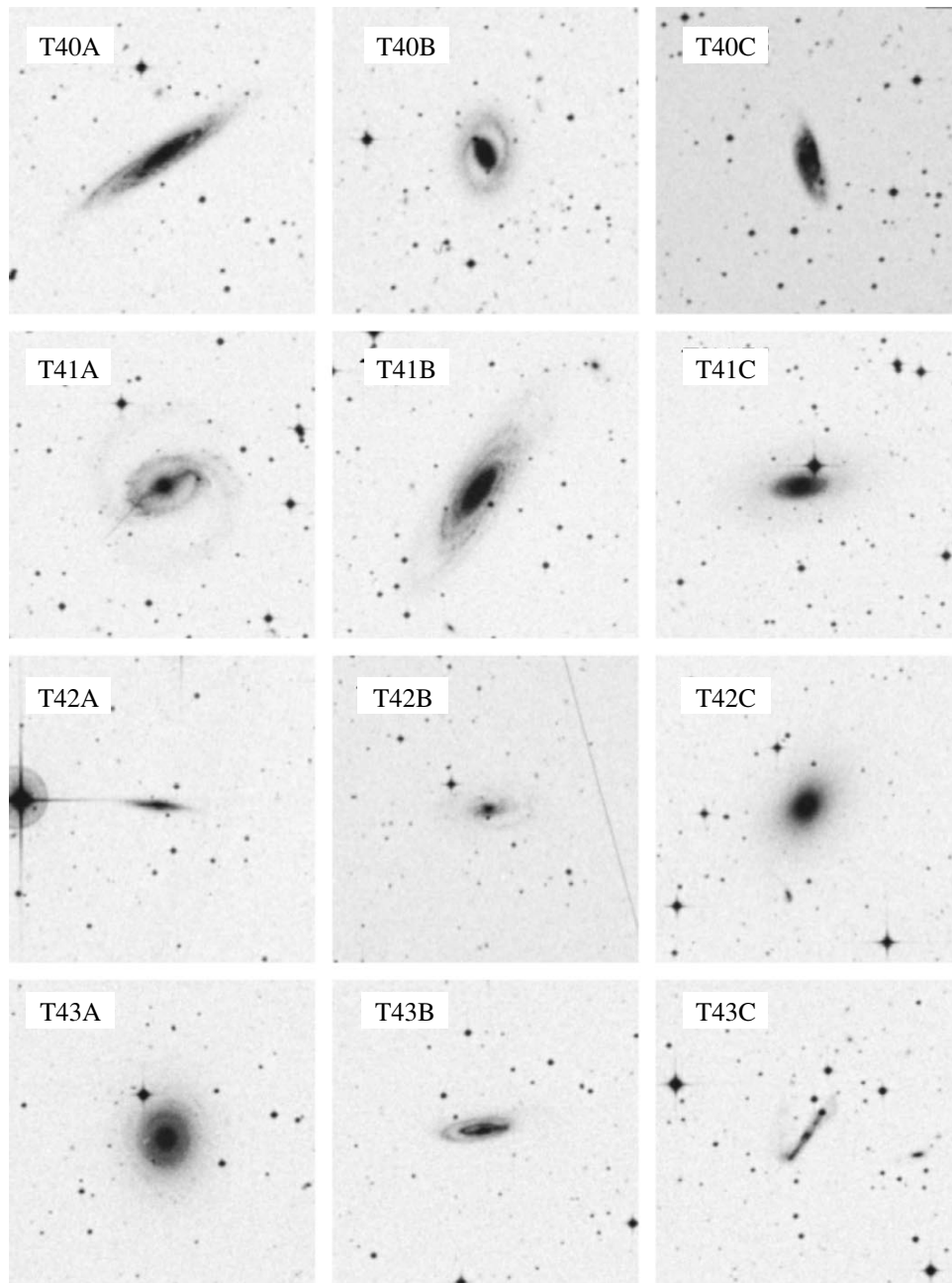
Figure. (Contd.)
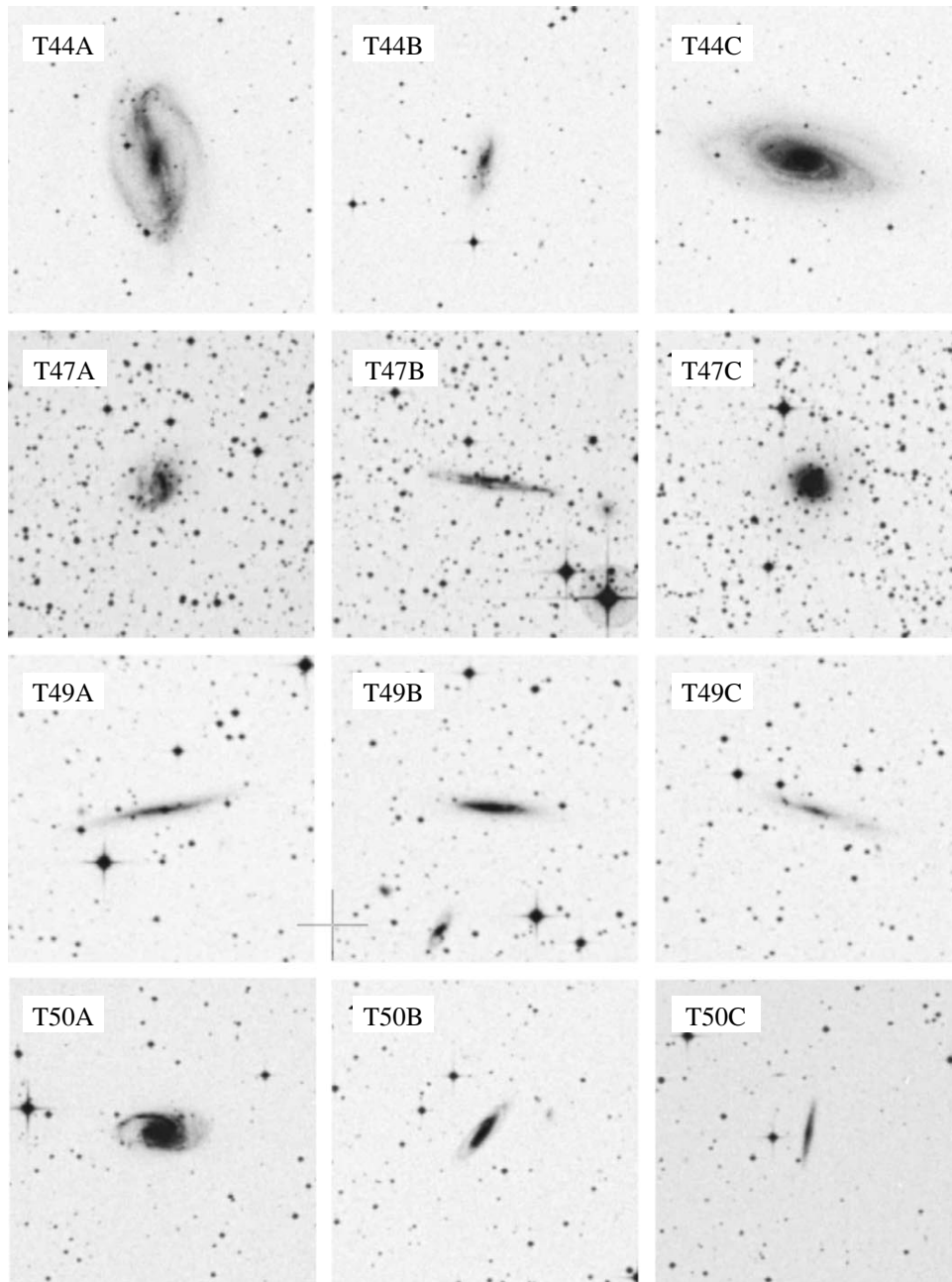
Figure. (Contd.)
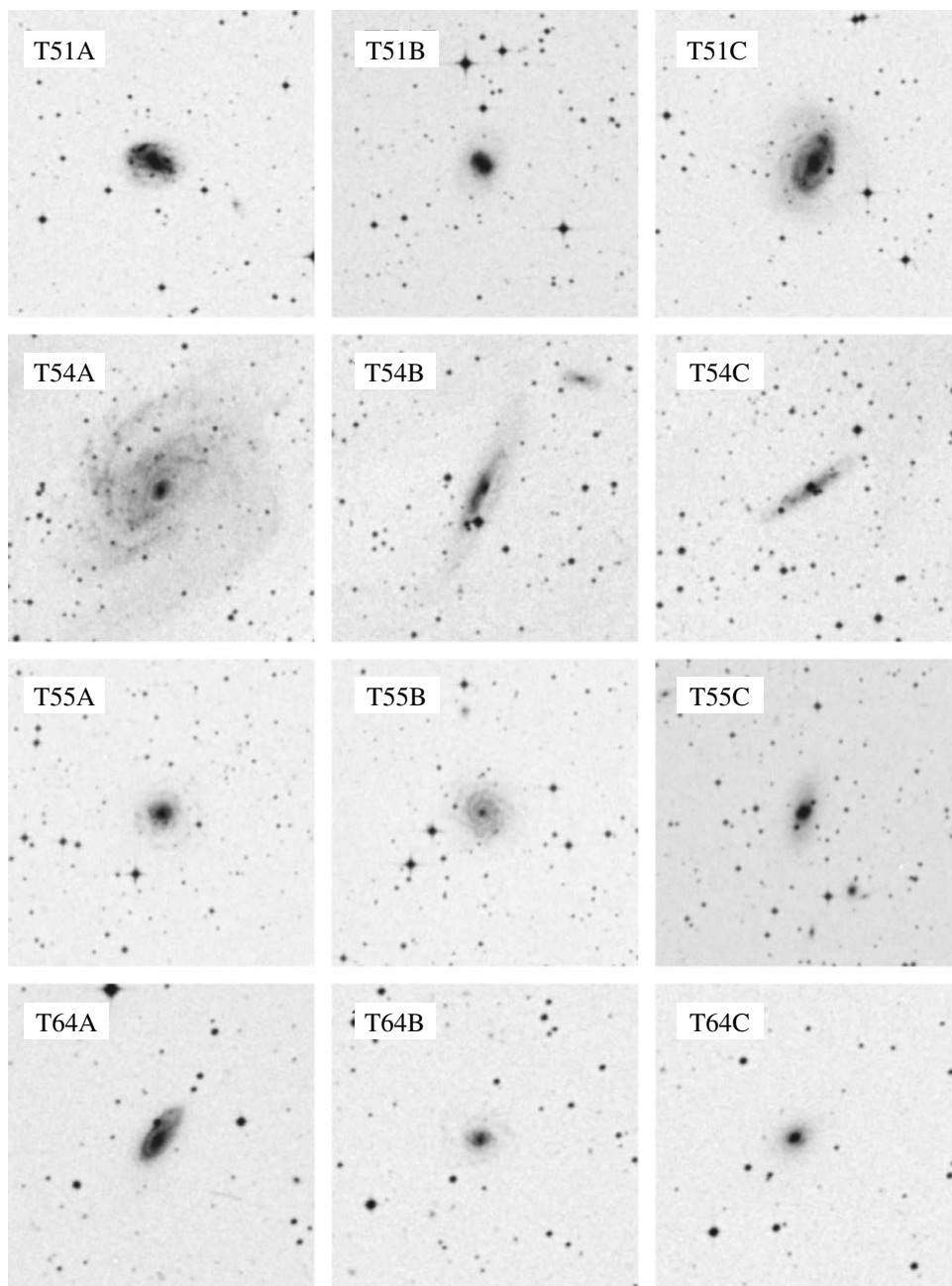
Figure. (Contd.)
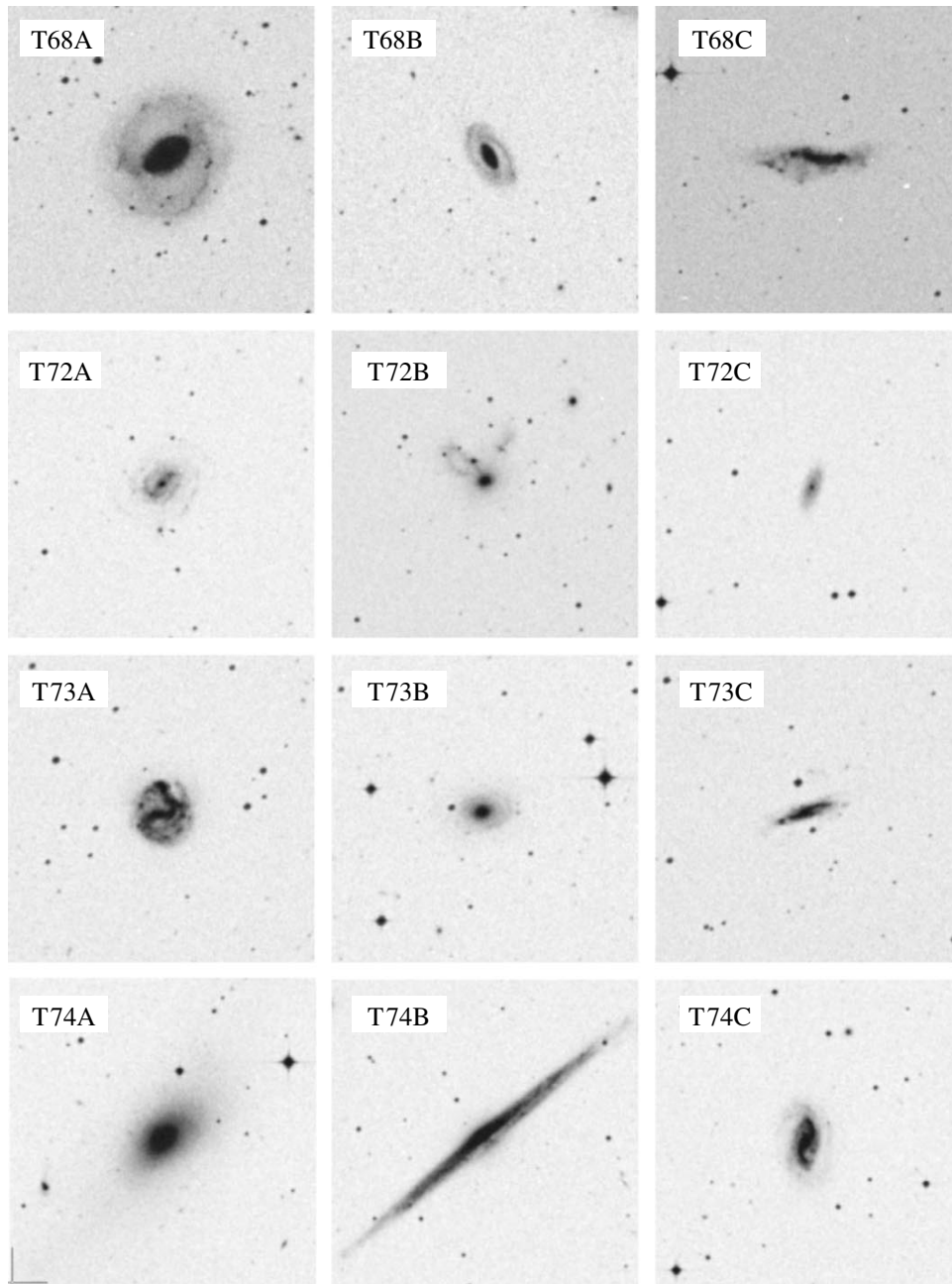
Figure. (Contd.)

Figure. (Contd.)

REFERENCES

1. V. E. Karachentseva, I. D. Karachentsev, and A. L. Shcher-banovskiĭ, Astrofiz. Issled. (Sofia) **11**, 3 (1979).

2. F. Zwicky, E. Herzog, M. Karpowicz, *et al.*, in *Catalogue of Galaxies and of Clusters of Galaxies* (California Institute of Technology, 1961–1968), Vols. I–VI.

3. I. D. Karachentsev and V. E. Karachentseva, Astrofizika **17**, 5 (1981).

4. V. E. Karachentseva and I. D. Karachentsev, Astrofizika **19**, 613 (1983).

5. V. E. Karachentseva, I. D. Karachentsev, and V. S. Lebedev, Astrofiz. Issled. (Sofia) **26**, 42 (1988).

6. I. D. Karachentsev, V. E. Karachentseva, and V. S. Lebedev, Astrofiz. Issled. (Sofia) **27**, 67 (1989).

7. I. D. Karachentsev and A. L. Shcherbanovskiĭ, Soobshch. SAO **24**, 5 (1978).

8. I. D. Karachentsev, G. G. Byrd, A. Chernin, and M. Valtonen, Fund. Cosm. Phys., 1999 (in press).

9. A. Lauberts, *The ESO/Uppsala Survey of the ESO(B) Atlas* (ESO, Munich, 1982).

10. B. A. Vorontsov-Vel'yaminov and V. P. Arkhipova, *Morphological Catalog of Galaxies* [in Russian] (Mosk. Gos. Univ., Moscow, 1963–1968), Chaps. III–IV.

11. Yu. N. Kudrya, I. D. Karachentsev, V. E. Karachentseva, and S. L. Parnovskiĭ, Pis'ma Astron. Zh. **23**, 15 (1997) [Astron. Lett. **23**, 11 (1997)].

12. I. D. Karachentsev and D. I. Makarov, Astron. J. **111**, 794 (1996).

13. D. J. Schlegel, D. P. Finkbeiner, and M. Davis, Astron. J. **500**, 525 (1998).

14. I. D. Karachentsev, Pis'ma Astron. Zh. **17**, 671 (1991) [Sov. Astron. Lett. **17**, 283 (1991)].

15. Yu. N. Kudrya, V. E. Karachentseva, I. D. Karachentsev, and S. L. Parnovskiĭ, Pis'ma Astron. Zh. **23**, 730 (1997) [Astron. Lett. **23**, 633 (1997)].

16. D. N. Limber and W. G. Mathews, Astrophys. J. **132**, 186 (1960).

Translated by A. Dambis

A Photometric Study of the Peculiar Galaxy UGC 4332

V. A. Yakovleva, V. A. Gagen-Torn, and G. M. Karataeva

Astronomical Institute, St. Petersburg State University, Bibliotechnaya pl. 2, Petrodvorets, 198904 Russia

Received August 19, 1999

Abstract—BVR_c photometry of the galaxy UGC 4332 is presented. It is shown that its inclusion in a list of candidate galaxies with polar rings is erroneous. In reality, it is a spiral galaxy with a powerful bulge and a disturbed dust disk viewed edge-on. © *2000 MAIK "Nauka/Interperiodica".*

1. INTRODUCTION

In the catalog of Candidate Galaxies with Polar Rings and Similar Objects of Whitemore *et al.* [1], the galaxy UGC 4332 is listed as a possible polar-ring galaxy. On this basis, it was included in a program of photometric observations of such galaxies carried out at the Astronomical Institute of St. Petersburg University. Here, we present and analyze the results of our *B*, *V*, R_c observations of UGC 4332.

The peculiarity of UGC 4332 (see Fig. 1, which shows a *B*-band image) lies in the presence of dark bands with complex structure crossing it from NE to SW. This hinders the precise determination of its morphological type: in the UGC, Nilsson [2] classifies it as

Irr, while Zwicky *et al.* [3] list it as a possible spiral in the CGC1G. The detection of emission lines in its nuclear region characteristic of Sy2 galaxies [4, 5] supports the idea that it is a spiral. As a member of the Cancer cluster of galaxies, UGC 4332 was included in an observational survey of this cluster in the optical and near IR [6, 7]. In connection with this, observations were also obtained in far IR [8, 9] and radio [10, 11]; detailed studies of this galaxy had not been performed earlier. The heliocentric radial velocity of UGC 4332 is 5496 km/s [6]. After correcting for the Galactic rotation (–107 km/s), this yields a distance to the galaxy of 71.9 Mpc and a scale of 0.35 kpc/arcsec (for a Hubble constant of 75 km s^{-1} Mpc^{-1}).
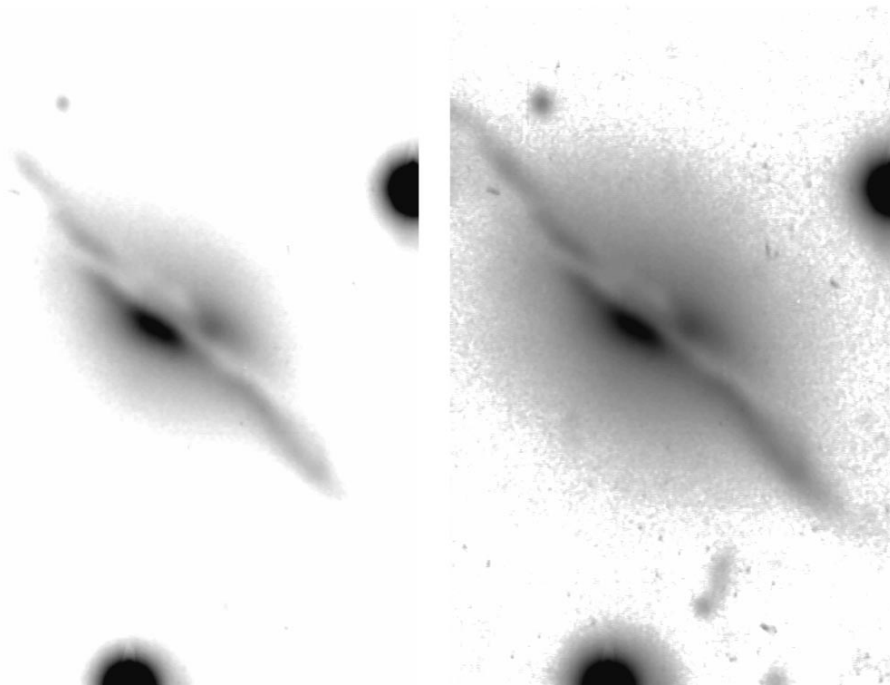
Fig. 1. *B*-band image of UGC 4332 at various brightness levels (N is up and W is to the right).
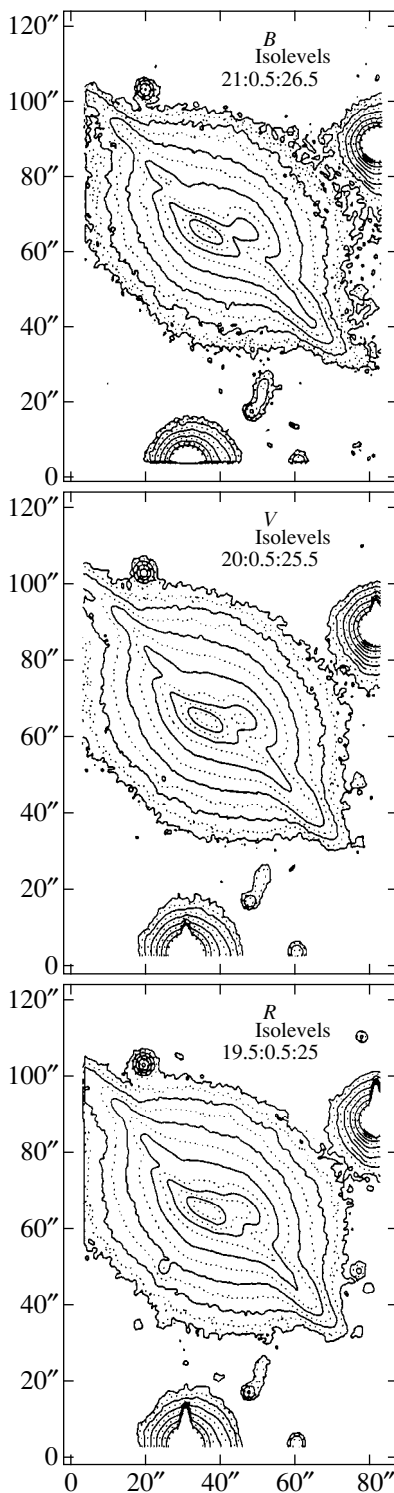
Fig. 2. Isophotes of the galaxy in the three color bands (N is up and W is to the right).

2. OBSERVATIONS AND REDUCTION

We carried out photometric observations of UGC 4332 at the prime focus of the 6-m telescope of the Special Astrophysical Observatory of the Russian Academy of Sciences. We used a K983 CCD array with 530×580 pixels (18×24 μm per pixel) with readout noise 12–20 el. [12]. The angular size of a pixel was $0.15'' \times 0.20''$, and the field of view was $1.3' \times 2.0'$. The observations were carried out in the Johnson *B* and *V* bands and the Cousins R_c band. The seeing was about $2''$.

For calibration purposes, we observed standard stars from the lists [13, 14] in the course of the night. We used the mean SAO values for the transmission coefficients to correct for the atmosphere. Table 1 presents a brief description of the observational material used; the last column gives values for the night-sky brightness in each CCD frame after correction for atmospheric absorption. The data were reduced at the Astronomical Institute of St. Petersburg University using the ESO-MIDAS package.

3. RESULTS

3.1. General Photometric Structure

Figure 1 shows that the shape of UGC 4332 (a powerful central body and relatively weak spiral arms) is very reminiscent of the well-known Sa "Sombrero" Galaxy. However, the dusty material in the "Sombrero" is distributed regularly, while the dust lane in UGC 4332 does not form a uniform layer. It is projected against the brightest region in the galaxy in the center, then divides in the northeastern part, encircling the region of the spiral arm from both sides. In the southwest, the band passes above the spiral arm, although there are also individual dusty intrusions below the arm.

Figure 2 shows isophotes of the galaxy in the three color bands. As expected if the dark band is dusty, it is strongest in the *B*-band image. We can also easily see that the brightest part of the galaxy is not its geometric center, which is obviously located to the northwest, in the region of the dark band. To determine the location of the nucleus, we approximated the outer isophotes as ellipses and found the mean of their centers, together with other parameters of each ellipse (major axis *a*, position angle, and axial ratio *b/a*). The data for the ellipse representing the 26 mag/arcsec^2 *B*-band isophote are presented in Table 2 and summarize the main characteristics of UGC 4332.

Figures 1 and 2 suggest that UGC 4332 is a spiral galaxy viewed edge-on. We can crudely estimate the inclination of the galaxy $i = 85°$ and the optical depth of the dusty layer $\tau_V \sim 0.5$ perpendicular to the plane of the disk by comparing the isophote patterns and the observed brightness distribution along the minor axis (see below) with model calculations for galaxies with dusty stellar disks and powerful bulges [15]. According to the computations of Byun *et al.* [15], the internal absorption in the *B* band ($A_{B,\,int}$) in a galaxy with $\tau_V = 0.5$ and $i = 85°$ is 0.3^m–0.5^m, depending on whether or not the light scattered by dust is taken into account. As we will see below, this is close to the internal absorption implied by the observations.
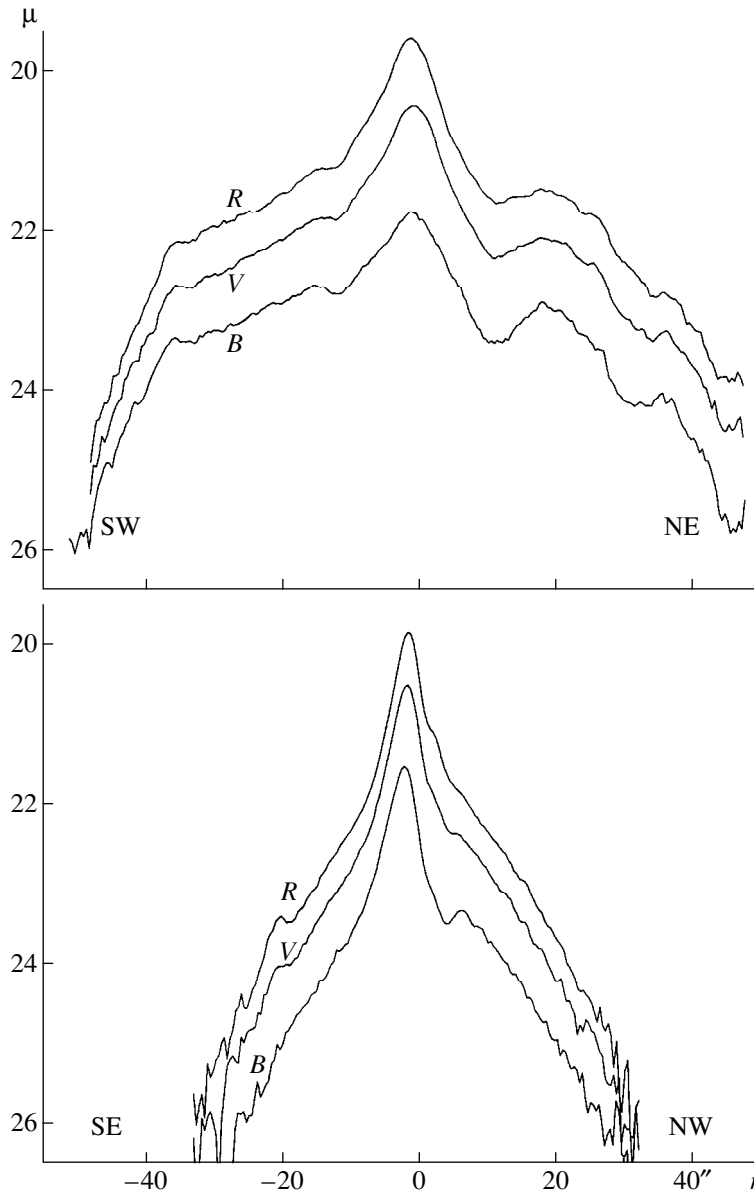
Fig. 3. Photometric cuts along the major (upper) and minor (lower) axes.

3.2. Integrated Characteristics

We used multiaperture photometry to determine the integrated asymptotic apparent magnitudes of the galaxy. The brightness curve of growth is in agreement with the standard aperture dependences for Sa galaxies ($T = 1$) for the RC3 [16]. The resulting values $B_t = 14.93$, $V_t = 13.95$, and $R_{c,t} = 13.32$ are in good agreement with those presented in the RC3 (taking into account that $R_c = R_j + 0.25$): $B_t = 14.82 \pm 0.1$, $V_t = 13.86 \pm 0.1$, and $R_{j,t} = 13.03$.

The Galactic interstellar absorption for UGC 4332 indicated by the RC3 is $E_{B-V} = 0.05$. Table 2 presents the integrated magnitudes and colors of UGC 4332 corrected for interstellar absorption. The resulting color is

redder than the mean colors for Sa galaxies (apparently due to internal absorption in the galaxy). For example, the $B-V$ color excess is $E_{B-V} = 0.13$; for a normal ratio of total to selective absorption $R_B = 3.1$, this yields $A_{B, \text{int, obs}} \approx 0.5$ (in agreement with the estimate obtained in the previous section). Although R_B may be different

Table 1. Observational material

Date	Band	Exposure, s	z	μ_{sky}
Mar. 10, 1994	R_c	300	23°	20.6
	V	600	23	21.3
	B	900	22.5	22.0
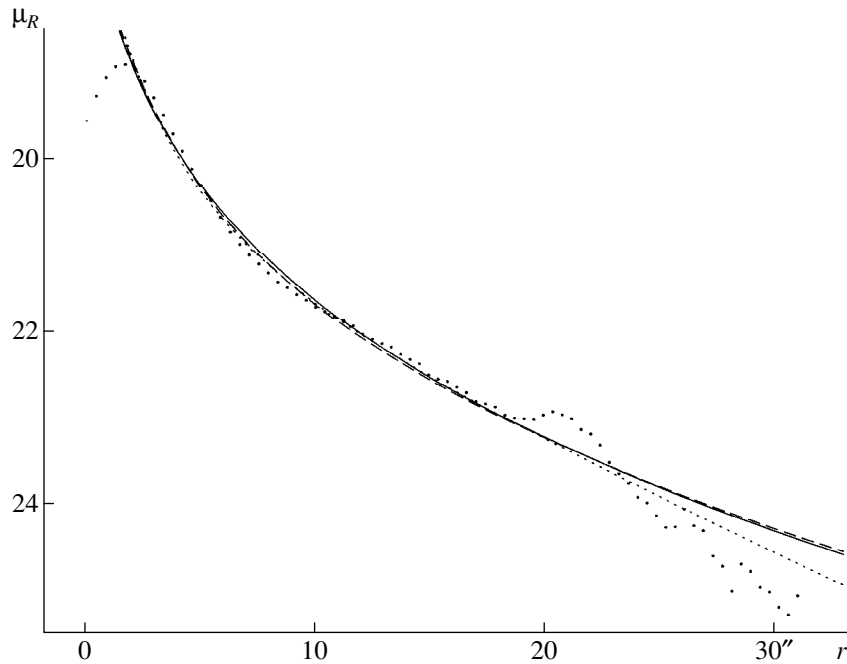
Fig. 4. Three representations of the SE part of the *R*-band galactic profile along the minor axis.

for different models for the galaxy and different dust particles, this difference is unlikely to cause a change exceeding 0.2. Taking internal absorption into account, we obtain for the absolute magnitude, $M_{0,B} = -20.1 \pm 0.3$; i.e., the galaxy is giant.

Table 2. Main characteristics of UGC 4332

Distance [6]	71.9 Mpc (0.35 kpc, 1″)
E_{B-V}	0.05
B_t	14.71
V_t	13.78
$R_{c,t}$	13.18
$(B-V)_t$	0.93
$(V-R_c)_t$	0.60
Ellipse corresponding to the $\mu_B = 26.0$ isophote	
a	36″
b/a	0.6
Position angle	54°
$A_{B,\text{int. obs}}$	0.5
$M_{0,B}$	−20.1
Diagnostic results	
i	85°
τ_V	≈0.5
$A_{B,\text{int}}$	0.3–0.5

3.3. Brightness and Color Distribution

Figure 3 presents photometric cuts of the galaxy along the three main axes in three spectral bands. Due to the nonuniformity of the absorption, only the SE part of the cut along the minor axis has a regular shape, though, here as well, the formal decomposition of the profile into a bulge and disk is not well determined. For example, in the *R* band, where the influence of dust is less appreciable, the profile (Fig. 4) can be equally well represented as an extended bulge with $\mu_e = 21.72$, $r_e = 10.2″$ (3.6 kpc) plus a bright, small disk with $\mu_0 = 19.0$, $h = 1.3″$ (0.5 kpc) (dashed curve), or as an extended, low-brightness disk with $\mu_0 = 21.1$, $h = 8.5″$ (3.0 kpc) plus a small, but very bright bulge with $\mu_e = 19.7$, $r_e = 3.2″$ (1.1 kpc) (dotted curve). In both cases, the parameters of the small, bright formation seem to be implausible. Since UGC 4332 could be an Sa galaxy, we prefer the first option. If we try to describe the profile using only a bulge with $\mu_e = 21.4$ and $r_e = 9″$ (3.2 kpc), the agreement with the observed profile does not appreciably worsen over most of the profile (solid curve in Fig. 4). For an axial ratio $b/a = 0.6$, the equivalent effective radius R_e is equal to 4.1 kpc.

In the plane of effective parameters for galactic bulges in the R_c band (recalculation to R_c using the standard relations of Kent [17] was carried out by Reshetnikov *et al.* [18]), UGC 4332 is located close to the dependence for elliptical and S0 galaxies. It deviates from the dependence for spiral galaxies, being roughly 1.0^m brighter (at fixed R_e), which is not surprising for such a powerful bulge.
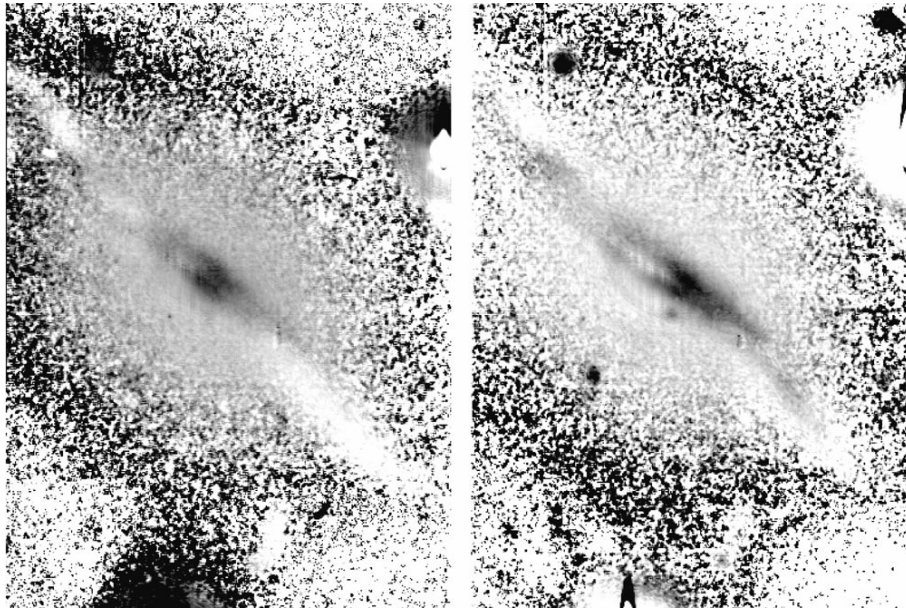
Fig. 5. Distribution of *B–V* (left) and *V–R* (right) in the galaxy (N is up and W is to the right).

By comparing the NW part of the profile along the minor axis and the SE part, which is undistorted by the influence of dust, we can estimate the distribution of the absorption in the photometric band (assuming that the profile is symmetric). The results are presented in Table 3, where the columns give (1) the distance to the center of the galaxy; (2)–(4) the absorption in the *B*, *V*, and *R* bands; and (5), (6) ratios of the absorption in different bands. The mean absorption ratios are $\overline{A_B/A_V} = 1.29$ and $\overline{A_R/A_V} = 0.78$, which are close to the values for the reddening curve in our Galaxy (1.32 and 0.84), suggesting that the dust components in the two galaxies are similar.

Figure 5 shows the distribution of *B–V* (left) and *V–R* (right) over the galaxy, emphasizing details of the structure of the dust lane. Figure 6 presents color cuts in *B–V* along the main axes, and a two-color diagram is shown in Fig. 7. Inspection of these figures and comparison with the brightness distribution shows that, as expected, the largest values for the color indices are observed in the region of the dust lane. Most of the points on the two-color diagram are grouped near *B–V* = 1.0, *V–R* = 0.6, which are characteristic for galactic bulges; points corresponding to spiral branches are located above, and a tail connected to the region of the dark band extends to the right and downward. The direction of this tail coincides to that of the reddening line. We can see that the color excess in the band reaches $E_{B-V} \simeq 0.5$, which for the normal value $R_V = 3.1$ gives an absorption in the band that is in agreement with the data in Table 3. To estimate the contribution of the spirals to the total observed emission from the SW part of the observed major-axis profile, we subtracted the emission due to the bulge. We estimated the bulge contribution from the SE part of the

profile along the minor axis and the *b/a* from Table 2. In all three spectral bands, the surface brightnesses from 17″ to 35″ along the arm were roughly constant and equal to $\mu_B = 23.72$, $\mu_V = 23.22$, and $\mu_R = 22.66$. This yields mean color indices *B–V* = 0.50 and *V–R* = 0.56, characteristic of spiral arms.

4. DISCUSSION AND CONCLUSION

Although UGC 4332 was included in the catalog of Whitemore *et al.* [1] as a candidate galaxy with polar rings (object C26), other observational data do not confirm this identification. If we consider UGC 4332 as a polar-ring galaxy, the bluest parts of the galaxy and the dust should be associated with the ring, and we should take the elliptical main body to be a disk viewed nearly face-on. Since there is no bifurcation of the dust structure in the central region (Fig. 1; see also the image of the central part of the galaxy obtained using the HST [19]), the ring should be observed edge-on. In this case, the width of the ring at the periphery of the galaxy should be larger than in the center. However, there is an offset of the dark material relative to blue regions at the periphery, making it necessary to invoke the presence of two spatially separated polar rings (dusty and stellar). The development of this type of configuration does not seem likely.

On the other hand, if we take UGC 4332 to be a spiral galaxy, the offset of the dust disk relative to the stellar disk could quite plausibly be the consequence of interaction (UGC 4332 is a member of a cluster of galaxies). The rotation rate of the gaseous component reached at the galactic periphery, 250 km/s [20], is not usual for spiral galaxies. Although the brightness pro-
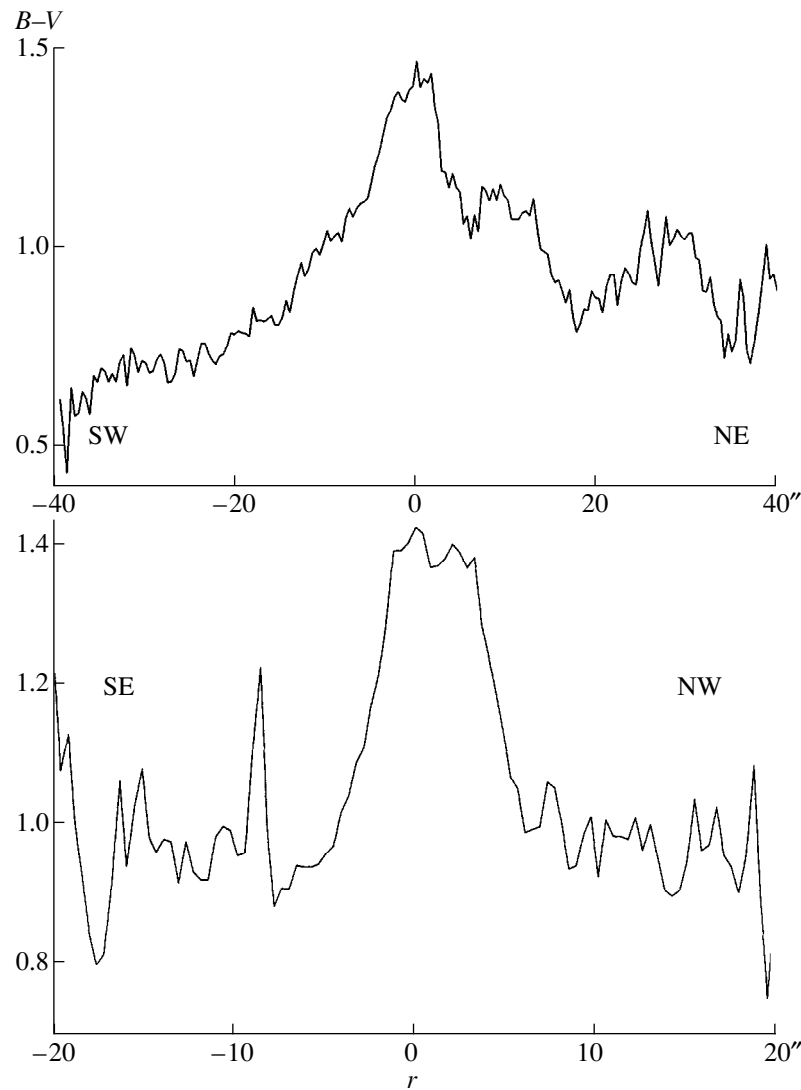
Fig. 6. Color cuts along the main axes: major (upper panel) and minor (lower panel).

file along the minor axis (Fig. 4) is consistent with the elliptical formation being a disk viewed nearly face-on, its color characteristics argue against this interpretation. Here, the deciding argument would be provided

Table 3. Distribution of absorption in the dust lane

r	A_B	A_V	A_R	A_B/A_V	A_R/A_V
1	2	3	4	5	6
3″	1.95	1.68	1.39	1.16	0.82
4″	1.73	1.45	1.09	1.19	0.75
5″	1.20	0.96	0.81	1.25	0.84
6″	0.76	0.60	0.43	1.27	0.72
7″	0.50	0.35	0.26	1.43	0.74
8″	0.30	0.21	0.16	1.43	0.76

by an absorption-line rotation curve; however, unfortunately, such data are currently lacking.

The infrared and radio data [11] in no way contradict the possibility that UGC 4332 is a spiral galaxy viewed edge-on. Indeed, the mass of neutral hydrogen $(5.5 \times 10^9 \mathcal{M}_\odot)$ and IR luminosity $(9.7 \times 10^9 \mathcal{L}_\odot)$ are not unusual for spiral galaxies. At the same time, all kinematically confirmed galaxies with polar rings have substantially lower IR luminosities. The contrast between UGC 4332 and kinematically confirmed polar-ring galaxies can clearly be seen in Figs. 3–6 of [11].

The information presented above leads us to conclude that UGC 4332 is not a polar-ring galaxy but instead a spiral galaxy with a powerful bulge viewed edge-on. The dark band that intersects it is due to dust whose properties are close to those of the dust in our Galaxy. In this sense, UGC 4332 is quite reminiscent of
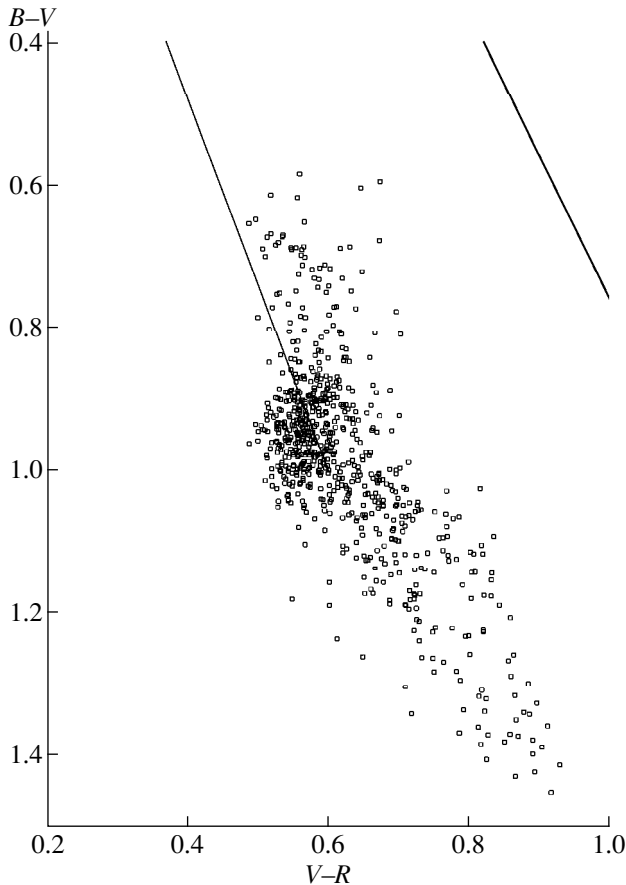
Fig. 7. Two-color diagram. The line in the upper right corner shows the direction of the reddening line, and the thin line corresponds to the mean dependence for normal galaxies.

NGC 4594 (the "Sombrero" Galaxy), for which similar results were obtained in [21].

REFERENCES

1. B. C. Whitmore, R. A. Lucas, D. B. McElroy, *et al.*, Astron. J. **100**, 1489 (1990).
2. P. Nilsson, *Uppsala General Catalogue of Galaxies*, Upsala Obs. Ann. **6**, 1 (1973).
3. F. Zwicky, E. Herzog, M. Karpowicz, and C. T. Kowal, *Catalogue of Galaxies and Clusters of Galaxies: I–VI* (Calif. Inst. Tech., Pasadena, 1961–1968).
4. V. A. Lipovetskiĭ, S. I. Neizvestnyĭ, and O. M. Neizvestnaya, Soobshch. SAO, No. 55, 5 (1987).
5. A. Hewitt and G. Burbidge, Astrophys. J., Suppl. Ser. **75**, 297 (1991).
6. G. Gavazzi, B. Garilli, L. Carrasco, *et al.*, Astron. Astrophys., Suppl. Ser. **104**, 271 (1994).
7. G. Gavazzi, G. Trinchieri, and A. Boselli, Astron. Astrophys., Suppl. Ser. **86**, 109 (1990).
8. *IRAS Catalogs and Atlases, Point Source Catalog* (US Government Printing Office, Washington, D. C., 1989).
9. H. D. Bicay and R. Giovanelli, Astrophys. J. **321**, 645 (1987).
10. E. E. Salpeter and J. M. Dickey, Astrophys. J. **317**, 102 (1987).
11. O. R. Richter, P. D. Sackett, and L. S. Sparke, Astron. J. **107**, 99 (1994).
12. *Report of SAO 1993–1994*, Ed. by S. N. Fabrika.
13. A. U. Landolt, Astron. J. **88**, 439 (1983).
14. R. S. Smith, B. T. Jannuzi, and R. Elston, Astrophys. J., Suppl. Ser. **77**, 67 (1991).
15. Y. I. Byun, K. C. Freeman, and N. D. Kylafis, Astrophys. J. **432**, 114 (1994).
16. G. de Vaucouleurs, A. de Vaucouleurs, H. G. Corwin, *et al.*, *Third Reference Catalogue of Bright Galaxies* (Springer, New York, 1991).
17. S. M. Kent, Astrophys. J., Suppl. Ser. **59**, 115 (1985).
18. V. P. Reshetnikov, V. A. Hagen-Thorn, and V. A. Yakovleva, Astron. Astrophys. **278**, 351 (1993).
19. M. A. Malkan, V. Gorjian, and R. Tam, Astrophys. J., Suppl. Ser. **117**, 25 (1998).
20. V. P. Reshetnikov and F. Combes, Astron. Astrophys. **291**, 57 (1994).
21. J. H. Knapen, R. Hes, J. E. Beckman, and R. F. Peletier, Astron. Astrophys. **241**, 42 (1991).

Translated by D. Gabuzda

Non-LTE Effects in Mg I Lines for Various Types of Stars

N. N. Shimanskaya, L. I. Mashonkina, and N. A. Sakhibullin

Kazan State University, ul. Lenina 416, Kazan, 420111 Russia
Received August 18, 1999

Abstract—We have performed a detailed statistical-equilibrium analysis based on a 49-level model of the magnesium atom for the atmospheres of stars of various spectral types: T_{eff} = 4500–12000 K, $\log g$ = 0.0–4.5, and [M/H] = 0 to –3. In the atmospheres of stars with T_{eff} > 5500 K, deviations from LTE for Mg I are due to photoionization by ultraviolet radiation from the 3p level; i.e., neutral magnesium is in a state of "superionization." When T_{eff} < 5500 K, the populations of the Mg I levels differ from their LTE values due to radiative processes in bound–bound transitions. We analyzed Mg I lines in the solar spectrum in order to empirically refine certain atomic parameters (the van der Waals broadening constant C_6 and cross sections for photoionization and collisional interactions with hydrogen atoms) and the magnesium abundance in the solar atmosphere. We studied non-LTE effects for five Mg I lines for a wide range of stellar parameters. In the case of dwarfs and subdwarfs, the magnitude of non-LTE corrections to magnesium abundances does not exceed 0.1 dex for the $\lambda\lambda$ 4571, 4703, 5528, and 5711 Å lines but can be as large as ±0.2 dex for the $\lambda\lambda$ 3829–3838, 5172, and 5183 Å lines. The non-LTE corrections for giants and supergiants do not exceed 0.15 dex for the $\lambda\lambda$ 4571 and 5711 Å lines but can reach ±0.20 dex and even more for the $\lambda\lambda$ 4703, 5528, 3829–3838, 5172, and 5183 Å lines. © *2000 MAIK "Nauka/Interperiodica".*

1. INTRODUCTION

Estimates of the abundances of light elements in the atmospheres of stars belonging to different Galactic populations increase our understanding of the thermonuclear synthesis reactions enriching the interstellar medium with light elements. In this way, they provide a unique tool for studying the Galaxy's chemical evolution.

Magnesium is an important element in the chain of nuclear transformations. Many observations of neutral magnesium lines for stars of various spectral types can be found in the literature. This is due to the presence of numerous Mg I lines in the visible and infrared. Extensive calculations of magnesium abundances in stellar atmospheres usually assume local thermodynamic equilibrium (LTE; cf., for example, [1–8]). However, computations by several authors [9–20] have shown that populations of Mg I levels in the atmospheres of dwarfs and giants of various spectral types do not correspond to the Boltzmann–Saha formula.

The first non-LTE analysis of Mg I spectral lines for the solar atmosphere was presented in [13]. Later, a series of papers [14–18] investigated transitions between high levels giving rise to Mg I emission lines at $\lambda \sim 12$ µm. Only two studies [19, 20] considered deviations from LTE for the Mg I lines normally used to determine stellar magnesium abundances. Two Mg I lines, $\lambda\lambda$ 4571 and 5173 Å, were analyzed in [19]. The most comprehensive study dedicated to a non-LTE analysis of solar Mg I lines in the visible and infrared (18 lines, including emission at $\lambda \sim 12$ µm) was published by Zhao *et al.* [20]. Using their own model atmo-

sphere, they determined empirical corrections to several important line parameters.

In future studies, we plan to determine the Mg abundances for specific stars taking into account non-LTE effects using the LTE models of Kurucz [21]. Since the specific values of atomic parameters depend on the solar model atmosphere used, our adopted model of the Mg I atom and set of atomic data should be tested using a solar model atmosphere from Kurucz's model grid.

Thus, our present study is aimed at a detailed analysis of the statistical equilibrium of the magnesium atom in the atmospheres of stars of various types and empirical refinement of atomic parameters based on an analysis of Mg I lines in the solar spectrum. Section 2 describes the atomic model and computation technique, and Section 3 analyzes non-LTE effects for the magnesium atom for stars of various spectral types. Section 4 contains our analysis of Mg I lines in the solar atmosphere. Relations between the theoretical non-LTE corrections to the magnesium abundances and the stellar parameters for five Mg I lines ($\lambda\lambda$ 3838, 4571, 4703, 5183, and 5711 Å) are considered in Section 5.

2. THE ATOMIC MODEL AND COMPUTATION TECHNIQUE

We adopt the model for the magnesium atom and computation technique described in detail in [9]. Here, we note only important and new aspects. Our atomic model consists of 49 bound energy states of Mg I, to principal quantum number $n \leq 9$, orbital quantum number $l \leq 4$, and the $3s^2\,{}^2S_{1/2}$ ground state of Mg II (Fig. 1).
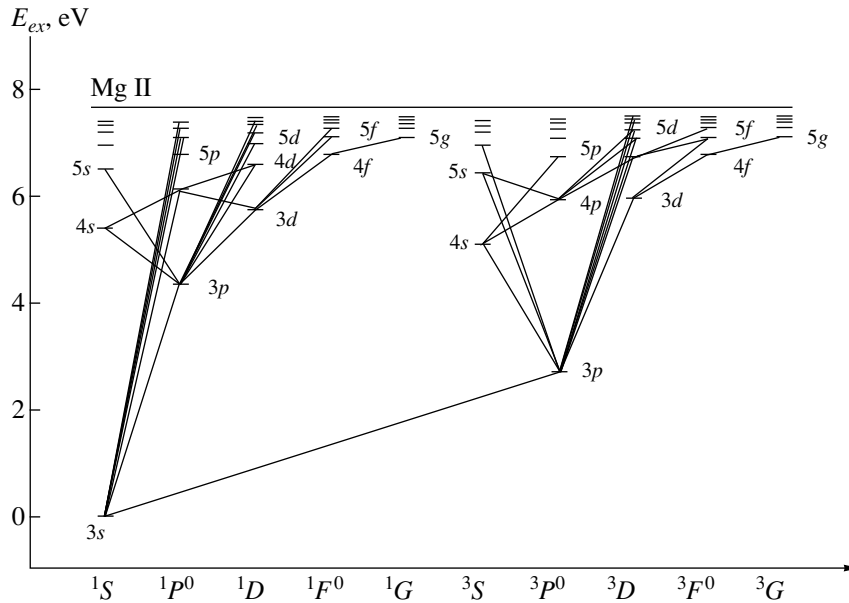
Fig. 1. Model of the Mg I atom. Linearized transitions are indicated.

The singlet and triplet level systems are considered together. We combined the singlet and triplet nf and ng levels, since the difference between their excitation energies is negligible. The lowest term of the triplet system, the metastable $3s3p\,^3P^0$ level, is coupled with the most important transitions in the magnesium atom; for this reason, we take into account its fine structure. In the equation for conservation of the particle number, we also included 13 levels of Mg II, whose populations we assumed to correspond to LTE, and the ground state of Mg III. The excitation energies for all terms were taken from [22]. In the statistical equilibrium equations, we took into account radiative processes in all 373 permitted and intercombinational bound–bound (b–b) transitions, all bound–free (b–f) transitions, and collisional processes due to interactions with both electrons and neutral hydrogen atoms.

We used the equations of Vainshtein *et al.* [23] to calculate the rates of collisional excitation by electrons for forbidden transitions between levels with $n \leq 6$, $l \leq 2$ in Born and Born–Coulomb approximations. We calculated the collision rates for all allowed transitions and the remaining forbidden transitions using the equation of van Regemorter [24], with the oscillator strengths for forbidden transitions set equal to 10% of those for nearby allowed transitions [15, 17] (cf. Section 5.2 in [9]). For all states, we used photoionization cross sections σ^{qdm} calculated using the quantum-defect method, provided by Hofsaess [25]. We took into account inelastic collisions with neutral hydrogen following the treatment of Steenbock and Holweger [26], varying the scaling factor k_{H} between 0 and 1.

In addition to the sources of opacity that are usually included in such studies, our continuum absorption calculations took into account 176 000 lines, as well as molecular opacity. We accounted for lines directly, using a Voigt profile for the opacity coefficient. The list of wavelengths and atomic data for all elements up to atomic number $Z = 60$ and up to the second ionization state were taken from [27]. We included absorption in the molecular bands of the diatomic molecules CO, NO, SO, SiO, TiO, MgO, VO, BO, AlO, CN, and MgH covering the wavelengths 1100–56 000 Å. The characteristics of the molecular bands were kindly supplied by V.Ya. Pavlenko. We used the "smeared-line" technique developed in [28] and kindly provided to us by Ya.V. Pavlenko to calculate the molecular absorption coefficients. To determine the number densities of molecules, we solved the system of nonlinear ionization and dissipation equilibrium equations in an LTE assumption using the NMOLEC routine [29]. We adopted data from [30] for the standard solar elemental abundances.

Since absorption in b–f transitions of Mg I from the $3s\,^1S$, $3p\,^1P^0$, and $3p\,^3P^0$ states plays a significant role in the total ultraviolet opacity, we included these in the list of transitions to be linearized. The total number of linearized transitions was 65. For these, the radiation field was determined via the simultaneous solution of the transport equations at the transition frequencies and the statistical equilibrium equations.

We computed the non-LTE populations of the Mg I levels using a complete linearization method with the NONLTE3 software developed by Sakhibullin [31]. We modified the standard technique of subdividing all transitions into fixed and linearized transitions by introducing recalculated transitions. For these transitions, we did not solve the linearized transport equations and instead recalculated the mean intensities after each iteration by

Table 1. Mg I lines studied and parameters for which the solar profiles are satisfactorily described for the *newKur* model atmosphere ($k_H = 0.5$, $\Delta\log\varepsilon_{Mg}^{\text{non-LTE}}$ are corrections to the standard abundance $\log\varepsilon_{Mg,\odot} = 7.58$)

λ, Å	Transition	$j''-j'$	$\log gf$	γ_R, 10^{-8}	$\log C_6$ (Uns)	$\Delta\log C_6$	$\Delta\log\varepsilon_{Mg}^{\text{non-LTE}}$, dex	ξ_t, km/s	W_λ^{obs}, mÅ
4571.085	$3s^{2\,1}S - 3p^3P^0$	0–1	−7.645	1.47×10^{-4}	−32.42	1.72	0.0	1.0	110.5
4571.089			−7.043						
4571.091			−6.737						
4571.093			−6.737						
4571.096			−6.177						
4571.099			−6.039						
11 828.180	$3p^1P^0 - 4s^1S$	1–0	−0.34	4.628	−31.40	1.44	0.0	0.8	897:
5711.088	$3p^1P^0 - 5s^1S$	1–0	−1.72	4.547	−30.66	0.77	−0.01	0.8	112
8806.757	$3p^1P^0 - 3d^1D$	1–2	−0.16	4.535	−31.63	0.86	−0.02	1.0	517
5528.405	$3p^1P^0 - 4d^1D$	1–2	−0.49	4.726	−30.75	0.44	0.01	0.8	330
4702.991	$3p^1P^0 - 5d^1D$	1–2	−0.52	4.632	−30.26	0.74	0.01	0.8	361:
8923.569	$4s^1S - 5p^1P^0$	0–1	−1.58	0.402	−30.50	1.31	−0.01	0.8	64
8213.034	$3d^1D - 6f^1F^0$	2–3	−0.51	0.422	−29.80	1.25	−0.04	0.8	178
5172.684	$3p^3P^0 - 4s^3S$	1–1	−0.381	5.271	−31.41	0.74	0.0	0.8	
5183.604	$3p^3P^0 - 4s^3S$	2–1	−0.158			0.72	0.0	0.9	
12 417.935	$4p^3P^0 - 6s^3S$	0–1	−1.63	0.242	−30.30	1.06	0.01	0.8	47:
12 423.032		1–1	−1.16			1.14	−0.01	0.8	99:
12 433.457		2–1	−0.94			1.19	−0.02	0.8	136:
8712.676	$4p^3P^0 - 7d^3D$	1–1	−1.67	0.223	−29.53				
8712.689		1–2	−1.26			1.03	−0.03	0.8	64
8717.803		2–1	−2.85						
8717.816		2–2	−1.85						
8717.825		2–3	−0.97			1.11	−0.03	0.8	92
6318.716	$4s^3S - 6p^3P^0$	1–2	−1.97	1.334	−30.08	1.39	0.03	0.8	49:
6319.236		1–1	−2.20				0.02	0.8	32:
6319.493		1–0	−2.61				0.02	0.8	12:

Note: The sign (:) indicates uncertain W_λ^{obs} measurements.

formally solving the transport equation. A similar approach was suggested by Hubeny and Lanz [32]. The magnesium abundance was varied in proportion to the total heavy-element content of the model; we adopted $\log\varepsilon_{Mg,\odot} = 7.58$ [30] for the standard solar value (on a logarithmic scale with $\log\varepsilon_H = 12.0$ for hydrogen).

In the calculations, we used blanketed, LTE Kurucz [21] model atmospheres with parameters appropriate for A–K stars: $T_{\text{eff}} = 4500$–12 000 K, in steps of 250 K; $\log g = 0.0$–4.5, in steps of 0.5; and metallicity [M/H] = 0 to −3, in steps of 0.5.

The line profiles were computed taking into account natural damping with $\gamma_R = \sum_{l<i} A_{il} + \sum_{l<j} A_{jl}$, Stark and van der Waals broadening, and the particles' ther-

mal motion and microturbulence. When computing the lines of the triplet system, we assumed that the populations of sublevels were proportional to their statistical weights. It is shown in [9] that the hyperfine structure of lines and isotope shifts influence the resulting magnesium abundances only slightly. Thus, we did not consider these effects for most lines. One exception is the λ 4571 Å line; we took its hyperfine splitting parameters and isotope shifts from [33] (Table 1). We took the isotope abundance ratio for magnesium, $^{24}Mg/^{25}Mg/^{26}Mg$, to be 0.79/0.10/0.11 [33]. The Stark broadening was calculated using the theory of Griem [34] or in accordance with [35]. We calculated the van der Waals broadening using the constant C_6 given by the formula of Unsöld [36]

[here and below, C_6(Uns)] with orbital radii $\overline{r^2}$ taken from [37].

3. ANALYSIS OF NON-LTE EFFECTS FOR THE MAGNESIUM ATOM

We calculated the level populations n_i in the Mg I atom and the profiles and equivalent widths of lines observed in the spectra of stars of various spectral types for the grid of model atmospheres. We will now investigate the influence of deviations from LTE on these values.

The Coefficients b_i.

As usual, we introduce the values $b_i = n_i/n_i^*$, where n_i, n_i^* are the number densities of atoms in level i without and with the assumption of LTE, respectively. It is known that the behavior of b_i with depth in the atmosphere is different for stars with different T_{eff}, $\log g$, and [M/H] (Fig. 2). The reasons for the corresponding distributions of the atoms over their states are also different, as we will now briefly discuss.

In stellar atmospheres with $T_{eff} > 5500$ K, neutral magnesium, which is not the main ionization state, experiences "superionization", i.e., additional ionization (compared to LTE) due to ultraviolet radiation emerging from deep, hot layers of the star's atmosphere. Figure 2a shows the behavior of the b_i for a solar model atmosphere with $T_{eff} = 5770$ K, $\log g = 4.44$, and [M/H] = 0 (we will write these model parameters 5770/4.44/0).

Deviations from LTE begin in layers where the medium becomes transparent to radiation above the thresholds for ionization from the $3p^1P^0$ ($\lambda_{thr} = 3753$ Å) and $3p^3P^0$ ($\lambda_{thr} = 2512$ Å) levels. At the corresponding optical depths ($\log \tau_{5000} < 0$), the temperature of radiation at the frequencies for ionization from these levels exceeds the local medium temperature, which determines recombination processes. For example, analysis of the radiative rates shows that, for this atmosphere, the ionization of the metastable level exceeds that of the $3p^1P^0$ level by a factor of 5–10. The effect of ionization of the ground level becomes appreciable only in surface layers, because of the low flux at the wavelengths in question ($\lambda_{thr} = 1620$ Å).

The $3s^1S$ state is also depleted via the resonance transition (λ 2850 Å). As a result, beginning with radiation formation depths beyond the threshold for ionization from the $3p^1P^0$ and $3p^3P^0$ levels, $b_i < 1$ for these three levels. The underpopulation of the lower levels is transferred to other levels via b–b transitions. As a result, the populations of most Mg I lines at the depths of line formation are lower than those for LTE.

Radiation in strong lines also redistributes atoms over states. As soon as the medium becomes transparent to radiation in the line core, strong depletion of the

transition's upper level begins, and its b_i value drops sharply. Analysis of the radiative rates shows that the $3p$ levels for the 5770/4.44/0 model atmosphere are mainly populated by transitions from the $4s$ and $3d$ levels (the $\lambda\lambda$ 11 828 and 8806 Å and $\lambda\lambda$ 5167–5183 and 3829–3838 Å lines for singlets and triplets, respectively). This leads to a slight overpopulation of the $3p^1P^0$ level at optical depths $-4.0 < \log \tau_{5000} < -3.24$.

Qualitatively, the character of processes leading to non-LTE effects does not change for stellar atmospheres with $T_{eff} > 7500$ K. We will briefly consider these processes using a 9000/4.0/0 model atmosphere as an example.

In the deepest atmospheric layers, $b_i = 1$ for all levels. At optical depths $\log \tau_{5000} < -0.89$, the medium becomes transparent to radiation beyond the ionization thresholds for the three lowest levels, and b_i ($3p^{1,3}P^0$, $3s^1S$) < 1 for these layers (Fig. 2d). The underpopulation of the lower states is transferred to other levels via b–b transitions. A strong depletion of the upper level of the transition begins in layers where τ_{λ_0} becomes less than unity. No overpopulation is observed for the $3p^1P^0$ state, because the $\lambda\lambda$ 11 828 and 8806 Å lines become weaker, and the efficiency of $4s^1S$, $3d^1D \longrightarrow 3p^1P^0$ transitions decreases. Since they are close to the continuum, the upper states are coupled to it by strong collisional processes, and the depletion of these levels by cascade transitions is compensated by recombination processes. The generally greater depletion of all Mg I states compared to the above case (the 5770/4.44/0 model; Fig. 2a) is due to increased photoionization.

For cooler stars (4500 K < T_{eff} < 5500 K), Mg I and Mg II are competing ionization states. In such atmospheres, the level populations deviate from their LTE values for a different reason: redistribution of atoms over states due to radiative processes in b–b transitions.

Using a 4500/4.0/0 model atmosphere as an example, let us consider the processes occurring in the magnesium atom (Fig. 2e). At this temperature, Mg I is the dominant ionization state and Mg II constitutes only a few percent of the total number of magnesium atoms. Thus, photoionization is not able to change this ratio; the populations of the $3s^1S$, $3p^1P^0$, and $3p^3P^0$ Mg I levels are close to their LTE values; and the $3s^2S$ Mg II state is very sensitive to changes in the Mg I level populations.

The λ 2850 Å resonance line is in detailed balance at all depths in the stellar atmosphere and does not influence the redistribution of atoms over excitation states. The mechanism determining repopulation of the $3s^1S$, $3p^1P^0$, and $3p^3P^0$ states at optical depths $-4.43 < \log \tau_{5000} < -1.41$ is recombination to upper levels and cascade transitions:
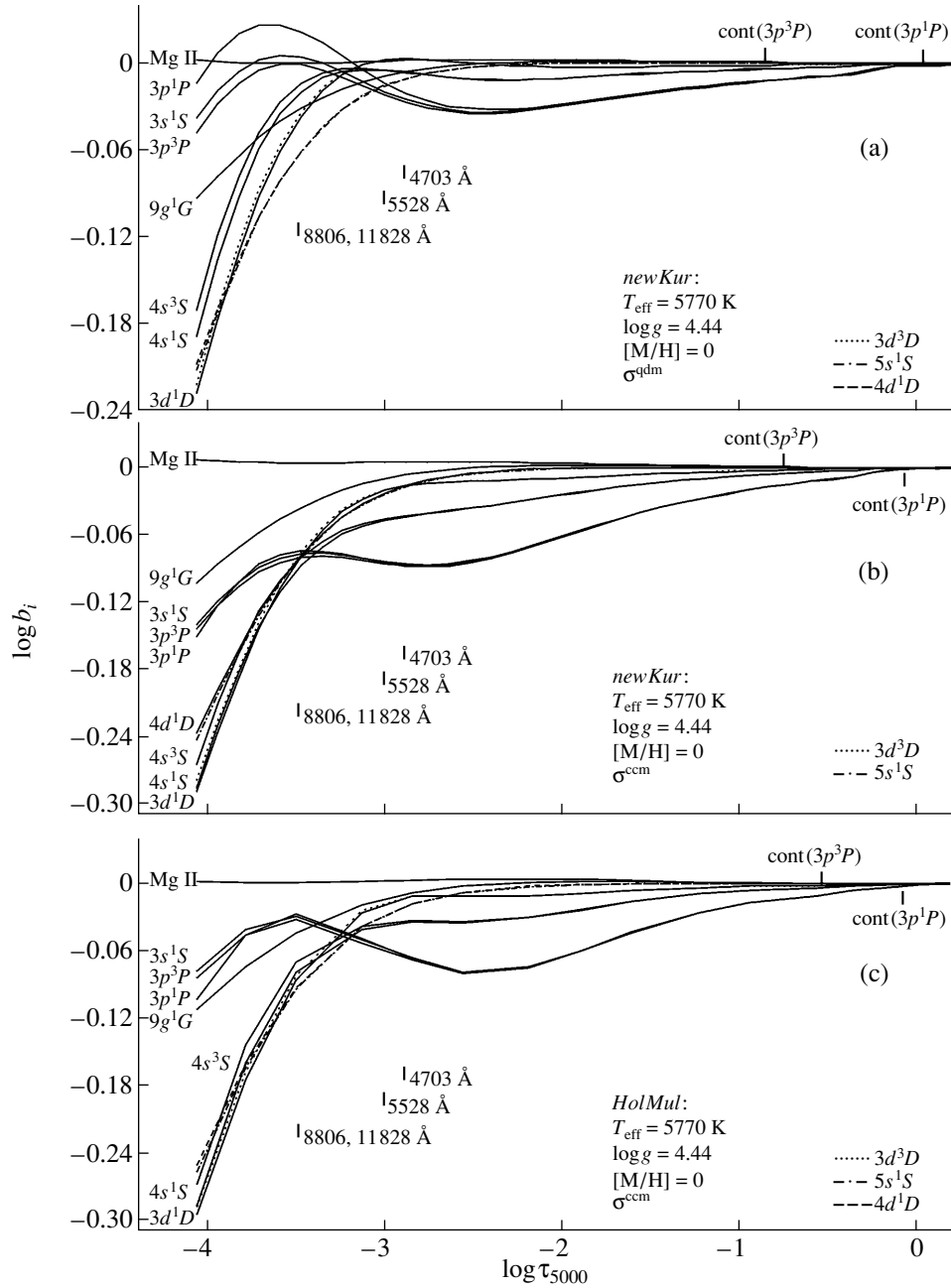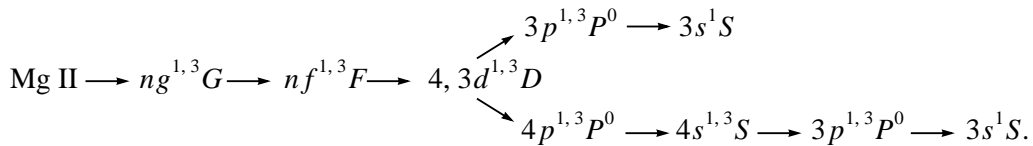
Fig. 2. Behavior of the coefficients b_i for Mg I levels with changing depth for several model atmospheres. Formation depths for the continuum and cores of some spectral lines are indicated.

$$Mg\,II \longrightarrow ng^{1,\,3}G \longrightarrow nf^{1,\,3}F \longrightarrow 4, 3d^{1,\,3}D \begin{array}{c} \nearrow 3p^{1,\,3}P^0 \longrightarrow 3s^1S \\ \\ \searrow 4p^{1,\,3}P^0 \longrightarrow 4s^{1,\,3}S \longrightarrow 3p^{1,\,3}P^0 \longrightarrow 3s^1S. \end{array}$$

Thus, $b_i\,(3s^2S\,Mg\,II) < 1$ when $-4.56 < \log\tau_{5000} < -1.3$.

In the dense atmospheres of cool dwarfs, there are intense collisional interactions between the singlet and triplet levels of the same electronic configuration, resulting in similar values of their coefficients b_i over a wide region in the stellar atmosphere. In the transition to giants with the same temperatures and metallicities, the
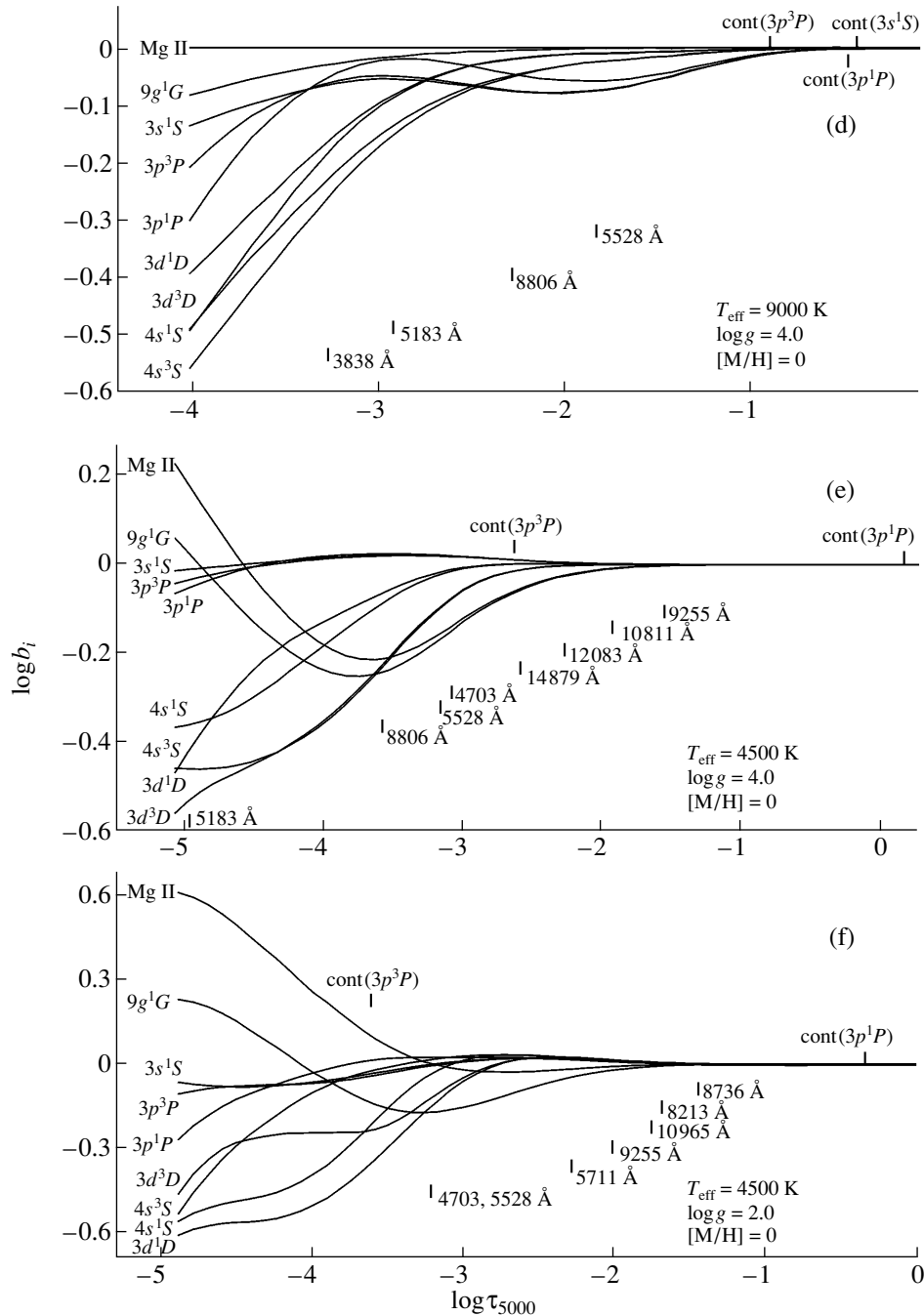
Fig. 2. (Contd.)

qualitative character of the described processes remains the same. However, the role of radiative processes increases, since the collisional interactions become less strong. This leads to the development of different coefficients b_i for different lines (Fig. 2f). For cool, metal-deficient stars, all the processes will lead to deviations from LTE, as described above (Fig. 2g).

4. ANALYSIS OF THE NEUTRAL MAGNESIUM SPECTRUM IN THE SOLAR ATMOSPHERE

4.1. Observational Material

The high quality of solar spectra makes it possible to conduct detailed analyses of the equivalent widths W_λ and profiles of both strong and weaker lines. In our analysis of solar Mg I lines, we used the spectrographic
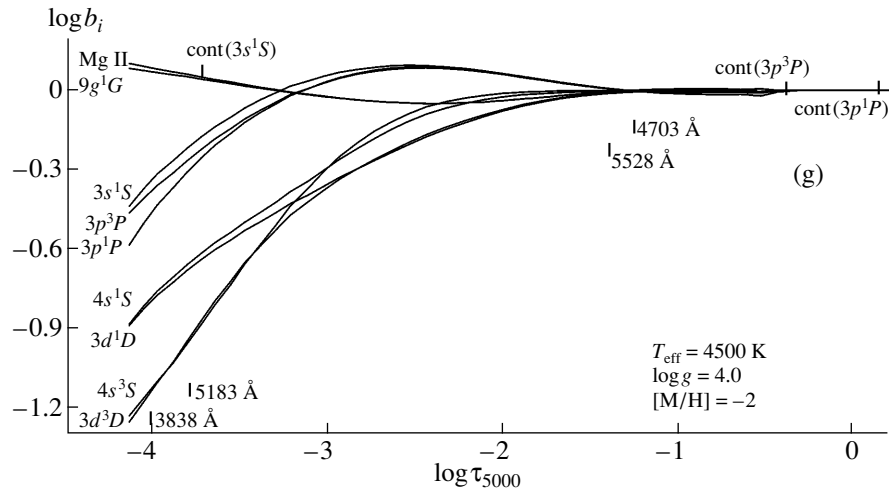
Fig. 2. (Contd.)

solar atlas [38], based on observations of fluxes from 2960 to 13 000 Å with spectral resolution $\lambda/\Delta\lambda = 522\,000$ in the red and infrared and $\Delta\lambda/\lambda = 348\,000$ in the ultraviolet, with signal-to-noise ratios $S/N = 2000–9000$. We selected 25 Mg I lines for which there was no blending or the contribution of blending could be estimated for the theoretical analysis. These lines belong to the spectroscopic series of transitions $ns–n'p$, $np–n's$, $np–n'd$, $nd–n'p$, and $nd–n'f$. The transitions were from lower atomic states with $n = 3$ and 4.

To measure W_λ, we used the Origin 3.1 package running under Windows 3.11. Very strong blending in the wings introduces considerable errors into the W_λ determinations for the $\lambda\lambda$ 4167, 4730, and 7291 Å lines and the magnesium abundances derived from them. For this

reason, we excluded these lines from the final analysis. The equivalent widths for the remaining lines were determined rather reliably, with the exception of the $\lambda\lambda$ 4703, 6318, 6319, 8209, 8310, 9986, 9993, 10 312, 11 828, 12 417–12 433 Å lines, which were blended in their wings. The $\lambda\lambda$ 5172 and 5183 Å lines were used only to compare the theoretical and observed profiles. The parameters of all the Mg I lines studied and their observed W_λ values are collected in Tables 1 and 2.

4.2. Results

We analyzed the profiles of the Mg I lines in order to empirically improve certain atomic parameters (the van der Waals broadening constant C_6 and the cross

Table 2. Parameters of the studied Mg I lines and $\Delta\log\varepsilon_{\mathrm{Mg}}^{\mathrm{non\text{-}LTE}}$ derived from W_λ^{obs} for *newKur* and *HolMul* ($k_{\mathrm{H}} = 0.5$ and 1.0, respectively) models with $\xi_t = 0.8$ km/s

λ, Å	Transition	$j''–j'$	$\log gf$	γ_R, 10^{-8}	$\log C_6$ (Uns)	$\Delta\log\varepsilon_{\mathrm{Mg}}^{\mathrm{non\text{-}LTE}}$, dex		W_λ^{obs}, mÅ
						newKur	*HolMul*	
8209.835	$3d^1D – 7p^1P^0$	2–1	−2.14	0.447	−29.71	0.04	0.08	13:
10 312.530	$4p^1P^0 – 7d^1D$	1–2	−1.58	0.439	−29.60	−0.03	0.00	22:
9983.200	$4p^3P^0 – 7s^3S$	0–1	−2.15	0.186	−29.90	0.02	0.07	11
9986.475		1–1	−1.67			0.06	0.07	30:
9993.209		2–1	−1.45			0.07	0.10	45:
8305.585	$4p^3 P^0 – 8d^3 D$	1–1	−1.90	0.136	−29.28			
8305.596		1–2	−1.45			0.02	0.08	44
8310.244		2–1	−3.08					
8310.255		2–2	−2.07					
8310.264		2–3	−1.15			0.03	0.10	63:

Note: The sign (:) indicates uncertain W_λ^{obs} measurements.

sections for photoionization and collisional interaction with hydrogen atoms) and refined our estimates of the microturbulence velocity ξ_t and abundances ε_{Mg}. In the modeling, we fixed the line oscillator strength f_{ij}, natural damping constant γ_R, and Stark broadening constant C_4, as well as the Sun's rotational velocity $V\sin i = 2.0$ km/s. The γ_R values were specified quite rigorously. In the solar atmosphere, Stark broadening of Mg I lines is not as strong as van der Waals broadening, so that it is not possible to refine C_4. Only the product $f_{ij}\varepsilon_{Mg}$ can be determined from profile analyses. Thus, fixing the oscillator strength, we transfer uncertainties in f_{ij} to the parameter ε_{Mg}. We varied all other parameters to achieve the best agreement between the theoretical and observed line profiles.

In our calculations, we used the 1994 Kurucz solar model atmospheres [21] (*newKur*) and the 1974 models of Holweger and Müller [39] (*HolMul*). In addition, in our analyses of the profiles of the strongest Mg I lines, we used a model atmosphere with a chromospheric rise, constructed by combining the *newKur* model with part of the VAL–C model [40] above the temperature minimum.

We took into account the instrumental profile by convolving the theoretical profiles with a Gaussian whose half-width corresponded to the spectral resolution of the atlas used. We included the effect of microturbulence when computing the line profiles, imitating, to a first approximation, the granulation of the solar atmosphere with the radial and tangential components of a Gaussian velocity distribution. We determined the microturbulence parameter ζ_{RT} for each line; the values for various lines were between 1.8 and 4.0 km/s.

4.2.1. Refined Cross Sections for Photoionization and Collisional Interactions with H Atoms

Photoionization cross sections. The behavior of the non-LTE deviations of Mg I lines in solar-type stars is determined by the underpopulation of most of the lower atomic levels discussed above, with the magnitude of the deviation also dependent on the photoionization cross sections. Therefore, these cross sections are important for the levels of Mg I. We studied two versions of the computations, using photoionization cross sections determined via the quantum-defect method [25], σ^{qdm}, and the close-coupling method [41], σ^{ccm}. The threshold cross sections for the ground and metastable states in these two methods differ only insignificantly:

$$\sigma_0^{qdm}(3s^1S) = 1.55 \text{ Mbarn}$$

$$\text{and } \sigma_0^{ccm}(3s^1S) = 2.93 \text{ Mbarn},$$

$$\sigma_0^{qdm}(3p^3P^0) = 21.02 \text{ Mbarn}$$

$$\text{and } \sigma_0^{ccm}(3p^3P^0) = 16.2 \text{ Mbarn}.$$

However, the cross sections for the $3p^1P^0$ level differ by a factor of six:

$$\sigma_0^{qdm}(3p^1P^0) = 12.3 \text{ Mbarn}$$

$$\text{and } \sigma_0^{ccm}(3p^1P^0) = 73.5 \text{ Mbarn}.$$

Figure 3 shows the cross sections σ^{qdm} and σ^{ccm} for the first s, p, d, and f singlet and triplet levels of Mg I. We can see that the general behavior of σ^{qdm} and σ^{ccm} as functions of wavelength (or energy) is also present for the $3d^1D$ and $4f^3F$ levels, with the exception of resonances. For the remaining levels, there are differences for photon energies $E > 0.8$ Ry of the ionization threshold. Significant differences in the run of the cross sections for the $3p^1P^0$ level are already observed starting with the ionization threshold.

Let us consider the impact of these differences for σ^{qdm} and σ^{ccm} on the populations of the Mg I atomic levels. In Section 2, we discussed processes occurring in the Mg atom when using photoionization cross sections derived using the quantum defect method, σ^{qdm} (Fig. 2a for the *newKur* model solar atmosphere). Figure 2b shows the behavior of the coefficients b_i if we use σ^{ccm} in the calculations for the same model atmosphere. Using σ^{ccm} leads to stronger depletion of the s, p, and d singlet and triplet levels with principal quantum numbers $n = 3$–5, compared to the results for σ^{qdm}. The strongest reduction of b_i, by 22%, occurs for the $3p^1P^0$ level (Fig. 2b). This is due to the large value of $\sigma^{ccm}(3p^1P^0)$ near the threshold, so that the rates of photoionization from the $3p$ singlet and triplet levels become comparable (they differ by only a factor of 1.4–2). Cross-section resonances do not contribute appreciably to ionization from Mg I levels. For higher Mg I atomic levels ($n > 5$), differences in the behavior of b_i are insignificant throughout the atmosphere.

The stronger non-LTE effects obtained when using cross sections σ^{ccm} lead to significantly weaker $\lambda\lambda$ 4703, 5528, 8806, and 11828 Å lines compared to those obtained when σ^{qdm} is used. For the *newKur* model solar atmosphere, the central depth of these lines decreases by as much as 24%. To describe the line profiles in the solar spectrum in this case, we must increase the magnesium abundance by 0.2–0.4 dex compared to the $\Delta\varepsilon_{Mg}$ values derived from weak lines that are insensitive to non-LTE effects. For the strong $\lambda\lambda$ 5172, 5183, 8806, and 11828 Å lines, it is impossible to obtain agreement between the profiles, even when ε_{Mg} is significantly increased: the theoretical profiles remain narrower than the observed ones.

We have a similar situation when σ^{ccm} is used in computations of the photoionizaton rates for the *HolMul* model atmosphere. The behavior of b_i in this case is shown in Fig. 2c. When σ^{ccm} is used with the *HolMul* model, the central depths of the $\lambda\lambda$ 4703, 5528, 8806, 11828 Å lines are reduced by 23% compared to the results for σ^{qdm}. In this case, we must increase the magnesium abundance by 0.1–0.3 dex over the values derived from weak lines in order to fit the profiles.
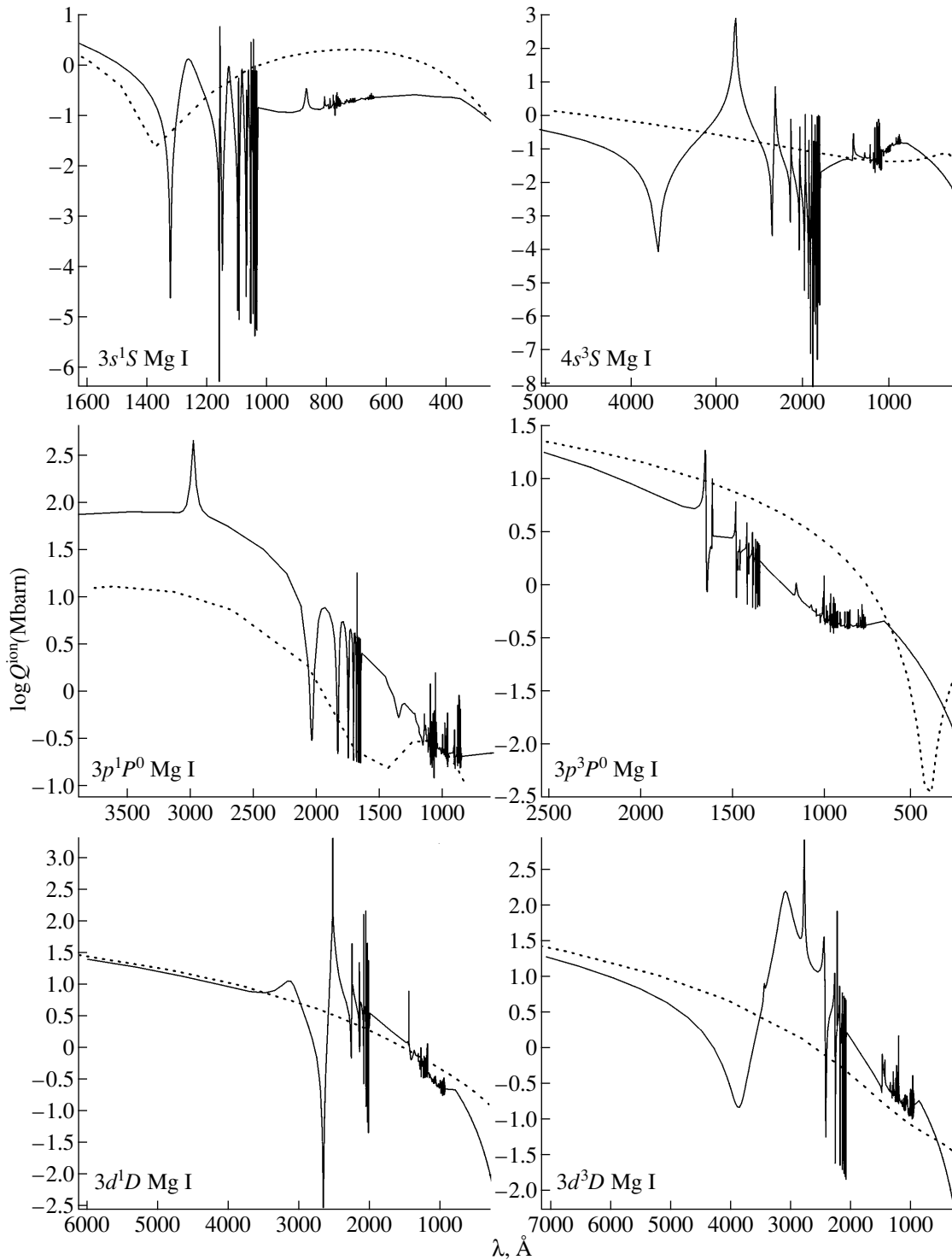
Fig. 3. Photoionization cross sections computed with the quantum defect method, σ^{qdm} (dashed), and with the close-coupling method, σ^{ccm} (solid), for several levels of Mg I.

However, if we use the σ^{qdm} photoionization cross sections, it is possible to obtain agreement with minimal internal dispersion for the profiles of all lines in the solar spectrum (Tables 1–3), for both the *newKur* (see Fig. 5 below) and *HolMul* model atmospheres, using ε_{Mg} values that do not differ from those derived from weak lines. For this reason, we favor the photoionization cross sections σ^{qdm}, computed using the quantum-defect method.
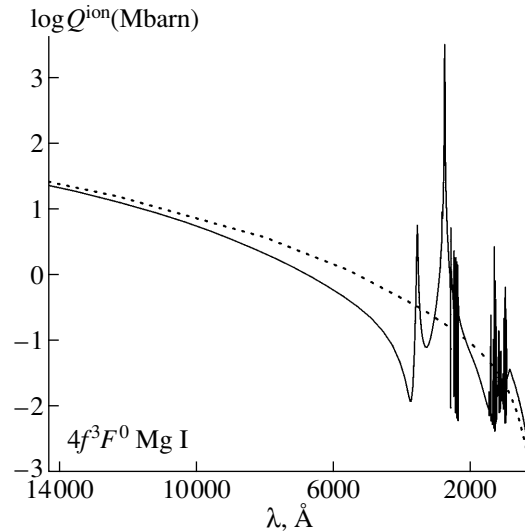
Fig. 3. (Contd.)

Collisional excitation and ionization by H atoms. Neutral particles interact with a much lower efficiency than charged particles. However, under certain conditions, when the electron density is much lower than the density of neutral particles (for example, the electron density in the atmospheres of solar-type dwarfs is lower than the density of H atoms by three to four orders of magnitude), more frequent collisions with neutral particles can compensate for low interaction cross sections. In this study, we describe collisions with H atoms leading to the excitation and ionization of Mg I levels using the formulas of Steenbock and Holweger [26], who estimate their uncertainty to be about an order of magnitude. For this reason, a scaling coefficient k_H, specific to each chemical element and to be determined empirically, is usually added to these formulas.

It is possible to determine the value of k_H for Mg I by fitting the observed and theoretical profiles of the $\lambda\lambda$ 8806 and 11 828 Å infrared lines, which are sensitive to this parameter. The lines have saturated cores, so that they are insensitive to abundance changes. Their profiles, as well as non-LTE corrections to them, are determined by collisional interactions with hydrogen atoms. Let us consider this using the λ 8806 Å line as an example, using the *newKur* model and the cross sections σ^{qdm}. Figure 4 shows the non-LTE profiles computed with $k_H = 0$ and 0.5 for fixed values of the remaining computational parameters. When $k_H = 0$, the discrepancies between the observed and theoretical profiles are 2.5% in both the core and wings; these discrepancies can be removed only by changing the scaling coefficient. It is clear that increasing k_H decreases the depth and increases the Doppler half-width of the lines. Thus, by varying k_H, we were able to achieve satisfactory fits of the solar profiles for these two lines for both the *newKur* (with k_H equal to 0.5) and *HolMul* (with k_H equal to 1.0) models (Tables 1, 3).

In summary, our theoretical descriptions of the profiles of the solar $\lambda\lambda$ 4703, 5172, 5183, 5528, 5711, 8806, and 11828 Å lines obtained using the *newKur* and *HolMul* model solar atmospheres and photoionization cross sections computed using the quantum-defect and close-coupling methods, σ^{qdm} and σ^{ccm}, for k_H from 0 to 1 lead us to the following conclusions.

(1) For both the *newKur* and *HolMul* model atmospheres, we are able to achieve a satisfactory fit of the line profiles only using σ^{qdm}.

(2) The scaling coefficient k_H depends on the model atmosphere adopted. When using the cross sections σ^{qdm} in the computations, the optimum k_H values for the *newKur* and *HolMul* models are 0.5 and 1.0, respectively.
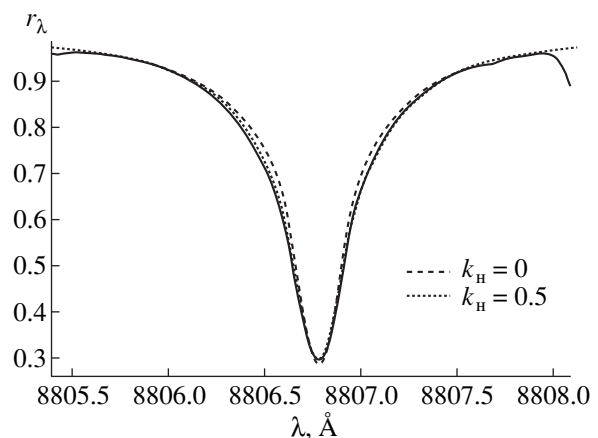

Fig. 4. Non-LTE profiles of the λ 8806 Å line computed for the *newKur* model solar atmosphere with values for the scaling factor in the Steenbock and Holweger formula $k_H = 0$, 0.5; the remaining computational parameters were fixed. The solid curve is the observed profile.

Table 3. Parameters providing satisfactory fits of *HolMul* solar line profiles ($k_H = 1.0$, $\Delta\log\varepsilon_{Mg}^{non\text{-}LTE}$ are corrections to the standard abundance $\log\varepsilon_{Mg,\odot} = 7.58$)

λ, Å	$\log gf$	$\Delta\log C_6$	$\Delta\log\varepsilon_{Mg}^{non\text{-}LTE}$, dex	ξ_t, km/s
4571.085	−7.645	1.72	0.1	1.0
4571.089	−7.043			
4571.091	−6.737			
4571.093	−6.737			
4571.096	−6.177			
4571.099	−6.039			
11828.180	−0.34	1.26	0.13	0.8
5711.088	−1.72	0.66	0.09	0.8
8806.757	−0.16	0.68	0.10	1.0
5528.405	−0.49	0.28	0.13	0.8
4702.991	−0.52	0.68	0.11	0.8
8923.569	−1.58	1.31	0.05	0.8
8213.034	−0.51	1.25	0.06	0.8
12417.935	−1.63	1.06	0.05	0.8
12423.032	−1.16	1.14	0.05	0.8
12433.457	−0.94	1.19	0.05	0.8
8712.676	−1.67			
8712.689	−1.26	1.03	0.03	0.8
8717.803	−2.85			
8717.816	−1.85			
8717.825	−0.97	1.11	0.04	0.8

4.2.2. Refining the van der Waals Broadening Constant

By comparing theoretical and observed line profiles, we can derive empirical values for $C_6(prof)$ ($\log C_6(prof) = \log C_6(Uns) + \Delta\log C_6$) (Tables 1, 3). The corrections $\Delta\log C_6$ for the $\lambda\lambda$ 5172 and 5183 Å lines (0.74 and 0.72, respectively) are close to the theoretical value given in [42] for the λ 5167 Å Mg I line of the same multiplet (0.75). The derived correction factors for $C_6(Uns)$ for lines formed in transitions from the 3^1P^0 level are not large ($\Delta\log C_6 < 1.0$), except for the correction for λ 11828 Å. Lines formed in transitions between high levels, and also the $\lambda\lambda$ 4571 and 11828 Å lines, have large corrections to $C_6(Uns)$.

Note that the van der Waals broadening constant depends on the model atmosphere used. We determined empirical values of $C_6(prof)$ for 13 lines of Mg I using the *HolMul* model atmosphere (Table 3). Table 3 shows that these values coincide with those derived for lines formed in transitions between high levels when the *newKur* model is used. For the rest of the studied lines, the $C_6(prof)$ values determined from *HolMul* computations are lower than those for the *newKur* model. The differences occur primarily for the strongest lines and reach 13–35%.

Zhao *et al.* [20] also derived empirical values of the van der Waals broadening constant from their analysis of the solar spectroscopic atlas [38]. Using their own model atmosphere, they derived systematically lower $C_6(prof)$ values. For example, for ten lines in common with our study, their values differ from those for our *newKur* computations by 7–30%, and the discrepancies for the $\lambda\lambda$ 4703, 5711, and 8213 Å lines are 40–49%.

Thus, corrections to the van der Waals broadening constant must be specific not only for each line of a particular chemical element but also for each model atmosphere grid. Underestimation of C_6 can result in overestimation of the abundance of the given element.

4.2.3. The Microturbulence Velocity, ξ_t

The optimum value of the microturbulence velocity for the Sun is 0.8 km/s (Tables 1, 3). If ξ_t is further increased, the theoretical Doppler line half-width becomes larger than the observed width. The thermal velocity of magnesium lines in the solar atmosphere is 2 km/s, and the total line half-width will become sensitive to the value of ξ_t only if $\xi_t > 0.8$ km/s. Thus, $\xi_t = 0.8$ km/s is only an upper limit for the microturbulence velocity.

4.2.4. The Magnesium Abundance in the Solar Atmosphere

Our computations show that, for the solar atmosphere, the non-LTE corrections to the magnesium abundance ($\log\varepsilon^{non\text{-}LTE} - \log\varepsilon^{LTE}$) are fairly low, ±0.01 dex. The non-LTE magnesium abundances derived using all line profiles studied here and the optimum computational parameters given above (Tables 1, 3) are $\log\varepsilon_{Mg,\odot} = 7.58 \pm 0.02$ and 7.66 ± 0.03 dex for the *newKur* and *HolMul* model atmospheres, respectively.

The use of line-profile analysis and refined van der Waals broadening constants makes it possible to obtain virtually the same solar-atmosphere magnesium abundance from strong Mg I lines and weaker lines, whose intensities are independent of ξ_t and C_6. For example, our non-LTE magnesium abundances based on the observed equivalent widths W_λ^{obs} for seven weak lines (Table 2) using $\xi_t = 0.8$ km/s are $\log\varepsilon_{Mg,\odot} = 7.61 \pm 0.03$ dex and $\log\varepsilon_{Mg,\odot} = 7.65 \pm 0.03$ dex for the *newKur* and *HolMul* model atmospheres, respectively. Our solar-atmosphere magnesium abundance coincides with the meteoritic value only for the *newKur* computations.

For comparison, Table 4 presents magnesium abundances $\log\varepsilon_{Mg}$ derived from Mg I lines in the solar atmosphere in other studies (columns 6 and 7), the meteorite Mg abundance (column 8), and the results of our non-LTE computations for the two model atmospheres (*newKur*, columns 2 and 3, and *HolMul*, columns 4 and 5). The results in columns 6 and 7 were

Table 4. Mg abundances in the solar atmosphere $\log\varepsilon_{Mg}$ (dex) derived from Mg I lines in various studies

Parameters	Model						
	newKur, line profiles	*newKur*, weak lines	*HolMul*, line profiles	*HolMul*, weak lines	[43]	[44]	meteorites [30]
1	2	3	4	5	6	7	8
No. of lines	18	7	13	7	15	21	
$\log\varepsilon_{Mg}$	7.58	7.61	7.66	7.65	7.36	7.59	7.58
$\sigma_{(n)}$	0.02	0.03	0.03	0.03	0.13	0.13	

obtained assuming LTE. For their analysis of the Mg I spectrum of the solar photosphere, Lambert and Warner [43] selected weak ($W_\lambda \le 100$ mÅ) infrared lines at wavelengths 5780–15890 Å. Their equivalent widths were taken from published photometric atlases and catalogs and are systematically lower (by 7–22%) than the values we determined for the same lines. They determined LTE abundances using their own model of the solar atmosphere based on the spectral energy distribution from 5000 Å to 13 μm, with $\cos\theta \ge 0.2$; ξ_t was taken to be 1.8 km/s. The abundances derived from individual Mg I lines are in the range $7.15 < \log\varepsilon_{Mg}^{LTE} < 7.60$ dex, with a mean value 7.36 ± 0.13 dex. The low magnesium abundance found by Lambert and Warner [43] is due to the high value of the microturbulence velocity they used. We compared their and our abundances for the seven lines common to the two studies: $\lambda\lambda$ 6318, 6319, 8712, 8923, 9983, 9986, and 9993 Å. When calculating $\log\varepsilon_{Mg}^{non\text{-}LTE}$, we used the W_λ^{obs} values determined by Lambert and Warner [43]. The resulting non-LTE abundances for the *newKur* model and $\xi_t = 1.8$ km/s do not differ from those of Lambert and Warner [43] by more than 0.02–0.04 dex. The difference for the λ 8712 Å line is 0.06 dex. The *HolMul* $\log\varepsilon_{Mg}^{non\text{-}LTE}$ values are somewhat higher (by 0.03 dex). Since non-LTE corrections to the solar magnesium abundances do not exceed 0.01 dex, these difference must be due to differences in the model atmospheres used and underestimation of the van der Waals broadening constant (for the λ 8712 Å line).

Later, Lambert and Luck [44] redetermined the abundances of several elements using a Holweger and Müller [39] model atmosphere with $\xi_t = 1.0$ km/s. They used infrared Mg I lines with $W_\lambda < 120$ mÅ at wavelengths 6310–21500 Å to calculate the LTE magnesium abundance, with equivalent widths derived from published photometric intensity atlases. The abundances derived using individual Mg I lines are in the range $7.29 < \log\varepsilon_{Mg}^{LTE} < 8.06$ dex, with a mean value 7.59 ± 0.13 dex. We compared the abundances of Lambert and Luck [44] with those determined by us for eleven Mg I lines common to the two studies ($\lambda\lambda$ 6318, 6319, 8209, 8305, 8310, 8712, 8717, 10312, and

12417–12433 Å), using the same model solar atmosphere (*HolMul*), ξ_t, and f_{ij} values for the lines. We also used the W_λ^{obs} values determined by Lambert and Luck [44]. The magnesium abundances from [44] for seven weak and four strong lines are 7.51 ± 0.12 and 7.63 ± 0.09 dex, respectively. It appears that the van der Waals broadening constant used by Lambert and Luck [44], which was underestimated for strong lines, is the origin of the high magnesium abundance derived from these lines. The larger scatter of the $\log\varepsilon_{Mg,\odot}$ values found by them using all the Mg I lines they considered could also be due to inaccurate account of van der Waals broadening for strong lines.

The $\log\varepsilon_{Mg,\odot}$ values found by us using the W_λ from [44] for weak and strong lines together with the *HolMul* model and C_6(prof) (Table 3) coincide (7.50 ± 0.11 and 7.51 ± 0.08 dex, respectively). These values also coincide with the magnesium abundance determined in [44] for the weak lines common to the two studies. In this case, however, the magnesium abundance differs by 0.15 dex from that found by us for the same *HolMul* model atmosphere based on the profiles of 13 Mg I lines. These discrepancies in $\log\varepsilon_{Mg,\odot}$ could indicate that using equivalent widths in abundance determinations can lead to errors, even for the Sun.

Figure 5 presents profiles of several of the Mg I lines studied, computed for the *newKur* model atmosphere for the parameters specified in Table 1. This figure shows that the LTE profile of the λ 5183 Å line derived for the model atmosphere with the chromospheric rise has an emission component in the central part of the line core, which is not observed. The situation with the λ 5172 Å line is similar. Taking into account deviations from LTE enabled us to completely remove the emission peak and achieve good agreement between the theoretical and observed profiles of these lines.

Thus, our adopted model for the Mg I atom and the set of atomic data needed to calculate the rates of collisional and radiative processes can provide a correct description of the formation of magnesium lines in the spectra of solar-type stars.
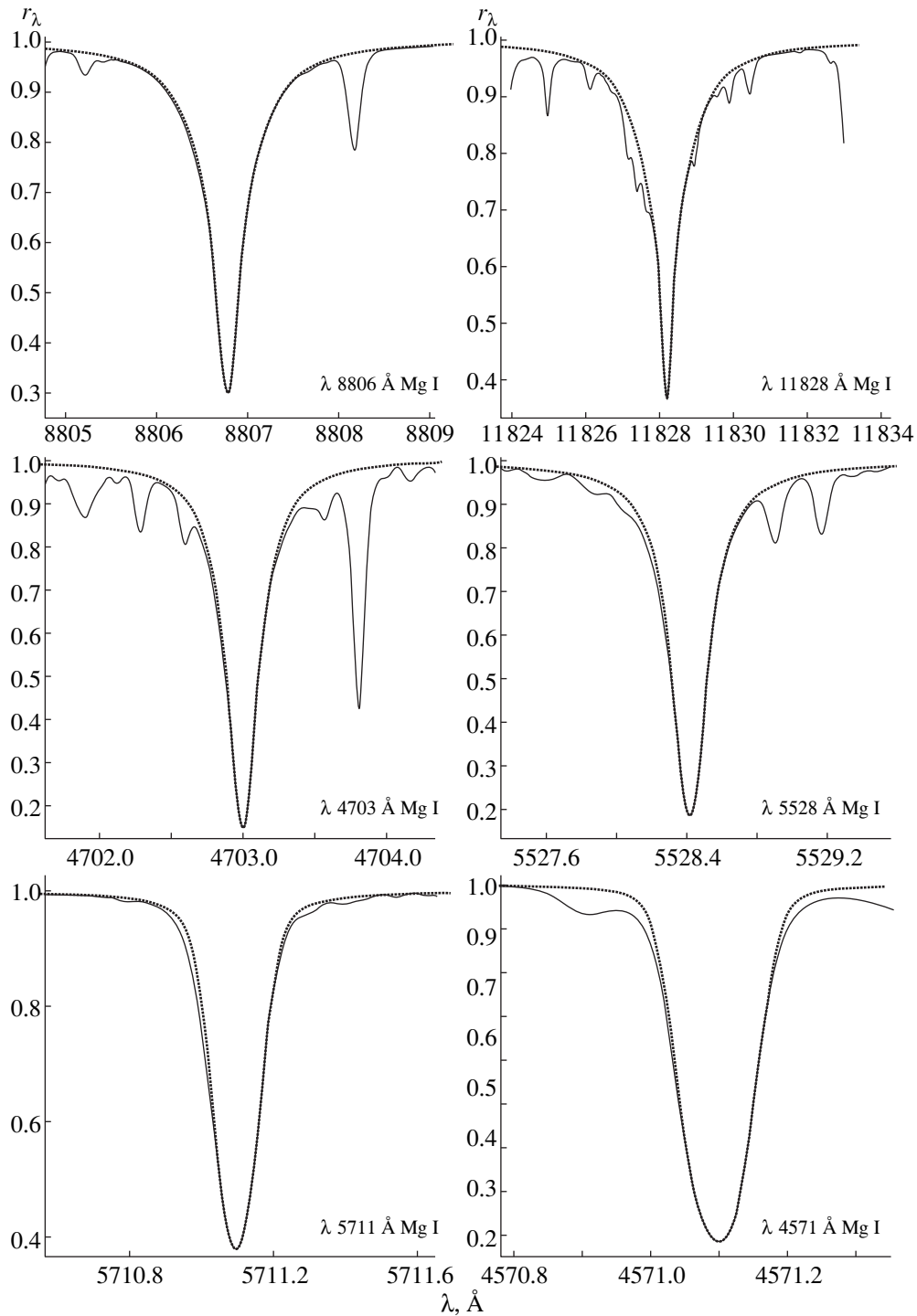
Fig. 5. Comparison between the observed (solid) and non-LTE theoretical (dotted) profiles of several Mg I lines for the Sun. The LTE profile is shown for the λ 5183 Å line (dashed).

5. DEPENDENCES OF THEORETICAL NON-LTE CORRECTIONS TO MAGNESIUM ABUNDANCES ON STELLAR ATMOSPHERIC PARAMETERS

Let $\Delta X = \log \varepsilon^{\text{non-LTE}} - \log \varepsilon^{\text{LTE}}$ be the theoretical correction to the magnesium abundance for non-LTE

effects. Figures 6–8 present the dependences of ΔX on T_{eff} for various $\log g$ values for Mg I five spectral lines. These dependences have jump-like discontinuities in the range from 5000 to 8000 K, probably due to the description of convection used when computing the Kurucz model atmospheres [21]. Lines with equivalent
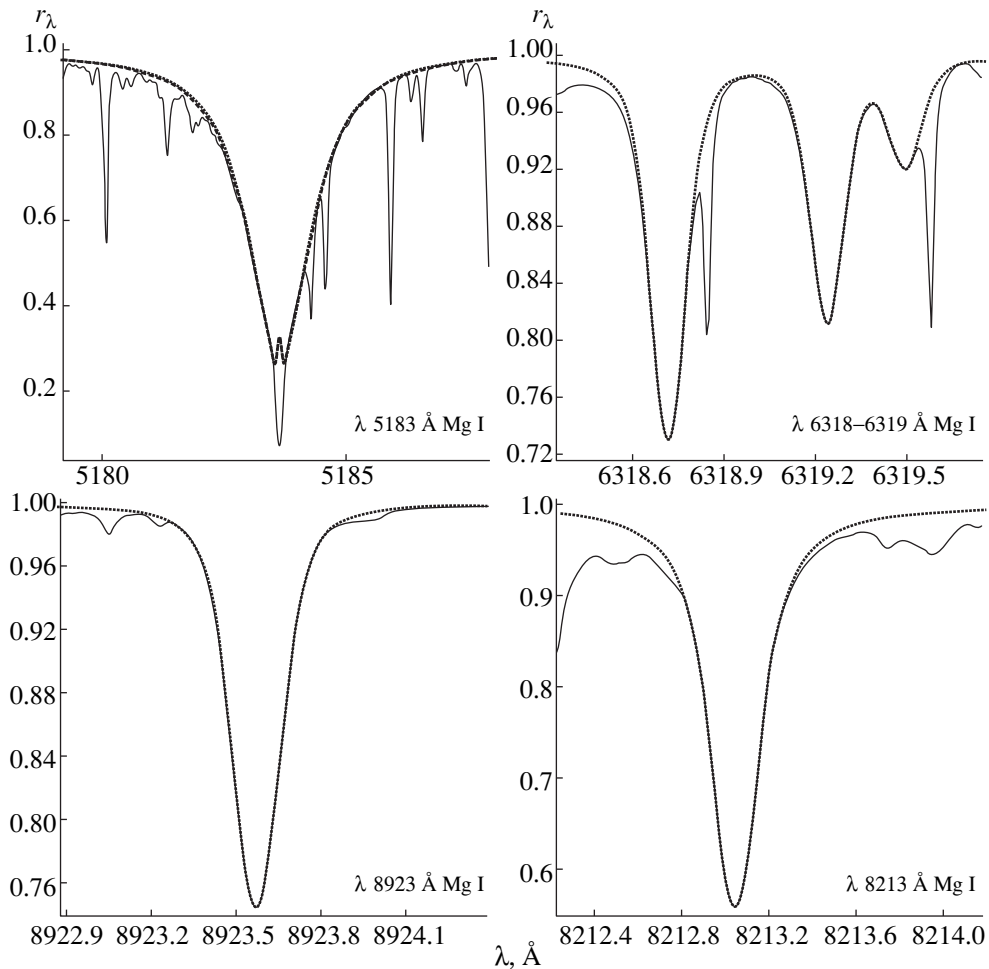
Fig. 5. (Contd.)

widths exceeding 7 mÅ in the particular model atmosphere considered were used for the analysis. For this reason, the ΔX–T_{eff} relations for each Mg I line are terminated at different T_{eff} values for stars with different luminosities. To help illustrate the behavior shown in these relations, let us consider the properties of Mg I line formation for one of the model atmospheres, e.g., the 5770/4.44/0 solar model (Fig. 2a for the coefficients b_i). Our conclusions will also be valid for other stellar model atmospheres.

Deviations from LTE in the equivalent widths of spectral lines result from two factors: the source function S_{ij} in the corresponding transition differs from the local Planck function, and/or the b_i value for the transition's lower level differs from unity. When $h\nu_{ij} > kT$ (valid for all the magnesium lines studied in the temperature range of interest), the source function for transition $i \longrightarrow j$ can be written $S_{ij} \approx b_j/b_i * B_\nu(T(\tau))$. Analyzing the behavior of the coefficients b_i in the region of formation of spectral lines, we can judge probable origins for deviations of the line radiation from the LTE

case. Both factors change the depth where the line radiation is formed. However, the role of these factors is different for lines with different intensities. Let us consider this in more detail.

For strong lines, the difference between the b_i values for the lower and upper levels is substantial in the region where they form. Therefore, the difference of S_{ij} from $B_\nu(T)$ is the dominant mechanism leading to deviations from LTE. Note that b_i can be either larger or smaller than b_j. For example, it is apparent from Fig. 2a that, for the λ 5183 Å line, $b_i < b_j$ at optical depths $\log\tau_{5000} > -3.24$ and $b_i > b_j$ at lower optical depths; for the λ 8806 Å line, $b_i < b_j$ at optical depths $\log\tau_{5000} > -3.12$ and $b_i > b_j$ at lower optical depths. Thus, the total energy absorbed in a line can be larger as well as smaller than in LTE. As a result, for a single model atmosphere, lines of different multiplets can differ in both the value and sign of their ΔX corrections.

Both factors are important for moderately strong lines. At all formation depths, $b_i < 1$ and $b_i < b_j$; i.e., $S_{ij} > B_\nu$. Since these lines form in deep layers, their
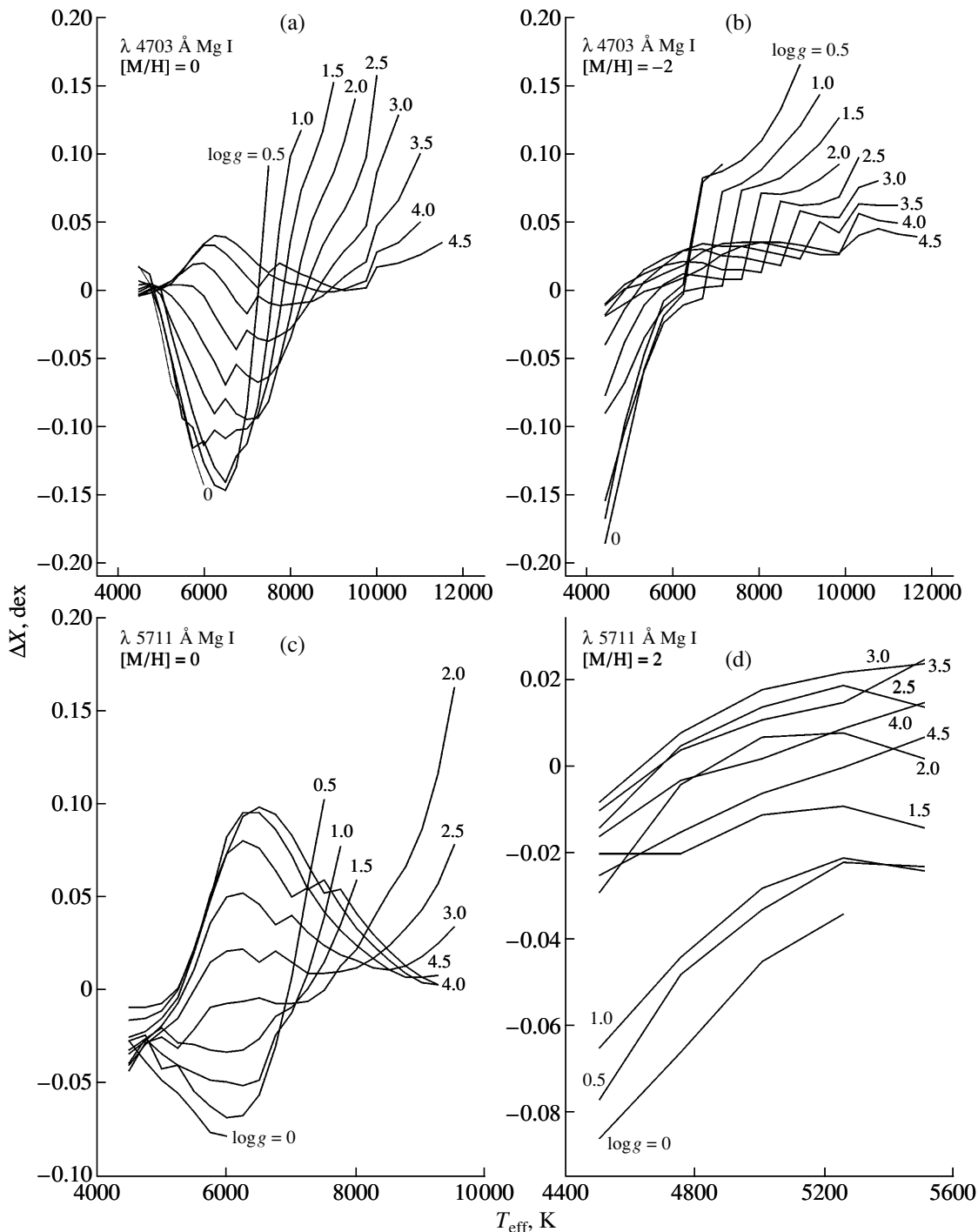
Fig. 6. Dependences of the theoretical non-LTE corrections to the magnesium abundance ΔX on T_{eff} for various $\log g$ and metallicities [M/H] values for the $\lambda\lambda$ 4703 and 5711 Å lines.

absolute differences, $\Delta\tau_{5000}$ and ΔT, are appreciable (cf. Table 2 in [9]). Thus, the formation of these lines under non-LTE conditions takes place at higher local temperatures $T(\tau)$. This leads to weaker non-LTE lines and positive corrections to the magnesium abundance ΔX.

Weak lines are formed in deeper atmospheric layers. For this reason, the difference between the b_i values for

their upper and lower levels is smaller, and the role of the second factor increases. One example is the known semi-forbidden line Mg I λ 4571 Å, whose coefficients $b(3s^1 S)$ and $b(3p^3 P_1^0)$ nearly coincide over its entire depth of formation (Fig. 2a). For such lines, the LTE and non-LTE line-formation depths, and hence the tempera-
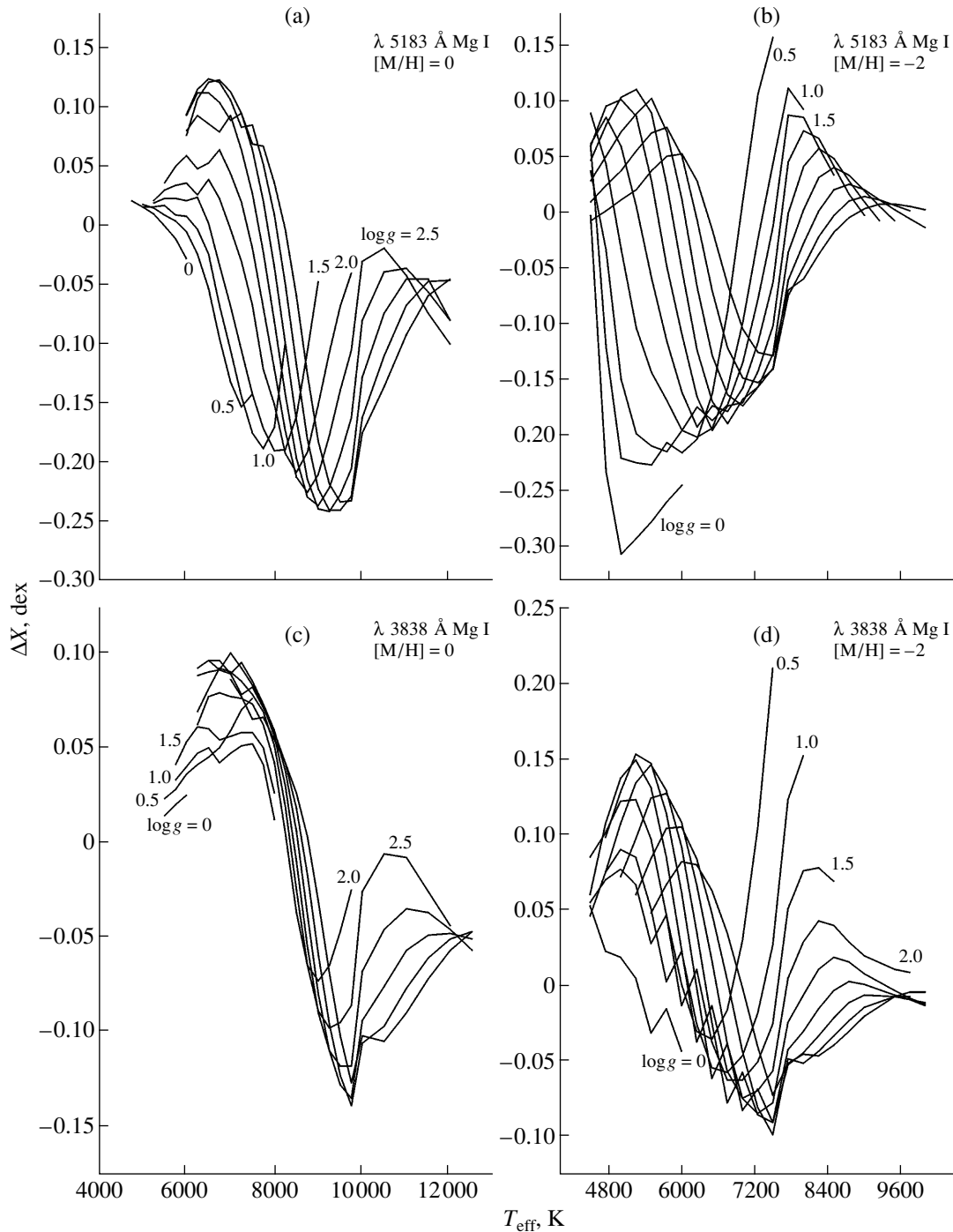
Fig. 7. Same as Fig. 6 for the $\lambda\lambda$ 5183 and 3838 Å line.

tures of the layers, differ even more (cf. Table 2 in [9]). The corrections ΔX will be positive, as in the previous case.

The absolute value of the abundance correction depends on the line's position on the curve of growth: the corrections are largest at the saturated part of the curve and are smallest on the linear portion. Below, we identify and discuss groups of lines with similar behav-

ior in their non-LTE corrections for various model atmosphere parameters.

Singlet Lines Corresponding to the $3p^1P^0-ns^1S$ and $3p^1P^0-nd^1D$ Transitions (Fig. 6).

For stars with different luminosities but $T_{eff} < 5000$ K, the difference of $b(3p^1P^0)$ from unity is small and is manifest only near the saturated Doppler core. The change in the non-LTE equivalent width compared to
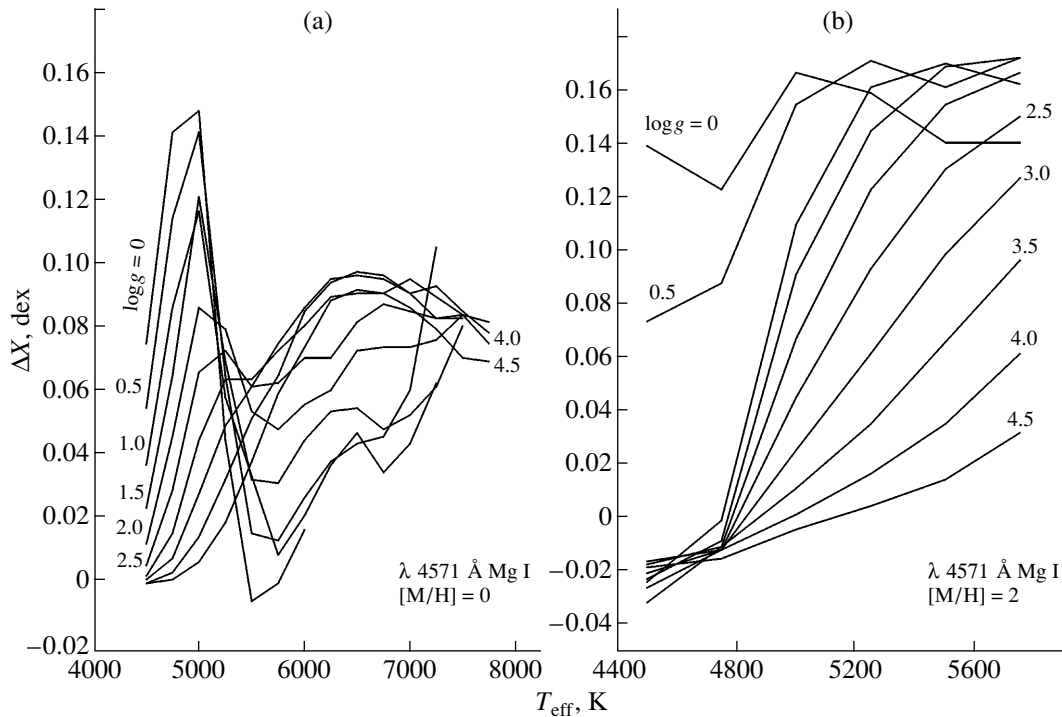
Fig. 8. Same as Fig. 6 for the λ 4571 Å line.

its LTE value is insignificant, and $\Delta X \sim 0$. For higher $T_{\rm eff}$, the distribution of the atoms over their states is different. The $3p^1P^0$ level is depleted by ionization in deep layers, $b_i < b_j$, and $S_{ij} > B_\nu(T)$. In higher layers, cascade transitions deplete the s and d states, $b_i > b_j$, and $S_{ij} < B_\nu(T)$. Thus, the line cores are enhanced and the wings weakened compared to the LTE case. Therefore, the sign of ΔX can be either positive or negative.

For stars with normal metallicities, at $T_{\rm eff} = 5000$–7500 K, the cores of the strong λλ 5528 and 4703 Å lines, which correspond to the $3p^1P^0$–$4d^1D$, $5d^1D$ transitions, are formed in a region where $b_i > b_j$. The corrections for these lines are negative for giants ($\Delta X = 0.0$ to –0.18 dex; the lines are on the saturated portion) and close to zero for dwarfs ($\Delta X = 0.03$ to –0.06 dex; the lines are on the saturated portion) (Fig. 6a). At higher temperatures, these lines become weaker, their formation depth moves to layers where $b_i < b_j$, and ΔX becomes positive.

The weaker λ 5711 Å line ($3p^1P^0$–$5s^1S$ transition) forms in a region where $b_i < b_j$ already when $T_{\rm eff} > 5500$ K. As a result, the non-LTE corrections for this line are positive ($\Delta X < 0.12$ dex) over the entire range of temperatures exceeding 5500 K for stars with $\log g > 2.0$ (Fig. 6c).

For supergiants, the corrections for these lines can reach –0.2 dex for $T_{\rm eff} < 7500$ K and +0.15 dex at higher temperatures. *At lower metallicities,* the lines become weaker and are formed in deeper layers. For dwarfs, at the line-formation depth, the coefficients b_i and b_j are ~1.

Therefore, deviations from LTE are small for these parameters (not exceeding +0.06 dex; Figs. 6b, 6d). The situation is different for giants. At low temperatures ($T_{\rm eff} < 5500$ K), $b_i > b_j$ and ΔX can reach –0.24 dex. At higher temperatures, the ratio b_j/b_i becomes greater than unity in the region of line formation and ΔX becomes positive, increasing to +0.16 dex.

Triplet Lines Corresponding to the $3p^3P^0$–ns^3S and $3p^3P^0$–nd^3D Transitions (Fig. 7).

For stars with solar heavy-element abundances, $b_i > b_j$ in the line-formation region at low temperatures ($T_{\rm eff} < 5500$ K) (Figs. 2d, 2e). The lines are strong and occupy the damped portion of the curve of growth. The corresponding corrections are small and positive (<0.05 dex). As the temperature increases, the lines become weaker and move to the saturated part of the curve of growth and their formation depth moves to layers with $b_i < b_j$. This leads to negative non-LTE corrections (to $\Delta X = -0.25$ dex). For subgiants and dwarfs with $T_{\rm eff} > 9000$ K, these lines move to the linear portion of the curve of growth, leading to lower $|\Delta X|$ values. This transition occurs at lower temperatures for giants.

The ΔX–$T_{\rm eff}$ relations for stars with different luminosities and metallicities have similar shapes. The extremes of the functions move toward lower temperatures as the luminosity increases.

The Intercombination Line Corresponding to the $3s^2{}^1S$–$3p^3P^0$ Transition (Fig. 8).

As noted above, the non-LTE corrections for the λ 4571 Å semi-forbidden line are positive. ΔX increases

with T_{eff} but does not exceed +0.15 dex anywhere in the studied range of parameters.

6. CONCLUSIONS

We have studied non-LTE effects for a wide range of stellar parameters for the Mg I lines usually used to determine magnesium abundances. The computations show that non-LTE corrections to the magnesium abundances are not large for dwarf and subdwarf stars: the magnitudes of the corrections for the $\lambda\lambda$ 4571, 4703, 5528, and 5711 Å lines are below 0.1 dex. For such stars, more substantial non-LTE corrections (±0.2 dex) are characteristic of the $\lambda\lambda$ 3829–3838, 5172, and 5183 Å triplet lines. For giants and supergiants with various metallicities, the magnitudes of the non-LTE corrections for the $\lambda\lambda$ 4571 and 5711 Å lines do not exceed 0.15 dex, but the corrections can reach ±0.2 dex or even more for the $\lambda\lambda$ 4703, 5528, 3829–3838, 5172, and 5183 Å lines.

ACKNOWLEDGMENTS

REFERENCES

1. R. E. Luck and H. E. Bond, Astrophys. J. **292**, 559 (1985).
2. R. C. Peterson, Astrophys. J. **244**, 989 (1981).
3. R. G. Gratton and S. Ortolani, Astron. Astrophys. **137**, 6 (1984).
4. R. G. Gratton and C. Sneden, Astron. Astrophys. **178**, 179 (1987).
5. P. Magain, Astron. Astrophys. **209**, 211 (1989).
6. B. Edvardson, J. Andersen, B. Gustafsson, *et al.*, Astron. Astrophys. **275**, 101 (1993).
7. K. Fuhrmann, Astron. Astrophys. **338**, 161 (1998).
8. P. E. Nissen and W. J. Schuster, Astron. Astrophys. **326**, 751 (1997).
9. L. I. Mashonkina, N. N. Shimanskaya, and N. A. Sakhibullin, Astron. Zh. **73**, 212 (1996) [Astron. Rep. **40**, 187 (1996)].
10. Ya. V. Pavlenko, *Effects of Deviation from LTE in the Atmospheres of M Giants* [in Russian] (Valgus, Tallin, 1984).
11. Ya. V. Pavlenko, Astrofizika **28** (1), 163 (1988).
12. Ya. V. Pavlenko, Astrofizika **29** (3), 520 (1988).
13. R. G. Athay and R. C. Canfield, Astrophys. J. **156**, 695 (1969).
14. M. Lemke and H. Holweger, Astron. Astrophys. **173**, 375 (1987).
15. E. Chang, E. Avrett, P. Mauas, *et al.*, Astrophys. J. Lett. **379**, L79 (1991).
16. D. Hoang-Binh, Astron. Astrophys. **241**, L13 (1991).
17. E. H. Avrett, E. S. Chang, and R. Loeser, *IAU Symp. No. 154: Infrared Solar Physics* (Kluwer, Dordrecht, 1992), p. 3.
18. M. Carlsson, R. J. Rutten, and N. G. Shchukina, Astron. Astrophys. **253**, 567 (1992).
19. P. J. Mauas, E. H. Avrett, and R. Loeser, Astrophys. J. **330**, 1008 (1988).
20. G. Zhao, K. Butler, and T. Gehren, Astron. Astrophys. **333**, 219 (1998).
21. R. L. Kurucz, CD-ROM No. 13 (1994).
22. C. Moore, *Atomic Energy Levels*, Natl. Bur. Stand. Circ. (U. S.) 467, Vol. 1 (1949).
23. L. A. Vaĭnshteĭn, I. I. Sobel'man, and E. A. Yukov, *Excitation of Atoms and Broadening of Spectral Lines* (Nauka, Moscow, 1979; Springer, Berlin, 1981).
24. H. van Regemorter, Astrophys. J. **136**, 906 (1962).
25. D. Hofsaess, At. Data Nucl. Data Tables **24**, 285 (1979).
26. W. Steenbock and H. Holweger, Astron. Astrophys. **130**, 319 (1984).
27. R. L. Kurucz, SYNTHE Spectrum Synthesis Programs and Line Data, CD-ROM, No. 18 (1994).
28. S. E. Nersisyan, A. V. Shavrina, and A. A. Yaremchuk, Astrofizika **30** (2), 247 (1989).
29. R. L. Kurucz, SAO Special Report, No. 309, 1 (1970).
30. E. Anders and N. Grevesse, Geochim. Cosmochim. Acta **53** (1), 197 (1989).
31. N. A. Sakhibullin, Tr. Kazan. Gor. Astron. Obs. **48**, 9 (1983).
32. I. Hubeny and T. Lanz, Astron. Astrophys. **262**, 501 (1992).
33. A. A. Radtsig and B. M. Smirnov, *Reference Data on Atoms, Molecules, and Ions* (Springer, Berlin, 1985; Énergoatomizdat, Moscow, 1986).
34. H. R. Griem, *Spectral Line Broadening by Plasmas* (Academic, New York, 1974; Mir, Moscow, 1978).
35. C. Cowley, Observatory **91**, 139 (1971).
36. A. Unsöld, *Physik der Sternatmospheren*, 2nd ed. (Springer, Berlin, 1955).
37. B. Warner, Z. Astrophys. **69**, 161 (1968).
38. R. L. Kurucz, I. Furenlid, J. Brault, and L. Testerman, in *Solar Atlas from 296 to 1300 nm* (Nat. Solar Obs. Sunspot, New Mexico, 1984).
39. H. Holweger and E. A. Müller, Sol. Phys. **39**, 19 (1974).
40. P. Maltby, E. H. Avrett, M. Carlsson, *et al.*, Astrophys. J. **306**, 284 (1986).
41. M. J. Seaton, C. J. Zeippen, J. A. Tully, *et al.*, Rev. Mex. Astron. Astrofis. **23**, 19 (1992).
42. W. Fullerton and Ch. R. Cowley, Astrophys. J. **165**, 643 (1971).
43. D. L. Lambert and B. Warner, Mon. Not. R. Astron. Soc. **140**, 197 (1968).
44. D. L. Lambert and R. E. Luck, Mon. Not. R. Astron. Soc. **183**, 79 (1978).

Translated by N. Samus'

The Normal Energy Distributions in Stellar Spectra: Giants and Supergiants

L. N. Knyazeva and A. V. Kharitonov

Fesenkov Astrophysical Institute, Academy of Sciences of Kazakhstan, Kamenskoe Plato, Almaty, 480068 Kazakhstan
Received August 10, 1999

Abstract—We have derived the normal spectral energy distributions for those early-type subgiants, giants, and supergiants that were not investigated in our earlier studies, which were in most cases also not included in the studies of Sviderskiene. Color indices computed using our normal energy distributions are in good agreement with normal colors derived from observations in the Vilnius photometric system. The reliability of our distribution curves is also demonstrated by comparisons of observed and computed $(W–B)–(B–V)$ two-color diagrams in the *WBVR* system. Normal color indices for the photometric *WBVR* system are derived. © *2000 MAIK "Nauka/Interperiodica".*

1. NORMAL ENERGY DISTRIBUTIONS

In this study, we derive the normal energy distributions for O9-G2 subgiants, giants, and supergiants. These stars were not included in our earlier work [1–7], and many were also not included in the analysis of Sviderskiene [8]. Similar to our previous studies [1–7], we attempted to

(1) use sufficiently representative samples of stars with available spectral energy distribution data;

(2) consider spectrophotometric data only from photometrically homogeneous sources [9–12];

(3) give preference as much as possible to homogeneous data on spectral classification and *UBV* photometry.

For most stars, we used the spectral-classification and photometry data from the new edition of the Bright Star catalog [13]; only for two faint stars did we use the data from [14].

When selecting the stars for the study, we excluded all peculiar and variable stars. Several suspected variables were kept in the list, since their brightness changes were less than a few hundredths of a magnitude and they displayed relatively constant colors. Such variability does not compromise our results, since it is within the accuracy of the spectrophotometric data used.

Table 1 lists the subgiant and giant stars selected together with their HD numbers, *B–V* color indices, trigonometric parallaxes (π), and Galactic latitudes (*b*), taken from the Bright Star Catalogue [13], as well as references to the spectrophotometric data (A for the Almaty catalog [9]; M for the Moscow catalog [10]; P for the Pulkovo catalog [11]; and C for the Cygnus-region catalog [12]).

We assume that these stars do not experience appreciable interstellar reddening on the following grounds. Within each spectral subtype, we have at least one

fairly bright star that is sufficiently close to the Sun and sufficiently far from the Galactic plane to be considered unreddened. These stars are denoted with asterisks in Table 1. Recordings of spectra from the OAO [15], TD-1 [16], and IUE [17] missions are available for some of these stars. These spectra show no $\lambda 2200$ Å band, confirming the absence of reddening. Within each subtype, differences in the *B–V* values for the unreddened star and the remaining stars do not exceed 0.06^m, demonstrating that all the selected stars can be assumed to be unreddened. In our subsequent analysis, comparisons of the scaled energy distributions for stars of a given spectral subtype revealed no significant distortions in the shapes of the spectral energy curves.

The supergiants used in the study are listed in Table 2; this table is similar to Table 1 but also provides information on the color excesses of the stars. Most of the supergiants experience interstellar reddening, which we removed using the relation

$$E_0(\lambda) = E(\lambda)/\tau(\lambda)^{E(B-V)},$$

where $E(\lambda)$ is the energy distribution distorted by interstellar reddening, $E(B-V)$ is the color excess, and $\tau(\lambda)$ is the transparency curve per unit mass of interstellar matter according to [18], where it is calculated for an amount of interstellar material giving a color excess equal to unity.

Usually, $E(B-V)$ values are determined as differences between observed and normal color indices. However, taking into account the natural dispersion in the color indices, differences in the normal color indices derived in different studies, and the fact that the normal color indices are not mean values, but instead extreme blue values for stars of a given subtype, we deviated somewhat from the usual procedure.

In those subtypes where there was no star that could be assumed to be unreddened (O9.5Iab, B2Iab,

Table 1. Subgiants and giants used to derive the normal energy distributions

HD	V	B–V	π	b	Remarks	HD	V	B–V	π	b	Remarks
B9IV						79931	5.47	−0.09	–	27	A
5408	5.55	−0.07	0.″007	−03°	A	87504	4.60	−0.09	–	33	A
6972	5.57	−0.09	–	02	A	144206	4.76	−0.11	–	48	A
86360*	5.26	−0.04	0.018	47	A	212097	4.81	−0.00	0.023	−24	A
141556	3.95	−0.04	–	16	P	218700	5.39	−0.08	–	−46	A
196867	3.77	−0.06	0.008	−15	A, P	220599	5.57	−0.11	0.004	−27	A
222439	4.14	−0.08	0.018	−17	A, P	A0III					
B6III						55075	6.31	−0.04	–	28°	A
23302	3.70	−0.11	0.020	−24	A	87887	4.49	−0.04	0.″015	42	A
155763*	3.17	−0.12	0.023	35	A, M, P	123299	3.65	−0.05	0.018	51	A, M
182255	5.18	−0.12	–	05	A, M	216336*	4.46	−0.04	0.043	−64	P
192987	6.48	−0.09	–	01	C	A3III					
195810	4.03	−0.13	0.025	−17	A, P	33111*	2.79	0.13	0.050	−25	A, P
196662	5.22	−0.12	–	−31	M	50019	3.60	0.10	0.021	15	A, M
197226	6.51	−0.12	–	−02	C	191747	5.52	0.08	0.002	−04	A, M
B7III						A5III					
3240	5.08	−0.11	–	−09	A	8538	2.68	0.13	0.037	−03	A
35497*	1.65	−0.13	0.028	−04	A	13161	3.00	0.14	0.022	−25	A, M
47395	6.03	−0.08	0.002	10	A, P	76543	5.20	0.15	–	35	A
49340	5.12	−0.13	0.002	26	A	159561*	2.08	0.15	0.067	23	M, P
B8III						173880	4.36	0.13	0.032	09	A, P
11529	4.99	−0.10	–	07	A	A7III					
12303	5.04	−0.08	–	−07	A	28319	3.40	0.18	0.029	−22	A, M, P
23408	3.87	−0.07	–	−24	A	70060	4.45	0.22	0.057	01	P
23850	3.63	−0.09	–	−23	A	102249	3.64	0.16	–	−05	P
47670	3.17	−0.11	–	−21	P	127762*	3.03	0.19	0.025	66	A, M
106625*	2.59	−0.11	–	45	A, P	195725	4.22	0.20	0.038	14	A
173300	3.17	−0.11	–	−11	P	197051	3.42	0.16	0.035	−36	P
207840	5.77	−0.10	–	−26	A	216701	6.11	0.20	–	−50	A
B9III						F0III					
144	5.59	−0.03	–	02	A	58923	5.25	0.22	0.010	11	M
2011	5.40	−0.00	0.015	−01	A	89025*	3.44	0.31	0.017	55	A
15318*	4.28	−0.06	0.030	−48	A, P	181333	5.53	0.26	0.004	−01	M

Table 2. Supergiants used to derive the normal energy distributions

HD	V	$B–V$	π	b	$E(B–V)$	Remarks
			O9.5Iab			
30614	4.29	0.03	–	14°	0.26	A
188209	5.62	−0.07	0$''$.009	10	0.16	A, C
209975	5.11	0.08	–	06	0.31	A
			B1Iab			
2905	4.16	0.14	–	00	0.28	A, M
24398	2.85	0.12	0.010	−17	0.26	A, M, P
91316*	3.85	−0.14	0.011	53	–	A, M
157246	3.34	−0.13	–	−12	–	P
			B2Iab			
14818	6.25	0.31	–	−04	0.44	A
41117	4.63	0.28	0.025	−01	0.35	A, M
165024	3.66	−0.08	–	−14	0.06	P
206165	4.73	0.30	–	07	0.39	M
			B5Iab			
13267	6.36	0.33	–	−04	0.43	A
36371	4.76	0.34	–	−01	0.39	A
58350*	2.45	−0.08	–	−07	–	P
164353	3.97	0.02	–	13	0.10	M
			B9Iab			
21291	4.21	0.41	–	03	0.42	A
202850	4.23	0.12	0.011	−07	0.13	A, M
212593	4.57	0.09	0.003	−07	0.13	A, M
			G2Iab			
67594	4.34	0.97	0.003	16	–	A
145544	3.85	1.11	0.029	−09	–	P
159181*	2.79	0.98	0.013	33	–	A, M, P
209750	2.96	0.98	0.012	−42	–	A, M, P

B9Iab), we chose the color excesses to achieve the best agreement for the shape of the spectral energy distributions for this subtype, corrected for reddening and scaled to unity at λ5475 Å; as a first approximation, we used the normal color indices from [18]. In addition, we compared the intensities of the λ2200 Å band in the spectra of these stars obtained with the OAO [15], TD-1 [16], and IUE [17] satellites and checked for consistency of these data with our adopted color excesses.

In the B1Iab, B5Iab, and G2Iab subtypes, there are stars that have $(B–V)$ within 0.04–0.05^m of the normal values, are fairly bright, are located far from the Galactic plane, and show no λ2200 Å band in their spectra. We assumed these stars to be unreddened, and they are marked with asterisks in Table 2. In each of these subtypes, we determined the color excesses for reddened stars relative to the color excesses for these stars. The next-to-last column of Table 2 presents the resulting color excesses, which we used in our reddening calculations.

We derived the normal energy distributions for each of the spectral subtypes studied as simple averages of the energy distributions for the individual stars, scaled to unity at λ5475 Å. The data are expressed in the energy distribution scale for Vega of Hayes [19]. Our final results are summarized in Tables 3 and 4.

2. COMPUTATION OF NORMAL COLOR INDICES

In order to evaluate the reliability of the normal energy distributions obtained by us here and in [1–7], we derived normal color indices for each spectral sub-

Table 3. Standard energy distributions for subgiants and giants

λ, Å	B9IV	B6III	B7III	B8III	B9III	A0III	A3III	A5III	A7III	F0III
3225	1.421	2.107	2.056	1.766	1.427	1.097	0.699	0.703	0.635	0.548
3275	1.387	2.035	1.985	1.703	1.369	1.076	0.704	0.714	0.649	0.561
3325	1.346	1.961	1.913	1.642	1.322	1.065	0.699	0.720	0.662	0.574
3375	1.307	1.898	1.837	1.583	1.277	1.030	0.696	0.708	0.648	0.581
3425	1.279	1.835	1.791	1.535	1.246	1.020	0.703	0.712	0.663	0.586
3475	1.250	1.761	1.732	1.489	1.210	0.989	0.702	0.708	0.651	0.578
3525	1.230	1.713	1.706	1.457	1.198	0.981	0.700	0.712	0.654	0.589
3575	1.211	1.678	1.684	1.445	1.185	0.980	0.695	0.711	0.675	0.595
3625	1.192	1.645	1.656	1.416	1.176	0.965	0.702	0.712	0.668	0.605
3675	1.185	1.618	1.659	1.415	1.178	0.981	0.733	0.735	0.705	0.646
3725	1.239	1.698	1.755	1.555	1.287	1.088	0.845	0.788	0.783	0.734
3775	1.552	1.954	2.081	1.895	1.608	1.438	1.090	1.008	0.970	0.885
3825	1.905	2.219	2.327	2.206	1.936	1.807	1.327	1.212	1.155	1.047
3875	2.146	2.404	2.478	2.423	2.096	2.050	1.590	1.466	1.379	1.269
3925	2.403	2.495	2.492	2.667	2.223	2.174	1.709	1.534	1.483	1.253
3975	1.899	2.084	2.030	2.118	1.843	1.767	1.433	1.297	1.247	1.272
4025	2.596	2.602	2.670	2.712	2.522	2.536	2.153	2.011	1.944	1.672
4075	2.107	2.298	2.416	2.315	2.165	2.180	1.747	1.680	1.622	1.445
4125	2.111	2.196	2.227	2.233	2.052	1.932	1.699	1.612	1.563	1.444
4175	2.287	2.304	2.362	2.313	2.226	2.214	1.934	1.845	1.778	1.573
4225	2.215	2.233	2.314	2.233	2.170	2.160	1.902	1.828	1.765	1.570
4275	2.137	2.162	2.232	2.116	2.090	2.078	1.822	1.768	1.721	1.529
4325	1.614	1.816	1.870	1.729	1.678	1.626	1.369	1.317	1.244	1.243
4375	1.922	1.947	1.998	1.971	1.884	1.823	1.622	1.555	1.532	1.404
4425	1.919	1.916	1.971	1.914	1.878	1.862	1.689	1.643	1.587	1.447
4475	1.834	1.842	1.888	1.817	1.810	1.798	1.654	1.606	1.554	1.437
4525	1.786	1.788	1.832	1.762	1.750	1.733	1.599	1.567	1.530	1.402
4575	1.719	1.730	1.767	1.709	1.687	1.678	1.557	1.525	1.484	1.381
4625	1.668	1.672	1.710	1.662	1.647	1.640	1.537	1.517	1.483	1.380
4675	1.620	1.611	1657	1.607	1.594	1.580	1.496	1.477	1.446	1.347
4725	1.552	1.567	1.590	1.556	1.535	1.537	1.451	1.433	1.412	1.310
4775	1.485	1.497	1.528	1.493	1.473	1.483	1.402	1.374	1.372	1.281
4825	1.331	1.433	1.422	1.407	1.353	1.386	1.262	1.247	1.273	1.182
4875	1.176	1.220	1.259	1.231	1.158	1.094	1.048	0.999	0.985	1.048
4925	1.383	1.371	1.400	1.373	1.339	1.344	1.291	1.260	1.256	1.197
4975	1.342	1.332	1.344	1.328	1.311	1.329	1.260	1.246	1.241	1.173
5025	1.291	1.281	1.296	1.279	1.269	1.278	1.226	1.207	1.197	1.161
5075	1.256	1.242	1.267	1.246	1.237	1.244	1.201	1.190	1.187	1.137
5125	1.215	1.207	1.211	1.201	1.195	1.208	1.167	1.158	1.152	1.116
5175	1.184	1.178	1.174	1.170	1.165	1.181	1.136	1.120	1.110	1.084
5225	1.141	1.136	1.142	1.134	1.127	1.127	1.106	1.101	1.095	1.064
5275	1.112	1.110	1.109	1.107	1.099	1.102	1.091	1.083	1.067	1.049
5325	1.078	1.083	1.072	1.077	1.070	1.068	1.066	1.056	1.050	1.029
5375	1.053	1.053	1.053	1.053	1.054	1.047	1.046	1.036	1.040	1.021
5425	1.026	1.025	1.026	1.026	1.026	1.023	1.019	1.017	1.015	1.009

Table 3. (Contd.)

λ, Å	B9IV	B6III	B7III	B8III	B9III	A0III	A3III	A5III	A7III	F0III
5475	1.000	1.000	1.000	1.000	1.000	1.000	1.000	1.000	1.000	1.000
5525	0.971	0.974	0.967	0.977	0.976	0.975	0.984	0.979	0.982	0.985
5575	0.951	0.949	0.940	0.953	0.952	0.949	0.966	0.959	0.969	0.978
5625	0.919	0.922	0.916	0.917	0.925	0.921	0.947	0.931	0.941	0.954
5675	0.892	0.899	0.884	0.892	0.898	0.900	0.921	0.917	0.922	0.930
5725	0.878	0.873	0.857	0.873	0.877	0.877	0.908	0.899	0.912	0.922
5775	0.855	0.848	0.837	0.847	0.855	0.855	0.881	0.879	0.897	0.906
5825	0.832	0.832	0.821	0.821	0.832	0.829	0.863	0.865	0.877	0.896
5875	0.811	0.808	0.793	0.801	0.806	0.808	0.839	0.841	0.859	0.883
5925	0.788	0.776	0.766	0.776	0.785	0.783	0.816	0.819	0.846	0.859
5975	0.762	0.760	0.739	0.749	0.763	0.753	0.793	0.796	0.819	0.831
6025	0.738	0.728	0.721	0.727	0.741	0.732	0.774	0.778	0.802	0.815
6075	0.719	0.719	0.698	0.710	0.724	0.708	0.760	0.762	0.782	0.800
6125	0.701	0.688	0.687	0.688	0.705	0.692	0.742	0.746	0.764	0.784
6175	0.678	0.671	0.667	0.672	0.687	0.674	0.725	0.724	0.754	0.765
6225	0.669	0.655	0.650	0.652	0.673	0.656	0.708	0.714	0.735	0.756
6275	0.649	0.636	0.640	0.633	0.650	0.635	0.691	0.697	0.721	0.748
6325	0.633	0.617	0.620	0.619	0.629	0.620	0.676	0.679	0.703	0.726
6375	0.618	0.606	0.606	0.607	0.616	0.610	0.663	0.667	0.698	0.725
6425	0.602	0.589	0.597	0.591	0.597	0.590	0.649	0.653	0.681	0.709
6475	0.584	0.577	0.587	0.580	0.587	0.582	0.637	0.638	0.671	0.700
6525	0.539	0.554	0.548	0.559	0.562	0.549	0.593	0.596	0.646	0.690
6575	0.475	0.499	0.487	0.484	0.494	0.469	0.521	0.522	0.540	0.622
6625	0.562	0.545	0.549	0.553	0.550	0.551	0.607	0.616	0.645	0.677
6675	0.542	0.528	0.536	0.535	0.539	0.541	0.598	0.603	0.632	0.668
6725	0.535	0.510	0.523	0.520	0.528	0.532	0.590	0.595	0.627	0.661
6775	0.519	0.501	0.510	0.506	0.520	0.515	0.579	0.582	0.615	0.660
6825	0.509	0.486	0.499	0.493	0.507	0.496	0.574	0.570	0.602	0.647
6875	0.493	0.472	0.486	0.472	0.501	0.487	0.561	0.555	0.592	0.634
6925	0.488	0.459	0.474	0.469	0.489	0.481	0.555	0.547	0.581	0.630
6975	0.473	0.451	0.463	0.457	0.478	0.469	0.546	0.537	0.573	0.625
7025	0.467	0.437	0.453	0.444	0.471	0.457	0.537	0.528	0.564	0.621
7075	0.456	0.432	0.442	0.432	0.458	0.450	0.524	0.517	0.556	0.603
7125	0.444	0.421	0.433	0.425	0.451	0.439	0.517	0.508	0.545	0.590
7175	0.430	0.414	0.421	0.413	0.442	0.427	0.506	0.497	0.538	0.584
7225	0.425	0.402	0.411	0.406	0.436	0.422	0.499	0.489	0.530	0.577
7275	0.414	0.395	0.401	0.393	0.430	0.414	0.489	0.480	0.522	0.578
7325	0.411	0.386	0.389	0.382	0.419	0.401	0.479	0.468	0.515	0.563
7375	0.410	0.375	0.378	0.372	0.411	0.393	0.466	0.460	0.506	0.562
7425	0.400	0.360	0.365	0.361	0.395	0.384	0.457	0.455	0.497	0.548
7475	0.389	0.351	0.358	0.351	0.390	0.377	0.446	0.442	0.488	0.540
7525	0.378	0.340	0.346	0.338	0.378	0.360	0.437	0.430	0.480	0.528
7575	0.367	0.333	0.340	0.329	0.370	0.353	0.429	0.424	0.472	0.520

Table 4. Standard energy distributions for supergiants

| λ, Å	O9.5Iab	B1Iab	B2Iab	B5Iab	B9Iab	G2Iab	λ, Å	O9.5Iab	B1Iab	B2Iab	B5Iab	B9Iab	G2Iab
3225	5.469	4.310	4.176	2.968	1.832	0.135	5425	1.030	1.028	1.029	1.018	1.020	0.998
3275	5.150	4.155	4.035	2.818	1.779	0.169	5475	1.000	1.000	1.000	1.000	1.000	1.000
3325	4.905	3.980	3.821	2.694	1.753	0.181	5525	0.970	0.970	0.976	0.969	0.976	1.016
3375	4.597	3.808	3.637	2.574	1.696	0.175	5575	0.933	0.952	0.950	0.949	0.951	1.014
3425	4.390	3.632	3.491	2.476	1.656	0.205	5625	0.907	0.919	0.922	0.920	0.930	1.013
3475	4.162	3.463	3.329	2.373	1.604	0.206	5675	0.880	0.879	0.893	0.883	0.911	1.004
3525	4.022	3.347	3.213	2.323	1.580	0.224	5725	0.850	0.855	0.877	0.862	0.891	1.028
3575	3.877	3.250	3.103	2.279	1.568	0.209	5775	0.814	0.833	0.852	0.842	0.875	1.027
3625	3.760	3.121	2.968	2.230	1.557	0.256	5825	0.787	0.807	0.827	0.820	0.857	1.045
3675	3.664	3.064	2.915	2.230	1.654	0.317	5875	0.766	0.782	0.802	0.795	0.841	1.010
3725	3.569	2.913	2.864	2.253	1.913	0.306	5925	0.745	0.762	0.782	0.770	0.817	1.033
3775	3.327	2.880	2.727	2.276	2.038	0.290	5975	0.725	0.736	0.763	0.755	0.793	1.015
3825	3.230	2.884	2.687	2.345	2.074	0.250	6025	0.703	0.713	0.739	0.741	0.768	1.006
3875	2.994	3.065	2.585	2.441	2.127	0.293	6075	0.686	0.691	0.720	0.718	0.749	0.991
3925	2.760	2.803	2.611	2.391	2.083	0.266	6125	0.665	0.675	0.707	0.700	0.739	0.970
3975	2.406	2.572	2.399	2.167	1.943	0.338	6175	0.650	0.654	0.681	0.683	0.719	0.961
4025	2.903	2.757	2.668	2.476	2.329	0.583	6225	0.635	0.638	0.666	0.671	0.705	0.952
4075	2.741	2.537	2.514	2.327	2.172	0.577	6275	0.613	0.621	0.645	0.642	0.692	0.944
4125	2.526	2.452	2.403	2.216	2.039	0.588	6325	0.593	0.604	0.631	0.638	0.672	0.946
4175	2.522	2.408	2.345	2.176	2.039	0.579	6375	0.585	0.597	0.618	0.623	0.665	0.954
4225	2.451	2.352	2.274	2.110	1.998	0.627	6425	0.567	0.582	0.599	0.608	0.650	0.946
4275	2.368	2.246	2.192	2.053	1.934	0.625	6475	0.557	0.571	0.589	0.600	0.638	0.933
4325	2.170	2.030	2.017	1.869	1.831	0.648	6525	0.544	0.556	0.576	0.578	0.628	0.936
4375	2.160	2.046	2.010	1.892	1.790	0.729	6575	0.537	0.527	0.551	0.555	0.612	0.880
4425	2.075	1.964	1.915	1.810	1.757	0.738	6625	0.525	0.542	0.558	0.569	0.602	0.939
4475	2.013	1.894	1.847	1.746	1.705	0.811	6675	0.505	0.512	0.535	0.542	0.587	0.940
4525	1.919	1.836	1.794	1.697	1.656	0.828	6725	0.492	0.507	0.523	0.537	0.580	0.933
4575	1.858	1.748	1.711	1.646	1.606	0.841	6775	0.478	0.495	0.508	0.526	0.573	0.929
4625	1.776	1.687	1.668	1.590	1.581	0.907	6825	0.463	0.478	0.499	0.514	0.566	0.922
4675	1.719	1.644	1.612	1.543	1.526	0.878	6875	0.453	0.464	0.483	0.501	0.555	0.903
4725	1.633	1.585	1.556	1.496	1.473	0.923	6925	0.451	0.455	0.475	0.493	0.545	0.902
4775	1.551	1.533	1.507	1.449	1.416	0.956	6975	0.433	0.446	0.463	0.480	0.538	0.883
4825	1.470	1.495	1.448	1.395	1.362	0.972	7025	0.415	0.439	0.455	0.471	0.531	0.874
4875	1.379	1.400	1.364	1.319	1.195	0.888	7075	0.405	0.428	0.439	0.452	0.522	0.871
4925	1.378	1.417	1.370	1.341	1.275	0.969	7125	0.402	0.416	0.430	0.441	0.508	0.858
4975	1.355	1.359	1.322	1.283	1.268	0.942	7175	0.390	0.404	0.419	0.438	0.499	0.852
5025	1.302	1.301	1.265	1.225	1.241	0.923	7225	0.381	0.397	0.407	0.428	0.490	0.844
5075	1.279	1.272	1.238	1.206	1.209	0.961	7275	0.371	0.388	0.401	0.420	0.482	0.832
5125	1.232	1.231	1.201	1.180	1.177	0.931	7325	0.361	0.379	0.389	0.403	0.473	0.818
5175	1.197	1.197	1.169	1.151	1.150	0.907	7375	0.351	0.368	0.380	0.391	0.463	0.813
5225	1.157	1.160	1.134	1.125	1.118	0.936	7425	0.342	0.357	0.372	0.381	0.451	0.804
5275	1.121	1.127	1.106	1.097	1.094	0.957	7475	0.332	0.347	0.363	0.373	0.441	0.795
5325	1.088	1.088	1.081	1.069	1.062	0.990	7525	0.321	0.337	0.353	0.361	0.432	0.777
5375	1.056	1.061	1.046	1.051	1.041	1.005	7575	0.301	0.329	0.345	0.352	0.425	0.762
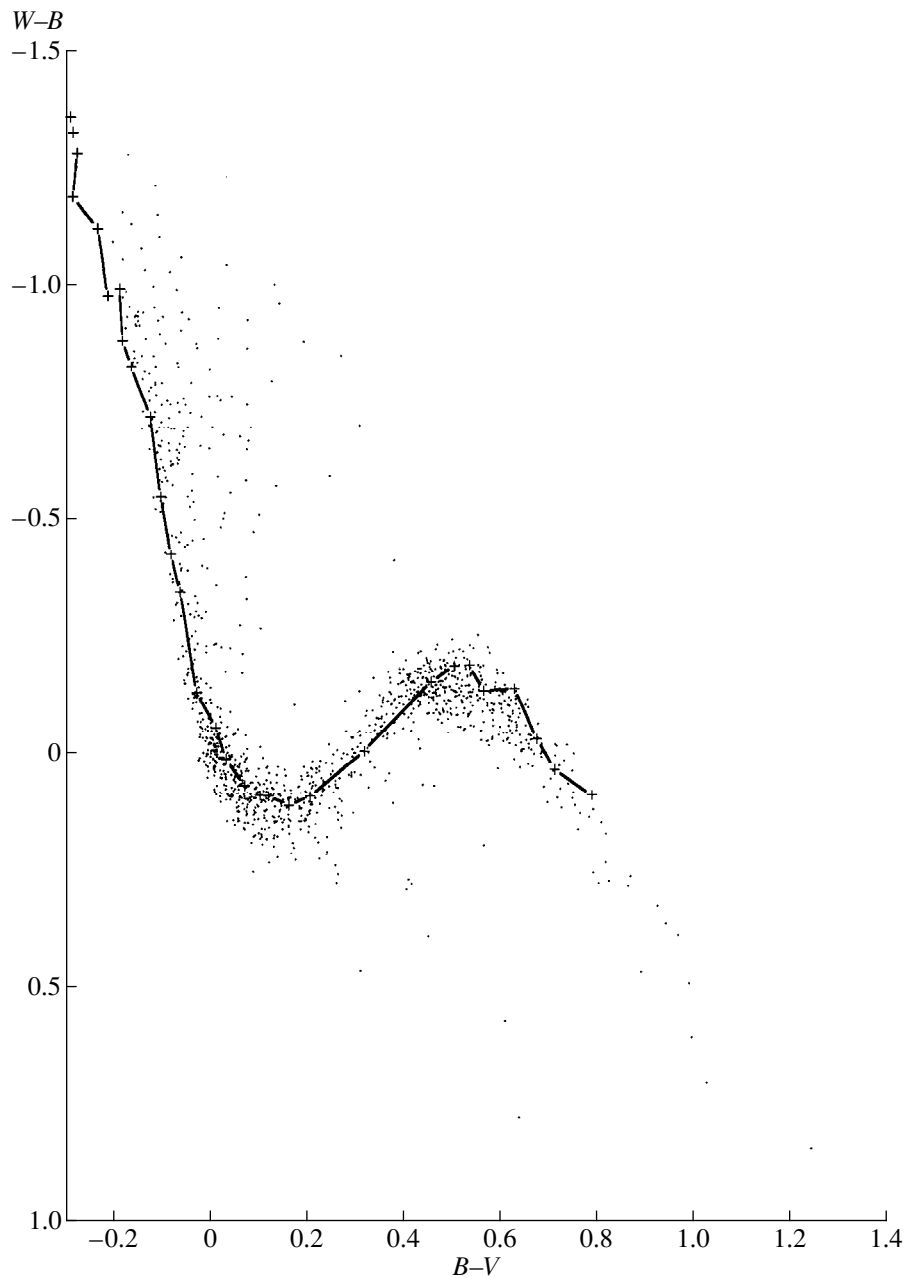
Fig. 1. Two-color (*W–B*)–(*B–V*) diagram (*WBVR* system) for main-sequence stars. The points are observational data from the catalog [20] and the crosses correspond to the computed normal color indices.

type by convolving the normal distributions with the response curves of the *WBVR* [20] and Vilnius [21] photometric systems, which have been determined rather accurately. We concluded earlier [22] that it is possible to obtain an accuracy in the computed stellar color indices comparable to the observational accuracy if the response curves for the photometric systems are reliably determined, the energy distributions for the program stars are accurate to 2% or better, and there are trustworthy data on the energy distribution in the integrated stellar spectrum, which determines the zero

point of the computed color indices. We have computed the normal color indices for main-sequence stars, subgiants, and B–F giants; our data on the normal distributions of late giants begin only from λ3425 Å.

Since the normal color indices in the Vilnius photometric system were derived from photometric observations [18], we obtained mean differences between these and the normal indices computed from the mean energy distribution for each of the studied spectral subtypes. An analysis of these differences demonstrates the absence of substantial systematic errors. For all spectral

Table 5. Normal color indices of stars in the *WBVR* system

Sp	*B–V*	*W–B*	Sp	*B–V*	*W–B*	Sp	*B–V*	*W–B*
O9V	−0.295	−1.356	G2V	0.663	−0.025	B0III	−0.269	−1.351
O9.5V	−0.290	−1.320	G5V	0.700	0.039	B1III	−0.244	−1.195
B0.5IV, V	−0.282	−1.277	G8V	0.777	0.093	B2III	−0.219	−1.048
B1V	−0.290	−1.184	B2IV	−0.205	−1.026	B3III	−0.194	−0.909
B1.5V	−0.239	−1.116	B3IV	−0.188	−0.918	B4III	−0.169	−0.778
B2V	−0.219	−0.973	B4IV	−0.169	−0.802	B5III	−0.143	−0.655
B2IV–V	−0.194	−0.987	B5IV	−0.148	−0.681	B6III	−0.117	−0.540
B2.5V	−0.189	−0.878	B6IV	−0.124	−0.560	B7III	−0.091	−0.434
B3V	−0.171	−0.823	B7IV	−0.098	−0.442	B8III	−0.065	−0.336
B5V	−0.132	−0.715	B8IV	−0.070	−0.331	B9III	−0.038	−0.246
B7V	−0.112	−0.542	B9IV	−0.041	−0.227	A0III	−0.011	−0.164
B8V	−0.091	−0.420	A0IV	−0.011	−0.135	A1III	0.016	−0.091
B9V	−0.073	−0.339	A1IV	0.021	−0.055	A2III	0.043	−0.026
B9.5V	−0.040	−0.125	A2IV	0.053	0.011	A3III	0.071	0.031
A0V	−0.001	−0.049	A3IV	0.086	0.063	A4III	0.099	0.080
A1V	0.021	0.018	A4IV	0.118	0.100	A5III	0.127	0.121
A2V	0.059	0.073	A5IV	0.151	0.122	A6III	0.156	0.153
A3V	0.090	0.094	A6IV	0.184	0.130	A7III	0.184	0.177
A4V	0.108	0.095	A7IV	0.216	0.125	A8III	0.213	0.193
A5V	0.150	0.115	A8IV	0.247	0.109	A9III	0.242	0.200
A7V	0.194	0.095	A9IV	0.277	0.082	F0III	0.272	0.200
F0V	0.306	0.001	F0IV	0.306	0.048	O9.5Iab	−0.212	−1.339
F5V	0.445	−0.148	F1IV	0.334	0.009	B1Iab	−0.164	−1.179
F6V	0.493	−0.181	F2IV	0.360	−0.032	B2Iab	−0.134	−1.167
F7V	0.524	−0.183	F3IV	0.383	−0.070	B5Iab	−0.074	−0.912
F8V	0.553	−0.129	F4IV	0.405	−0.103	B9Iab	−0.006	−0.603
G0V	0.617	−0.133	F5IV	0.423	−0.126	G2Iab	0.997	0.536

subtypes, the largest deviations occur for *U–P*, *P–X*, and *V–S* and are about 0.03^m; the deviations for *X–Y*, *Y–Z*, and *Z–V* are no more than 0.01^m to 0.02^m, which do not exceed the uncertainties in the spectrophotometric data and normal color indices [18].

Since normal indices have not derived from photometric observations in the *WBVR* system [20], we plotted the (*W–B*)–(*B–V*) two-color diagrams using the observational data, then superimposed the computed normal color indices for the main-sequence stars and early-type giants separately (Figs. 1, 2, respectively).

Figures 1 and 2 show that our computed color indices reproduce both the main sequence and the sequence of early giants well, testifying to the reliability of our normal energy distributions for these subtypes.

As a by-product of our analysis, we determined normal color indices in the *WBVR* system; these may become useful in the future, when observations in this system are extended toward fainter stars. With this in mind, we plotted the computed color indices as functions of the spectral type. After smoothing this plot, we were able to predict color indices for subtypes not
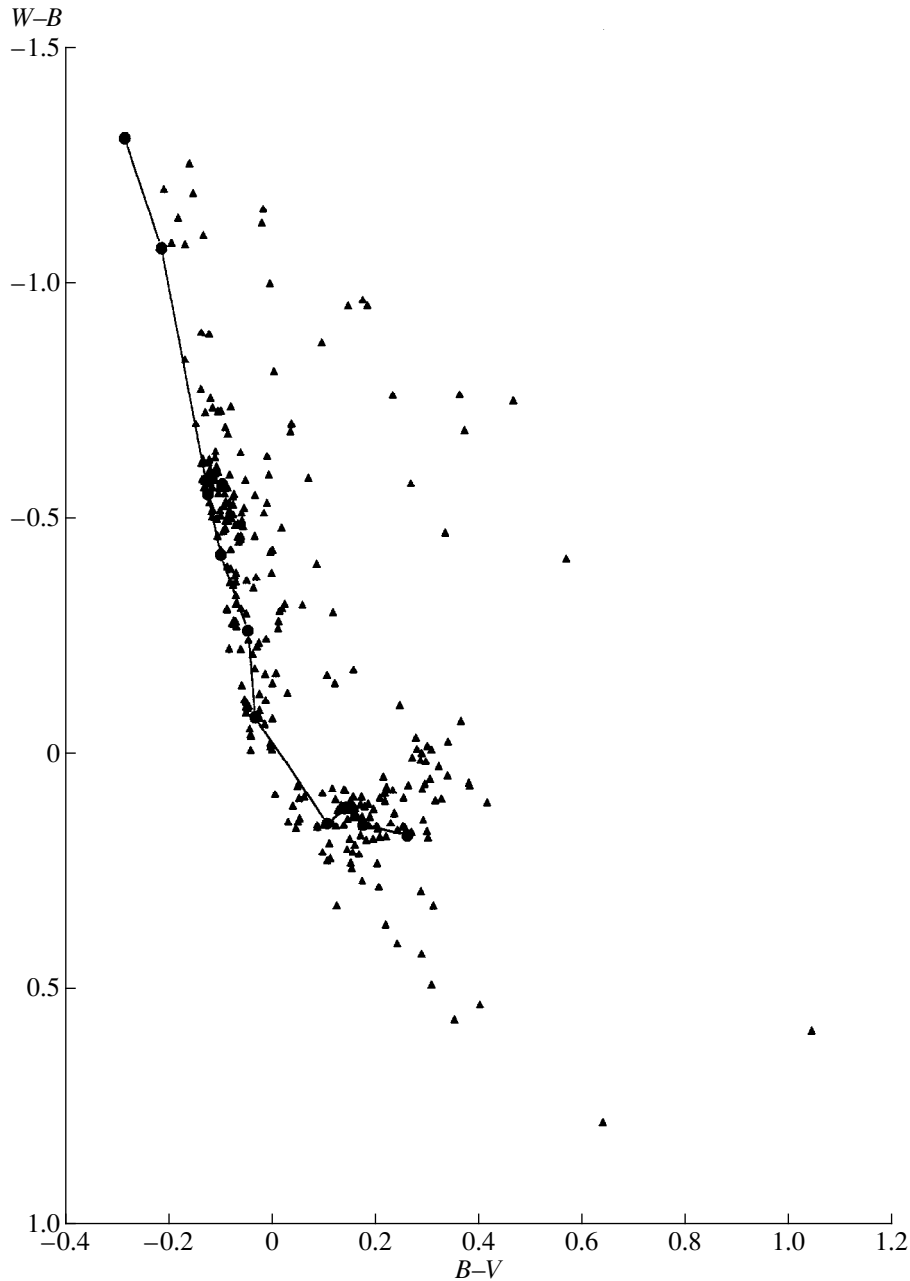
Fig. 2. Two-color (W–B)–(B–V) diagram (*WBVR* system) for early giants. The triangles are observational data from the catalog [20] and the filled circles correspond to the computed normal color indices.

included in our computations due to the lack of normal distributions. We carried out this procedure for both subgiants and giants. Table 5 presents the final computed $(W–B)_0$ and $(B–V)_0$ values.

3. CONCLUSIONS

Our study has yielded the following results.

(1) We have determined the normal energy distributions for early giants and supergiants of 15 spectral subtypes.

(2) Color indices in the Vilnius photometric system computed using our derived normal distributions for each of the spectral subtypes are in good agreement with the normal colors determined from photometric observations. Since these two types of normal color indices are based on different kinds of observations and are derived completely independently, this agreement testifies to the trustworthiness of our energy distributions and demonstrates that they can be used to determine the normal color indices for photometric systems for which such indices are not yet available.

(3) The reliability of our normal distributions is confirmed by the location of *WBVR* color indices computed using these curves in two-color diagrams plotted for *WBVR* observations of the stars.

(4) We have derived the $(W–B)_0$ and $(B–V)_0$ normal color indices for the *WBVR* system.

REFERENCES

1. L. N. Knyazeva and A. V. Kharitonov, Astron. Zh. **70**, 760 (1993) [Astron. Rep. **37**, 382 (1993)].

2. L. N. Knyazeva and A. V. Kharitonov, Astron. Zh. **71**, 264 (1994) [Astron. Rep. **38**, 231 (1994)].

3. L. N. Knyazeva and A. V. Kharitonov, Astron. Zh. **71**, 458 (1994) [Astron. Rep. **38**, 400 (1994)].

4. L. N. Knyazeva and A. V. Kharitonov, Astron. Zh. **73**, 67 (1996) [Astron. Rep. **40**, 57 (1996)].

5. L. N. Knyazeva and A. V. Kharitonov, Astron. Zh. **73**, 906 (1996) [Astron. Rep. **40**, 823 (1996)].

6. L. N. Knyazeva and A. V. Kharitonov, Astron. Zh. **75**, 70 (1998) [Astron. Rep. **42**, 60 (1998)].

7. L. N. Knyazeva and A. V. Kharitonov, Astron. Zh. **75**, 197 (1998) [Astron. Rep. **42**, 169 (1998)].

8. Z. Sviderskene, Byull. Vilnius Astron. Obs., No. 80, 3 (1988).

9. A. V. Kharitonov, V. M. Tereshchenko, and L. N. Knyazeva, *Spectrophotometric Catalog of Stars* [in Russian] (Nauka Kaz. SSR, Alma-Ata, 1988).

10. *Spectrophotometry of Bright Stars* [in Russian], Ed. by I. N. Glushnev (Nauka, Moscow, 1982).

11. G. A. Alekseeva, A. A. Arkharov, V. D. Galkin, *et al.*, Balt. Astron. **5**, 603 (1996).

12. A. V. Kharitonov, V. M. Tereshchenko, L. N. Knyazeva, *et al.*, Balt. Astron. **6**, 585 (1997).

13. D. Hoffleit, *The Bright Star Catalogue*, 5th ed. (Yale Univ. Observatory, CDS, Strasbourg, 1991).

14. A. Hirshfeld and R. W. Sinnott, *Sky Catalogue 2000.0* (Cambridge (MA), 1982).

15. A. D. Code and M. R. Meade, Astrophys. J., Suppl. Ser. **39** (1979).

16. Jamar *et al.*, in *Ultraviolet Bright-Star Spectrophotometric Catalogue* (1976).

17. A. Heck, D. Egret, M. Jaschek, and C. Jaschek, *IUE Low-Dispersion Spectra Reference Atlas. Part 1: Normal Stars. ESA SP–1052* (ESA, Paris).

18. V. Straizys, *Multicolor Stellar Photometry* (Phachart Publishing Hause, Tucson, 1992).

19. D. S. Hayes, *IAU Symp. 111: Calibration of Fundamental Stellar Quantities*, Ed. by D. S. Hayes *et al.* (Reidel, Dordrecht, 1985), p. 225.

20. V. G. Kornilov, I. M. Volkov, A. I. Zakharov, *et al.*, Tr. Gos. Astron. Inst., Mosk. Gos. Univ. **63**, 5 (1991).

21. V. Straizys and A. Kazlauskas, Balt. Astron. **2**, 1 (1993).

22. L. N. Knyazeva and A. V. Kharitonov, Astron. Zh., 2000 (in press) [Astron. Rep., 2000 (in press)].

Translated by N. Samus'

Non-LTE Analysis of the Formation of EuII Lines in the Atmospheres of Solar-type Stars

L. I. Mashonkina

Kazan State University, ul. Lenina 416, Kazan, 420111 Tatarstan, Russia
Received July 12, 1999

Abstract—A method to analyze the statistical equilibrium of the EuII ion based on a 36-level model atom has been developed. The formation of EuII lines without assuming local thermodynamic equilibrium (LTE) is considered for $T_{eff} = 5500$–7000 K, $\log g = 4.0$, and metallicities [A] from 0 to –1.5. Non-LTE effects in the level populations are primarily due to radiative pumping of excited states from the ground and low-lying levels, which leads to over-population of upper relative to lower levels. As a result, the studied λ4129 and λ6645 Å lines are weaker than in the LTE case. However, due to the small energy differences between even low-lying EuII levels, collisional coupling is strong, and deviations from LTE in EuII lines are modest: for the Sun, non-LTE corrections to the abundance are only 0.04 dex. The non-LTE effects grow with an increase in the effective temperature and with a decrease in the metallicity, so that non-LTE abundance corrections can reach 0.12 dex for $T_{eff} = 5500$K, $\log g = 4.0$, [A] = –1.5 and 0.1 dex for $T_{eff} = 7000$K, $\log g = 4.0$, [A] = 0. The effect of inaccuracy in the atomic parameters for EuII on the non-LTE calculations is examined. Analysis of the profiles of the solar EuII λ4129 and λ6645 Å lines is used to empirically refine estimates of the efficiency of collisional processes in forbidden transitions in establishing the distribution of EuII ions over excited states. © 2000 MAIK "Nauka/Interperiodica".

1. INTRODUCTION

This paper continues our earlier studies [1, 2] of the abundances of heavy elements synthesized in neutron-capture processes in low-mass stars ($M \leq M_\odot$) in the disk and halo of the Galaxy. Such stars provide a key to understanding the chemical evolution of the Galaxy. They evolve slowly, so that they include both very old objects whose ages are comparable with the age of the Galaxy (halo G subdwarfs) and stars that formed at appreciably later epochs. At the same time, if their mass is lower than a solar mass, even the oldest objects are still at the stage of core hydrogen burning, when the products of thermonuclear synthesis are not carried to the surface, so that the chemical composition of their atmospheres reflects the chemical composition of the interstellar medium from which they formed.

Depending on the flux density of neutrons, neutron-capture processes are divided into slow and fast neutron capture (the *s* process and *r* process, respectively). The *r* process is associated with the explosions of massive type-II supernovae, since a large flux density of neutrons is provided in this case. The *s* process can occur in stars of moderate mass (2–4 $M_\odot$) at the stage of steady-state double-layer burning and also in the cores of massive stars ($M \sim 20 M_\odot$) at the helium-burning stage [3]. The roles of the *s* and *r* processes in the synthesis of heavy elements with $Z > 26$ are different. The *s* process can form elements up to bismuth ($Z = 83$), dominated by the even isotopes of these elements. The *r* process plays the leading role in the formation of odd

isotopes with $Z \leq 83$ and is also responsible for the formation of heavier elements with $Z > 83$.

Theoretical estimates of the rates of synthesis of various isotopes in *s* and *r* processes and analyses of the isotopic composition of material in the solar system [4] have shown, for example, that the *s* process dominated in the synthesis of Sr ($s : r = 92 : 8$) and Ba ($s : r = 88 : 12$), the *r* process dominated in the synthesis of Eu ($s : r = 9 : 91$), and the roles of these two processes were comparable in the synthesis of a number of other elements, such as Y ($s : r = 73 : 27$) and Zr ($s : r = 79 : 21$). Here, $s : r$ is the ratio of the contributions of the *s* and *r* processes. The solar-system material reflects the contributions of these two processes summed from the first epochs of star formation to the time of the Sun's birth. But were their relative contributions the same at earlier epochs? The answer to this question will provide information about the relative rates of formation of stars of moderate mass, in which the *s* process dominates, and of massive stars, in which the *r* process dominates.

Our earlier study [2] was concerned with determining the abundance of barium in low-mass stars—an element synthesized primarily via the *s* process. A logical continuation of this work is an analysis of abundances of *r*-process elements. This was precisely why we chose europium for this study—it is the most widespread of *r*-process elements: $\log \varepsilon_{Eu} = 0.51$ for the Sun, and the meteoritic abundance is 0.54 [5]. Here, we have used an abundance scale in which $\log \varepsilon_H = 12$. Eu is singly ionized in the atmospheres of solar-type stars,
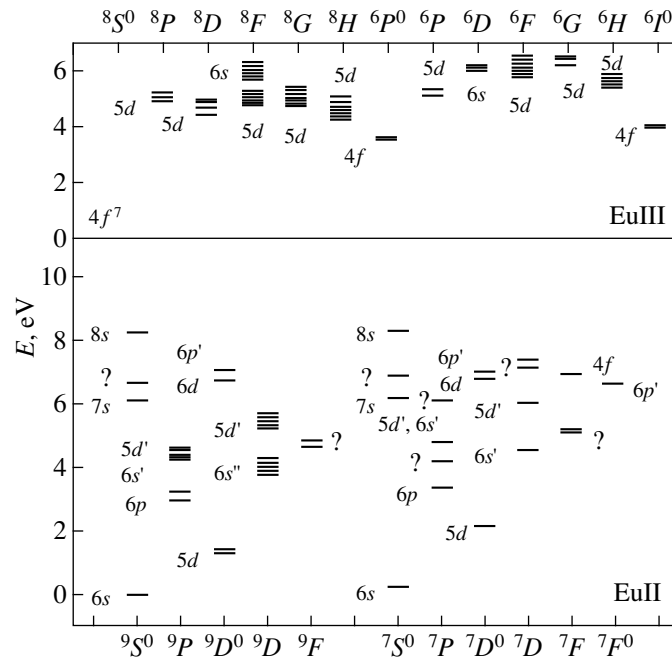
Fig. 1. Grotrian diagram for EuII and EuIII constructed using the data of [7]. The fine-splitting sublevels with close energies are shown as a single level.

and the EuII λ4129 Å resonance line is observed in stars with a fairly wide range of metallicities, up to [Fe/H] = –2 [6]. Our goal here was to develop a method for computing the statistical equilibrium of EuII and to analyze the formation of spectral lines of EuII in the atmospheres of solar-type stars without assuming LTE. This is the first time such a non-LTE analysis has been performed for EuII, and accordingly we describe in some detail the atomic model (Section 2), mechanisms for deviations from LTE in the populations of the atomic levels (Section 4), and the influence of uncertainties in the atomic parameters on the results (Section 5). Section 3 describes our computation method. The final section of the paper presents our results: analysis of the profiles of EuII lines in the spectrum of the Sun and theoretical non-LTE corrections to Eu abundances for effective temperatures T_{eff} = 5500–7000 K, surface gravity $\log g$ = 4.0, and heavy-element abundances [A] from –1.5 to 0. In future work, these results will be used in the analysis of stellar spectra.

2. MODEL FOR THE ATOM AND ATOMIC DATA

The ground state of EuII has the electronic configuration $4f^7 6s$, and states with a single excited electron have the configuration $4f^7 nl$. We will denote these excited states nl, where nl can be $4f$; $5d, f, g$; $6p, d, \ldots$; $7s, p, \ldots$; and so on. Each such configuration, except for $4f^8$, corresponds to two terms with the same orbital quantum number and spin numbers S = 3 and 4. For EuII, the probability of a transition between terms with different multiplicities is virtually the same as that for single-configuration transitions. Therefore, we consider

jointly the ^9L and ^7L systems of atomic levels. The energy levels for EuII, and also for EuIII and EuI, which will be considered below, were taken from [7] and are experimental values. Data are available for levels of EuII with excitation energies $E_i <$ 8.3 eV for nl = 5d, 6p, 7s, 6d, 4f, and 8s, as well as for a number of doubly excited states. However, in this last case, the electronic configurations and terms have been conclusively identified only for $4f^6 5dnl$ configurations, namely for

$4f^6 5d^2$ (further, 5d') terms ^9P, ^9D, ^7P;

$4f^6 5d6s$ (further, 6s') terms ^9P, ^9D, ^7P, ^7D;

$4f^6 5d6p$ (further, 6p') terms $^7D^0$, $^7F^0$.

For 83 other levels, in addition to the energy, only the total orbital angular momentum and parity are determined. Guided by the mutual positions of known terms of the 6s' configuration, we distinguished in the list of levels five candidate fine-structure sublevels of the missing ^7D term of the 5d' configuration and five candidate sublevels of the 6p' $^9D^°$ term. We were not able to identify sublevels of the missing 6p' $^9F^0$ term. We also distinguished ten terms that cannot correspond to the $4f^7 nl$ and $4f^6 5dnl$ configurations. Since the probabilities for transitions between these levels of unknown configurations and the $4f^7 nl$ sublevels are known, they were included in the model for the EuII atom. We took into account the remaining 27 levels with E_i from 5 to 7.4 eV only in the equation for conservation of particle number.

Figure 1 shows a Grotrian diagram for EuII terms known and identified by us (the latter is indicated by a question mark) and low levels of EuIII. When composing the EuII-atom model, we merged levels with nearby

Table 1. Model EuII atom

no.	Term	J	ν_{ion}, 10^{15} s^{-1}	no.	Term	J	ν_{ion}, 10^{15} s^{-1}
1	$6s^9S^0$	4	2.718069	20	$5d'^7D$	1–5	2.412452
2	$6s^7S^0$	3	2.668028	21	$?^7P$	2–4	2.397835
3	$5d^9D^0$	2–4	2.415104	22	$7s^9S^0$	4	1.245248
4	$5d^9D^0$	5, 6	2.391720	23	$7s^7S^0$	3	1.229701
5	$5d^7D^0$	1–5	2.204957	24	$6p'^7F^0$	0–6	2.266505
6	$6p^9P$	3, 4	1.998835	25	$?^9S^0$	4	2.254014
7	$6p^9P$	5	1.933427	26	$6d^9D^0$	2–6	1.086409
8	$6p^7P$	2–4	1.906641		$6d^7D^0$	1–5	
9	$6s'^9P$	2–6	2.892894	27	$?^7S^{\circ}$	3	2.200771
10	$?^7P$	2–4	2.850650	28	$4f^7F$	0–6	1.041023
	$6s'^9P$	3–5		29	$6p'^7D^0$	1–5	2.169544
11	$?^9P$	3, 4	2.810273		$6p'^9D^0$	2–5	
	$?^9P$	3, 4		30	$?^7D$	1–4	2.144068
12	$6s'^7D$	1–5	2.766894	31	$?^7D$	1–4	2.083981
13	$5d'^9P$	3–5	2.750150	32	$8s^9S^0$	4	0.7179409
14	$?^9F$	2–6	2.740683		$8s^7S^0$	3	
15	$6s'^7P$	2–4	2.705547	33	EuIII	7/2	0.0000000
	$5d'^7P$	2–4		34	$5d^8H$	3/2–17/2	–1.102901
16	$?^9F$	1–7	2.694816	35	$5d^8D$	3/2–11/2	–1.148320
17	$?^7F$	4, 6	2.639528		$5d^8G$	1/2–15/2	
	$?^7F$	4–6		36	$5d^8F$	3/2–13/2	–1.228077
18	$5d^9D$	2–5	2.556036		$5d^8P$	5/2–9/2	
19	$5d^9D$	6	2.486469		$5d^6P$	3/2–7/2	

energies. This is reflected in Table 1, which lists for each level in the model atom the EuII levels that were included in that level. We obtained the threshold ionization frequencies ν_{ion} by averaging over the individual levels. The $4f^7 {}^8S^0$ ground state, to which there is ionization from the nl levels of EuII, and the excited levels of the $4f^6 5d$ configuration, to which there is ionization from the nl' levels of EuII, are important for the non-LTE solution for EuIII.

Since the $5d$ EuIII levels have nearby energies (Fig. 1), we have grouped them into three levels in the model atom (Table 1). The populations of these levels can be taken to be in equilibrium relative to the EuIII ground state, since radiative transitions from the ground state to the $5d$ states are in the ultraviolet part of the spectrum, with $\lambda < 1800$ Å, where the flux of solar-type stars is very weak.

Our final model for the atom, shown in Fig. 2, includes 32 levels of EuII and four of EuIII. The equation for the conservation of particle number also takes into account eight low terms of EuI and 12 terms of EuIII. In the atmospheres of solar-type stars, the number density n (EuI) does not exceed $10^{-4} n$ (EuII), so that no processes in the EuI atom can realistically influence the populations of the EuII levels.

We took the oscillator strengths f_{ij} from the VALD database [8], which for EuII includes the $\log gf$ from [9, 10]. We compared them for common transitions. The difference was small and did not exceed 10%. When possible, we gave preference to the new data of [9]. The list [10] is the most complete but also includes far from all transitions for EuII, even among permitted transitions.

Fortunately, there are data for all permitted and intercombinational transitions from levels 1 and 2 (level numbers correspond to those in Table 1) to higher levels; for virtually all transitions upward from levels 3, 4, and 6–8; and for all important transitions from level 5. As we will show below, deviations from LTE in EuII in the atmospheres of solar-type stars are associated precisely with this group of transitions. The availability of oscillator strengths for these transitions provides the fundamental possibility of finding a non-LTE solution for EuII, in spite of large uncertainties in other atomic parameters. Of all transitions playing an important role in deviations of level populations from their equilibrium values, f_{ij} values are missing only for $6p^9P–8s^9S^0$ and $6p^7P–8s^7S^0$; these were specified to be a factor of five smaller than the f_{ij} for transitions in the same series

but lower in energy, $6p$–$7s$. We specified the f_{ij} values for the remaining permitted transitions as follows:

(a) the known oscillator strengths for the $6s$ – $6p$ and $5d$–$6p$ transitions were assigned to the corresponding $6s'$–$6p'$ and $5d'$–$6p'$ transitions;

(b) we assumed $f_{ij} = 0.001$ for transitions between nl' levels and levels of unknown configurations 10, 14, 16, 17, 21, 25, 27, 30, and 31;

(c) we assumed $f_{ij} = 0.001$ for transitions between doubly excited and singly excited states;

(d) the value $f_{ij} = 0.1$ was specified for the $6d$–$4f$ transition, which is half the known value of f_{ij} for the $5d$–$4f$ transition.

The known energies for the ns and nd levels made it possible to apply the method of quantum defects to calculate the photoionization cross sections for the $6p$ levels. When doing this, we used the tables of Peach [11]. The photoionization cross sections for the remaining levels are hydrogen-like. Collisions with electrons were taken into account using the formula of van Regemorter [12] for permitted transitions, the formula of Allen [13] with the line strength $\Omega = 1$ for the forbidden transitions, and the formula of Drawin [14] for ionization. For permitted transitions between nearby levels ($\Delta E <$ 0.1 eV), we used the formula of Vainshtein *et al.* [15]. We also took into account collisional excitation and ionization by neutral hydrogen atoms: in accordance with the formulas of Steenbock and Holweger [16] for permitted transitions and ionization and of Takeda [17] for forbidden transitions.

3. COMPUTATION METHOD

The computations were carried out using the NONLTE3 code [18], which is based on the complete-linearization method of Auer and Heasley [19]. In the opacity computations, in addition to the traditionally included contributions of HI, H⁻, H_2^+, and electron and Rayleigh scattering, we allowed for absorption in bound–free (b–f) transitions of neutral atoms and the first ions of abundant heavy elements (for more details, see [20]), absorption in the molecular bands of the 11 most abundant molecules, and absorption in quasi-molecules of hydrogen, in accordance with the treatment of Doyle [21]. The contribution to the opacity of lines of hydrogen and of heavy elements is taken into account directly, via summation of the absorption coefficients in individual lines. The line list was composed by Kurucz [10] and contains 154070 lines of all elements with $Z \le 60$ in the first three ionization stages from 912–100000 Å.

In our computations, we assumed the line to have a Voigt profile with a decay constant corresponding to natural decay (γ_R equal to the classical value). We assumed that the line width was determined by the action of van der Waals forces; γ_6 was calculated using the formula of Gray [22].
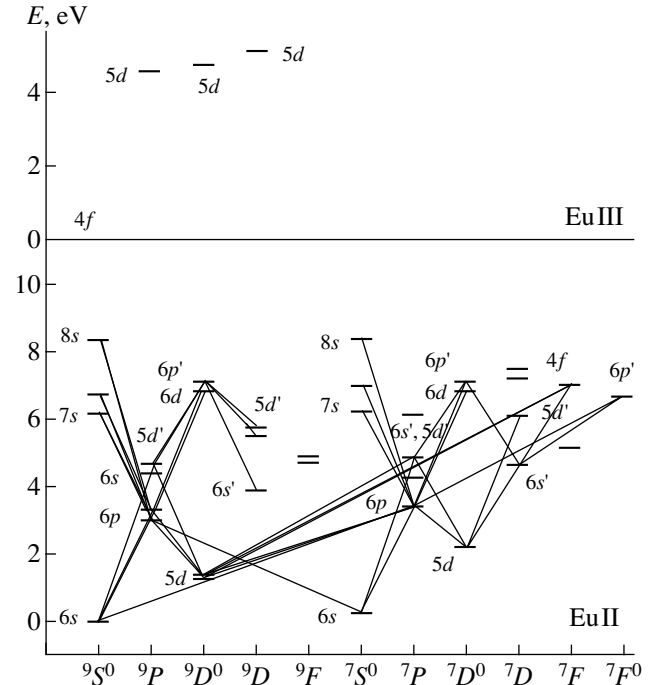

Fig. 2. A model EuII atom. The solid lines show linearized transitions.

Only two lines of EuII are used in the analysis of solar and stellar spectra: the $\lambda4129.7$ Å resonance line ($6s^9S_4^0$–$6p^9P_4$) and the $\lambda6645.11$ Å subordinate line ($5d^9D_6^0$–$6p^9P_5$). Fourteen additional EuII lines can be measured at 3800–10165 Å, but our analysis of the solar spectrum [23] and computations of synthetic spectra indicate that they are so strongly blended that they are not useful for europium abundance determinations.

Europium is a mixture of the two isotopes with odd mass numbers ¹⁵¹Eu and ¹⁵³Eu, each of which has fine structure in its levels. Any spectral line of EuII consists of a set of components forming in transitions between fine-structure sublevels of ions of the ¹⁵¹Eu and ¹⁵³Eu isotopes. The isotopic mixture is 26 mÅ for the $\lambda4129$ Å line and 21 mÅ for the $\lambda6645$ Å line [24]. The effect of hyperfine splitting was significant: a line of each of the isotopes consists of 15 components, with a maximum subdivision of components 170 mÅ for the resonance line and 90 mÅ for the subordinate line. The wavelengths of individual components and their relative intensities derived from the relative abundances of the isotopes $n(^{151}\text{Eu}) : n(^{153}\text{Eu}) = 47.8 : 52.2$ [5] are presented in [24]. For the $\lambda6645$ Å line, we merged components with nearby wavelengths, differing by no more than 5 mÅ. In this way, we obtained a ten-component model, which we used when computing the theoretical line profiles. For the $\lambda4129$ Å line, we used the 12-component model composed by Steffen [25], also on the basis of the data of [24]. Table 2 presents the line wave-
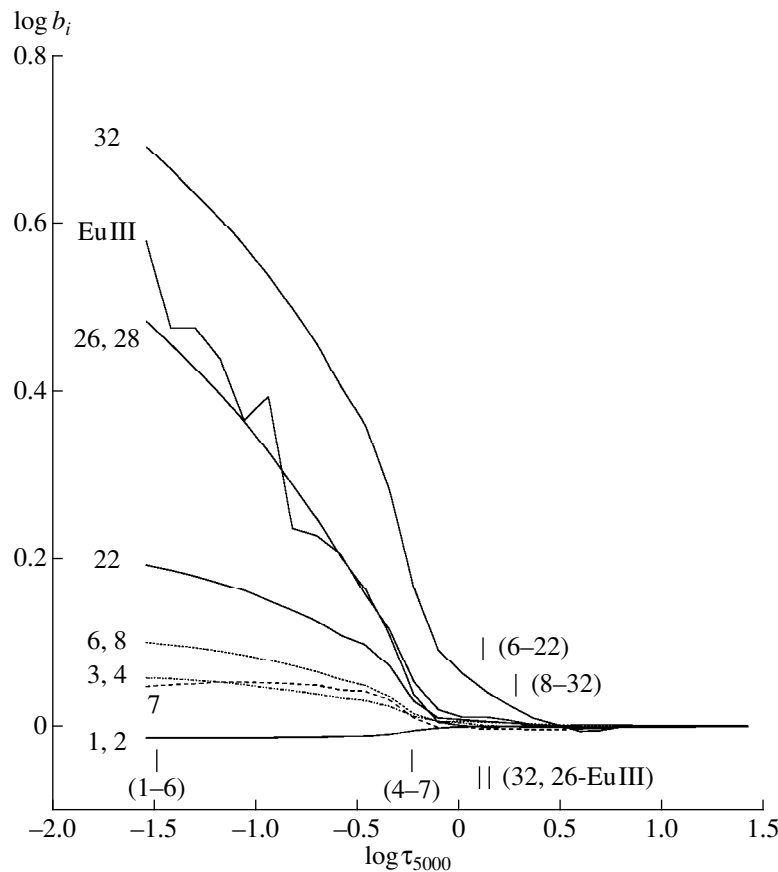
Fig. 3. Behavior of the b factors for individual EuII levels in the solar atmosphere. The level numbers are those from Table 1. The vertical markers indicate the depths of radiation in the cores of important spectral lines and above the ionization thresholds of important continua.

lengths and oscillator strengths. We carried out the computations for Kurucz [10] model atmospheres, kindly provided by the author.

4. MECHANISM FOR DEVIATIONS FROM LTE

Since EuII is the dominating stage of ionization in the atmospheres of stars with $T_{eff} < 7500$ K, deviations from LTE in the level populations arise primarily due to radiative pumping from the ground and low excited states. These deviations are usually characterized by b factors: $b_i = n_i/n_i^*$, where n_i and n_i^* is the population of level i calculated using a non-LTE approach in the Boltzmann–Saha formulas. Figure 3 presents the behavior of the b factors with varying optical depth in the solar atmosphere for those EuII levels that play an important role in deviations from LTE.

In deep layers with $\log \tau_{5000} > 0.4$, there is a detailed balance in all transitions, and $b_i = 1$ for all levels. The first level to begin to experience deviations from LTE is $8s$, due to photoexcitation (radiative pumping) from the $6p^7P$ level in layers where the radiation associated with this transition is generated ($\log \tau_{5000} \leq 0.25$). We will

take "thick" radiation at wavelength λ to mean line generation at a depth where $\tau_\lambda = 1$. In regions with $\log \tau_{5000} = 0\text{--}0.25$, there is radiative pumping of highly excited $6d$, $7s$, $8s$, and other levels in transitions from the $6p^7P$ and $6p^9P$ levels; the population of the $6p$ levels remains essentially in equilibrium due to the detailed balance in transitions coupling them to the ground state.

Above $\log \tau_{5000} = 0$, photons begin to go into the wings of the $\lambda\lambda 4129$, 4205 Å ($6s^9S^0 - 6p^9P$) and $\lambda\lambda 3907$, 3930, 3972 Å ($6s^7S^0 - 6p^7P$) resonance lines, and photo-excitation leads to over-population of the $6p$ levels. The metastable $5d^9D^0$ and $^7D^0$ levels have b factors close to unity in deep layers with $\log \tau_{5000} > -0.15$, due to strong collisional coupling with the ground state; their excitation energies are 1.3 and 2.1 eV, respectively. Higher, however, the medium becomes transparent to radiation in $5d - 6p$ transitions, and spontaneous $6p \longrightarrow 5d$ transitions overpopulate the $5d$ levels.

Overpopulation of the continuum begins in deep layers, due to photoionization from the $6d$ ($\lambda_{thr} \simeq 2760$ Å) and $8s$ ($\lambda_{thr} \simeq 4175$ Å) levels; radiation above the ion-

ization thresholds is generated near $\log \tau_{5000} = 0.15$ and 0.1, respectively. Overpopulation of EuIII is enhanced in higher layers, where photoionization from the $4f$ ($\lambda_{thr} \simeq 2880$ Å) and $7s$ ($\lambda_{thr} \simeq 2430$ Å) levels is added. Photoionization from the $6s$, $5d$, and $6p$ levels ($\lambda_{thr} = 1103$, 1360, and 1572 Å, respectively) plays virtually no role in the region of formation of the EuII lines, since radiation above the ionization thresholds of these levels is generated in surface layers with $\log \tau_{5000} \leq -3$.

Thus, this analysis of various processes overpopulating and depopulating the EuII levels leads us to two important practical conclusions.

(1) The lines under study are generated in transitions between the $6s$, $5d$, and $6p$ levels. In these levels, deviations from LTE in the region where these lines are formed are primarily associated with the disruption of the detailed balance in transitions between these levels and also in transitions to levels of the nl configuration. b–f transitions from the $6s \longrightarrow 6p \longrightarrow 7s$, $6d$, $4f$, and $8s \longrightarrow$ EuIII levels are also important links in the chain of EuIII processes $7s$, $6d$, $4f$, $8s$ overpopulating EuIII levels. Consequently, it is very important to accurately calculate the radiative and collisional rates precisely for these $b-b$ and $b-f$ transitions. With this in mind, we carried out test computations to estimate the influence of inaccuracy in the EuII atomic parameters on the results. The results will be presented in the following section.

(2) The behavior of the b factors in the region of line formation can be used to predict the nature of deviations from LTE in the line equivalent widths. For $\lambda 4129$ Å, the b factor of the upper level is larger than that of the lower level everywhere above $\log \tau_{5000} = 0$. This means that the line source functions S_{ij} exceed the Planck function $B_\nu(T)$, since

$$S_{ij} = \frac{2h\nu^3}{c^2} \frac{1}{\dfrac{b_i}{b_j} \exp(h\nu/kT) - 1} \simeq \frac{b_j}{b_i} B_\nu(T),$$

when $h\nu > kT$. Thus, the non-LTE EuII resonance line is weaker than in the LTE case, and non-LTE corrections to the europium abundance will be positive. For the $\lambda 6645$ Å subordinate line, on the contrary, $b_j < b_i$, so that the non-LTE line is stronger than in the LTE case, and non-LTE corrections to the abundance will be negative.

5. INFLUENCE OF INACCURACY IN THE ATOMIC PARAMETERS ON THE RESULTS

We performed 22 test computations for the model solar atmosphere [10] with various values of atomic parameters. We remark here only on those for which the deviations from LTE significantly changed.

Table 2. Oscillator strengths and shifts of the hyperfine structure of EuII line

Shift, mÅ	f_{ij}
Line λ4129.70Å	
−97	0.006
−78	0.009
−52	0.012
−17	0.021
−9	0.009
0	0.012
14	0.015
24	0.018
34	0.018
58	0.021
74	0.021
Line λ6645.11Å	
−41	0.0292
−29	0.0143
−18	0.0231
−10	0.0108
−3	0.0079
3	0.0154
11	0.0012
23	0.0089
38	0.0072
50	0.0054

(1) Among the $b-b$ transitions playing an important role in deviations from LTE, f_{ij} values are lacking for three of them—6, 7, and 8–32. We specified these values based on the argument that f_{ij} should be smaller for $6p$–$8s$ than for $6p$–$7s$. The f_{ij} values for transitions 6, 7–22 and 8–23 are similar (0.25, 0.39, and 0.26, respectively). Therefore, we adopted the single value $f_{ij} = 0.05$ for these transitions and carried out test computations with values a factor of two higher and lower. In both cases, only the b factor for level 32 changed, and the b factors for the levels of interest to us remained virtually the same.

(2) Most EuII lines in both the visible and ultraviolet are blended with strong lines of Fe I, Fe II, H I, and Ca II. If we do not allow for the additional opacity in the lines, the radiative rates for $b-b$ transitions will increase, and non-LTE effects will be enhanced (Fig. 4; we call this version of the computations blank.eff). Figure 4 presents for three versions of the test computations variations in the b factors for levels 1, 4, 6, and 7 relative to the standard run (0): $\Delta \log b_i = \log b_i - \log b_i(0)$. The standard run (0) corresponds to the atomic parameters described in Section 2; the $b_i(0)$ values are presented in Fig. 3, and their behavior is discussed in Section 4. In
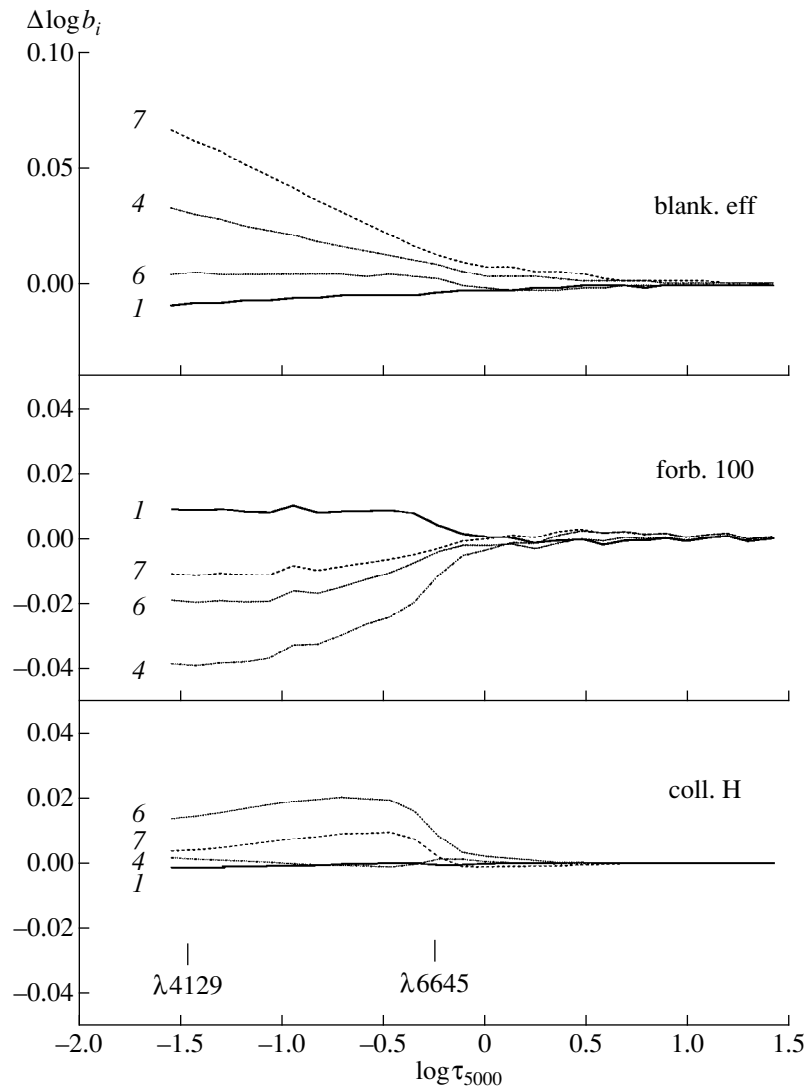
Fig. 4. Non-LTE effects in the populations of selected EuII levels for various sets of atomic parameters, compared to the standard set (0): blank.eff—blanketing not taken into account when computing the opacity; forb.100—rate of collisional excitation in forbidden transitions enhanced by a factor of 100; coll.H—inelastic collisions with H atoms not taken into account. The solar model atmosphere was used. $\Delta \log b_i = \log b_i - \log b_i(0)$. The depths of radiation in the cores of observed EuII lines are indicated.

the blank.eff test computation, the resonance line is weakened even more, so that the non-LTE correction to the abundance increases by 0.017 dex compared to the standard run. The change for the subordinate line is less, within 0.005 dex.

(3) The uncertainties in taking into account collisions with electrons for forbidden transitions and collisions with H atoms for all transitions are large. As we showed in [26], as a rule, the formula of Allen [13] underestimates the electron collisional excitation rate C_{ij}^e for forbidden transitions. Therefore, we performed our test run forb.100, in which the C_{ij}^e (Allen) values for transitions with $\Delta E_{ij} > 0.1$ eV were increased by a

factor of 100. For the resonance line, this led to the expected weakening of non-LTE effects: the non-LTE corrections to the abundance decreased by 0.024 dex compared to the standard run. There were important changes in the subordinate line. In contrast to the standard run, where the line was slightly increased compared to the LTE case, it was weakened in the forb.100 run; consequently, the corresponding non-LTE corrections to the abundance changed sign and became positive. This can be explained by the fact that the increase in the collisional connection of the $6s$ and $5d$ states leads to a decrease in overpopulation of the $5d$ levels; as a result, $\lambda 6645$ Å $b(7)$ becomes larger than $b(4)$ (Fig. 4, forb.100) and $S_\nu > B_\nu(T)$ in the region of formation of the $\lambda 6645$ Å line.

In principle, we can distinguish between various sets of atomic parameters based on the analysis of observed EuII lines. In Section 6, we empirically estimate the efficiency of collisional processes in forbidden transitions. We also ran test computations to estimate the influence of inelastic collisions with hydrogen atoms on the statistical equilibrium of EuII. As a rule, the formula of Steenbock and Holweger [16] used to calculate the excitation rate due to collisions with hydrogen atoms C_{ij}^{H} gives overestimated values of C_{ij}^{H} [26]. In our previous study [2], we used an analysis of BaII lines in halo stars to empirically estimate the scaling coefficient $k_{H} = 1/3$ in the formula of Steenbock and Holweger [16]. Therefore, we adopted here the standard run $k_{H} = 1/3$ and conducted test computations with $k_{H} = 0$, 0.5, and 1. Neglecting collisions with H atoms ($k_{H} = 0$) increases non-LTE effects (Fig. 4, coll.H), and increasing the efficiency of these collisions weakens non-LTE effects. However, the changes are so small that the non-LTE corrections to the abundance vary by no more than 0.01 dex compared to the standard run. For this reason, we decided not to try to empirically estimate the value of k_{H} and used in all cases $k_{H} = 1/3$.

Thus, the largest uncertainties in the results of our EuII non-LTE computations for solar-type stars are associated with uncertainty in the rates of collisional processes.

6. RESULTS

6.1. Analysis of EuII Lines in the Solar Spectrum

By comparing the observed and theoretical profiles for the two EuII lines, we attempted to empirically refine the values of the atomic parameters on which the results of our non-LTE computations depend. We used the atlas of the Sun as a star constructed by Kurucz *et al.* [23] using observations with high spectral resolution $\lambda/\Delta\lambda \simeq 500\,000$.

Figure 5 presents the observed profiles of the $\lambda4129$ and $\lambda6645$ Å EuII lines, shown by the solid curves. We can see that both lines are asymmetrical, due to both the hyperfine structure of the EuII lines and blending with lines of other elements. We computed the synthetic spectrum using the SIU code, kindly provided by the Institute of Astronomy and Astrophysics of Munich University.

Our line list was composed using the new data of Kurucz [10] supplemented with the SiI $\lambda6645.2$ Å line from the VALD database [8]. The importance of taking this line into account when analyzing the EuII $\lambda6645.1$ Å line is demonstrated in Fig. 5, where the dotted curves show two theoretical spectra: one computed without allowance for the SiI line and the other without allowance for the EuII line. In order to adequately describe the observed blend near 6645 Å, we had to decrease the VALD $\log gf$ value for the SiI line [8] by 0.3 dex.

When computing the theoretical spectra, we used the b factors for the EuII levels obtained using the

NONLTE3 code. We assumed LTE for the remaining atoms and ions. We carried out computations for two models of the solar atmosphere, based on the models of Holweger and Muller [27] (Holmu) and of Kurucz [10] (Sun-new). The differences between the computed EuII lines were negligible in both the LTE and non-LTE cases: the central depths of the $\lambda4129$ and $\lambda6645$ Å lines differed by 0.017 and 0.001, respectively. Therefore, all subsequent results were obtained only for the Sun-new model.

The theoretical spectra were computed using a single microturbulence velocity $V_{mic} = 0.8$ km/s, taking into account rotation with $V\sin i = 1.8$ km/s and radial–tangential macroturbulence with V_{mac}. We estimated the value of V_{mac} by comparing the observed and theoretical profiles for five FeI lines located near the EuII resonance line. For the various iron lines, V_{mac} was 3.6–3.8 km/s, and the profiles of both EuII lines are best fit when $V_{mac} = 3.6$ km/s.

We then carried out non-LTE computations for the standard set of atomic parameters and the forb.100 set (see above). In each case, we determined the europium abundance ε_{Eu} for which the best agreement between the synthetic and observed spectra was achieved. In the case of the resonance line, we were able to obtain a good agreement only for the long-wavelength half of the profile; apparently, the blue wing is enhanced by blends that we have not taken into account.

In the standard run, the abundance derived from the $\lambda4129$ Å line turned out to be 0.16 dex higher than that derived from the $\lambda6645$ Å line. Since the non-LTE difference $\log\varepsilon_{Eu}(\lambda4129) - \log\varepsilon_{Eu}(\lambda6645)$ was only 0.05 dex, we conclude that the standard run, in which the non-LTE corrections to the abundance were positive for $\lambda4129$ Å and negative for $\lambda6645$ Å [which only increases the difference $\log\varepsilon_{Eu}(\lambda4129) - \log\varepsilon_{Eu}(\lambda6645)$], cannot provide a correct treatment of the statistical equilibrium of EuII. Of all the computation runs considered, only that with an increased collisional rate for forbidden transitions gives non-LTE corrections of the same sign for both lines. The theoretical spectra in Fig. 5 correspond to precisely this run (forb.100). The observed profiles for both lines are satisfactorily fit when $\log\varepsilon_{Eu} = 0.49$.

The meteoritic abundance of europium is $\log\varepsilon_{Eu} = 0.54$ according to [5] and 0.55 ± 0.02 according to [28]. The small difference of the abundance obtained by us from the meteoritic value could have two origins. First, the EuII energy levels used by us, known from laboratory measurements, include only nonet and septet systems. Butler [30] has estimated that the missing levels of the quintet, triplet, and singlet systems should increase the sum over the states by roughly 6%, which corresponds to an underestimation in the Eu abundance by 0.03 dex. Second, the europium abundance depends on
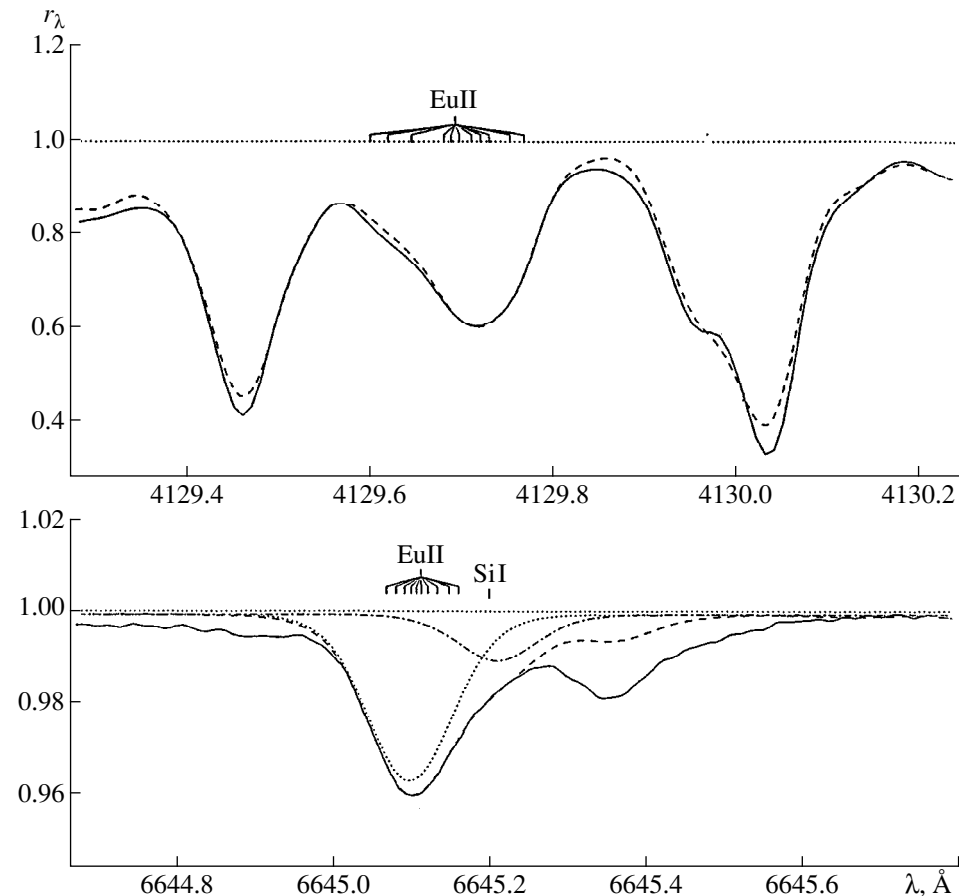
Fig. 5. Comparison of EuII $\lambda 4129$ and $\lambda 6645$ Å line profiles observed in the spectrum of the Sun [23] (solid curves) and theoretical non-LTE profiles (dashed curves) corresponding to our forb.100 run, computed for a Kurucz model [10] with $T_{eff} = 5780$ K, $\log g = 4.44$, $[A] = 0$, with $\log \varepsilon_{Eu} = 0.49$, $V_{mic} = 0.8$ km/s, $V \sin i = 1.8$ km/s, and $V_{mac} = 3.6$ km/s. The dotted curve shows the profile of the EuII 6645 Å line in the absence of the nearby SiI line, and the dash–dot curve shows the profile of the SiI line in the absence of the EuII line.

the model atmosphere used. The value $\log \varepsilon_{Eu} = 0.49$ corresponds to the Holmu [27] and Sun-new [10] models.

Thus, we consider the results obtained using the atomic-parameter set with an enhanced collisional rate for forbidden transitions to be the best for the analysis of statistical equilibrium of EuII. We hope that it will be possible to make a final choice of parameter set based on analyses of the EuII lines of hotter stars, for which non-LTE effects are stronger (see below).

6.2. Dependence of Non-LTE Effects on T_{eff} and Metallicity

We carried out non-LTE computations for a set of model atmospheres with solar chemical composition and $\log g = 4.0$ for the range $T_{eff} = 5500$–7000 K, and also for a set of atmospheres with $T_{eff} = 5500$ K and $\log g = 4.0$, but with heavy-element contents $[A]$ varying from 0 to –1.5. The results are shown in Fig. 6, in the form

of non-LTE corrections to the abundance Δ_{NLTE}, defined such that $\Delta_{NLTE} : \log \varepsilon_{NLTE} = \log \varepsilon_{LTE} + \Delta_{NLTE}$. The results for the resonance line are presented only for the forb.100 run, which we selected based on our analysis of the solar lines. For $\lambda 6645$ Å, we also present the non-LTE abundance corrections for the standard run (0).

The difference between the two runs increases with T_{eff}, and, at 7000 K, the difference Δ_{NLTE} reaches ~ 0.15 dex. Such values are detectable in analyses of observational data. We can see from Fig. 6 that the deviations from LTE grow with an increase in T_{eff} and with a decrease in the heavy-element content. In both cases, the increase in the magnitude of non-LTE corrections is associated with an increase in the radiation field and the rates of radiative processes; however, in the former case, this is facilitated by an increase in the temperature and, in the latter case, by a decrease in the opacity at ultraviolet and visible wavelengths.
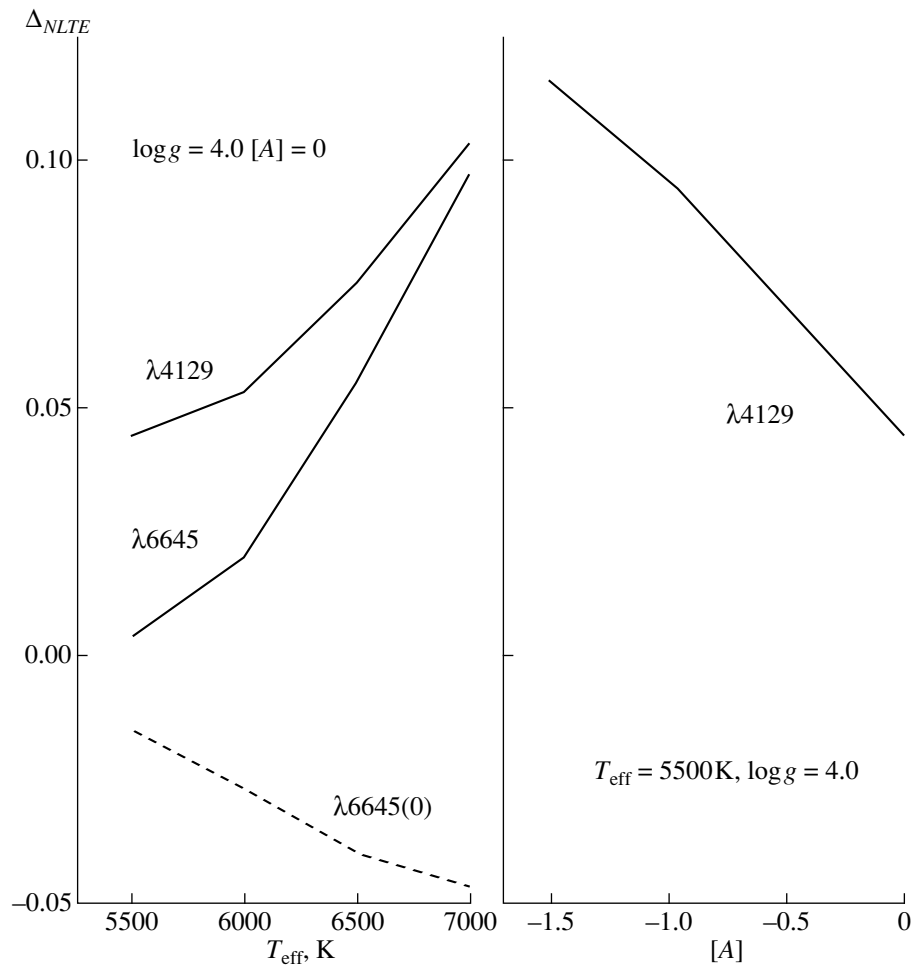
Fig. 6. Non-LTE corrections to the europium abundance for the forb.100 run (solid curve) as a function of effective temperature and heavy-element content. The dotted curve presents the results for the standard run (0).

Within the range of stellar parameters we have considered here, the non-LTE corrections to the Eu abundance are modest: $|\Delta_{NLTE}| < 0.12$ dex. Nonetheless, failure to take into account deviations from LTE introduces systematic errors into abundance determinations.

REFERENCES

1. L. I. Mashonkina and I. F. Bikmaev, Astron. Zh. **73**, 109 (1996) [Astron. Rep. **40**, 94 (1996)].

2. L. I. Mashonkina, T. Gehren, and I. F. Bikmaev, Astron. Astrophys. **343**, 519 (1999).

3. G. J. Mathews, G. Bazan, and J. J. Cowan, Astrophys. J. **391**, 719 (1992).

4. A. G. W. Cameron, Astron. Astrophys., Suppl. Ser. **82**, 123 (1982).

5. E. Anders and N. Grevesse, Geochim. Cosmochim. Acta **53**, 197 (1989).

6. R. G. Gratton and C. Sneden, Astron. Astrophys. **287**, 927 (1994).

7. W. C. Martin, R. Zalubas, and L. Hagan, *Atomic Energy Levels—The Rare Earth Elements*, NSRDS-NBS 60 (US Gov. Print. Off., Washington, 1978).

8. F. Kupka, N. Piskunov, T. A. Ryabchikova, *et al.*, Astron. Astrophys., Suppl. Ser. **138**, 119 (1999).

9. V. A. Komarovskiĭ, Opt. Spektrosk. **71**, 559 (1991) [Opt. Spectrosc. **71**, 322 (1991)].

10. R. L. Kurucz, CD-Roms, Nos. 18, 19 (1994).

11. G. Peach, Mem. R. Astron. Soc. **71**, 13 (1967).

12. H. van Regemorter, Astrophys. J. **136**, 906 (1962).

13. C. W. Allen, *Astrophysical Quantities* (Athlone, London, 1973; Mir, Moscow, 1977).

14. H.-W. Drawin, Z. Phys. **164**, 513 (1961).

15. I. I. Sobelman, L. A. Vainshtein, and E. A. Yukov, *Excitation of Atoms and Broadening of Spectral Lines* (Nauka, Moscow, 1979; Springer, Berlin, 1981).

16. W. Steenbock and H. Holweger, Astron. Astrophys. **130**, 319 (1984).

17. Y. Takeda, Pub. Astron. Soc. Jpn. **46**, 53 (1994).

18. N. A. Sakhibullin, Tr. Kazan. Gor. Astron. Obs. **48**, 9 (1983).

19. L. H. Auer and J. Heasley, Astrophys. J. **205**, 165 (1976).

20. L. I. Mashonkina, N. A. Sakhibullin, and N. N. Shimanskaya, Astron. Zh. **73**, 212 (1996) [Astron. Rep. **40**, 187 (1996)].

21. R. O. Doyle, Astrophys. J. **153**, 987 (1968).

22. D. Gray, *The Observation and Analysis of Stellar Photospheres* (Wiley, New York, 1976; Mir, Moscow, 1983).

23. R. L. Kurucz, I. Furenlid, J. Brault, and L. Testerman, *Solar Flux Atlas from 296 to 1300 nm* (Nat. Solar Obs., Sunspot, New Mexico, 1984).

24. D. Biehl, Sonderdruck der Sternwarte Kiel, No. 229 (1976).

25. M. Steffen, Astron. Astrophys., Suppl. Ser. **59**, 403 (1985).

26. L. I. Mashonkina, *Model Atmospheres and Spectrum Synthesis*, ASP Conf. Ser. **108**, 140 (1996).

27. H. Holweger and E. Muller, Solar Phys. **39**, 19 (1974).

28. N. Grevesse, A. Noels, and A. J. Sauval, Astron. Soc. Pac. Conf. Ser. **99**, 117 (1996).

29. K. Butler, private communication (1999).

Translated by D. Gabuzda